

Spatial Dispersion in Phonon Focusing

Kudakwashe Jakata

A dissertation submitted to the Faculty of Science, University of the Witwatersrand, Johannesburg, in fulfillment of the requirements for the degree of Master of Science.

Johannesburg, 2007

Declaration

I declare that this dissertation is my own, unaided work. It is being submitted for the Degree of Master of Science in the University of the Witwatersrand, Johannesburg. It has not been submitted before for any degree or examination in any other University.

K. Jakata

____ day of _____ 2007

Abstract

The ballistic phonon flux emanating from a point-like heat source in a crystal shows strong directional dependence. This effect is called phonon focusing and is measured using a technique called phonon imaging. In situations where long wavelength phonons are involved, the observations can be explained on the basis of classical continuum elasticity theory. Dispersion i.e. the variation of velocity with wavelength, sets in when the phonon wavelengths become comparable to the natural scale of length of the material, the lattice constant. This has a significant effect in the phonon focusing pattern and causes shorter wavelength phonons to lag behind longer wavelength ones and the dispersion relation i.e. the relation between angular frequency ω and wave number \mathbf{k} becomes non-linear.

A number of studies have used lattice dynamics models to explain the observed dispersive phonon images. Measured phonon images are not entirely satisfactorily reproduced by any of these lattice dynamics models and the different models tend to predict somewhat different focusing patterns. In this thesis, we set out to explain the observed dispersive phonon focusing patterns of cubic crystals by using a modification of continuum elasticity theory. This is done by including third and fourth order spatial derivatives of the displacement field in the wave equation. The coefficients of these higher order terms are the dispersive elastic constants. They are determined through optimized fitting to frequency versus wave vector data extracted from neutron scattering experiments for the acoustic modes in symmetry directions of a number of cubic crystals.

Our approach is limited to the first onset of spatial dispersion and does not apply to near Brillouin zone boundary phonons. It is also applicable to crystals of any symmetry

but in this thesis we focus on crystals of cubic symmetry. We report results on two crystals with a centre of inversion, Ge and Si, and two crystals without a centre of inversion, InSb and GaAs.

Contents

1	Introduction	1
1.1	The phonon imaging principle	2
1.2	Dispersive phonons	5
2	Elastic waves in Crystals: The long wavelength limit	7
2.1	Stress, strain and Hooke's law	7
2.2	Christoffel's equations	10
2.3	The slowness surface and group velocity	12
2.4	Maris phonon enhancement factor	16
2.5	Phase velocity along symmetry directions	17
2.6	Elastic parameter space	19
2.7	Non-dispersive phonon focusing	22
3	Dispersive phonons in cubic crystals	25
3.1	Extension of continuum elasticity theory to include dispersive effects	26

3.2	Dispersion relations along symmetry directions	29
3.3	Determination of elastic constants and dispersion parameters of crystals with a centre of inversion	33
3.3.1	Elastic constants, dispersion parameters and dispersion curves of Ge	36
3.3.2	Elastic constants, dispersion parameters and dispersion curves of Si along symmetry directions	39
3.4	Determination of elastic constants and dispersion parameters of InSb	42
3.4.1	Dispersion curves of InSb along symmetry and Brillouin zone centre directions	46
3.5	Determination of elastic constants and dispersion parameters of GaAs	48
3.5.1	Dispersion curves of GaAs along symmetry and Brillouin zone centre directions	51
3.6	Dispersive phonon imaging calculations	53
4	Phonon focusing patterns of Ge and Si	55
4.1	Comparison of calculated images with measured in Ge	55
4.1.1	Comparison of phonon images calculated using shell model derived elastic constants with measured images in Ge	59
4.2	Further frequency dependent Ge dispersive phonon images	61
4.3	Comparison of calculated images with measurements for Si	64

4.3.1	Comparison of images calculated using MD derived elastic constants with measurements for Si	67
4.4	Further frequency dependent dispersive phonon images of Si	67
5	Phonon focusing patterns of InSb and GaAs	71
5.1	Frequency dependence of dispersive phonon images of InSb	71
5.2	Evolution of dispersive phonon images of InSb in the (100) plane	75
5.3	Comparison of GaAs experimental images with calculated images	79
5.3.1	Comparison of GaAs experimental images with images calculated using DiVincenzo elastic constants	81
5.4	Frequency dependence of GaAs dispersive phonon images in the (100) plane	83
6	Conclusions	85
	Appendix	95

List of tables

3.1	Non-dispersive and dispersive elastic constants of germanium obtained by fitting to neutron scattering data to the continuum model versus a shell model.	37
3.2	Non-dispersive and dispersive elastic constants of silicon obtained by fitting neutron scattering data to the continuum model versus a molecular dynamics model.	40
3.3	Non-dispersive and dispersive elastic constants of indium antimonide obtained by fitting neutron scattering data to the continuum model.	46
3.4	Non-dispersive and dispersive elastic constants of Gallium Arsenide obtained by fitting neutron scattering data the continuum model versus the shell model.	50

List of figures

1.1	The phonon imaging principle	3
1.2a	Calculated non-dispersive phonon images of the FT and ST modes of GaAs in the (a) (100), (b) (110) and (c) (111) observation planes	4
1.2b	Calculated non-dispersive phonon images of the FT and ST modes of GaAs in the (a) (100), (b) (110) and (c) (111) observation planes	4
1.2c	Calculated non-dispersive phonon images of the FT and ST modes of GaAs in the (a) (100), (b) (110) and (c) (111) observation planes	4
2.1	The force per unit area, σ_{ij} , transmitted across the faces along the x_1 , x_2 and x_3 directions of an infinitesimal cube (Every, 2001).	9
2.2	Cross section of the slowness surface for Si in the (010) plane	13
2.3	Cross section of the slowness surface of Si in the (110) plane	13
2.4	Three dimensional ST sheet of the slowness surface for a Si crystal. Shaded regions are of saddle curvature and unshaded regions have convex or concave curvature (Calculated by A.G. Every).	14
2.5	Cross section of the ST and FT sheets of the wave surface for a Si crystal in the (100) plane.	15
2.6	Elastic parameter space for cubic crystals using elastic constants compiled by Every and McCurdy in the Landolt-Börnstein Series, (1992).	20
2.7	Cross section of the slowness surface for a positive- Δ crystal, CaF ₂ , in the (110) plane.	21

2.8a	Non dispersive FT and ST phonon focusing pattern of CaF ₂ , a positive- Δ crystal, in the (a) (111), (b) (100) and (c) (110) observation planes. The angular width of the images from left to right is 90°.	24
2.8b	Non dispersive FT and ST phonon focusing pattern of CaF ₂ , a positive- Δ crystal, in the (a) (111), (b) (100) and (c) (110) observation planes. The angular width of the images from left to right is 90°.	24
2.8c	Non dispersive FT and ST phonon focusing pattern of CaF ₂ , a positive- Δ crystal, in the (a) (111), (b) (100) and (c) (110) observation planes. The angular width of the images from left to right is 90°.	24
3.1	Dispersion curve of Ge along the (a) $\langle 100 \rangle$, (b) $\langle 111 \rangle$ and (c) $\langle 110 \rangle$ directions using optimized values of the elastic constants. The data points represent neutron scattering data (Nilsson and Nelin, 1971).	38
3.2	Dispersion curves of Ge along the (a) $\langle 100 \rangle$, (b) $\langle 110 \rangle$ and (c) $\langle 111 \rangle$ directions using elastic constants extracted by Maranganti et al (2007). The data points represent neutron scattering data (Nilsson and Nelin, 1971).	39
3.3	Dispersion curves of Si along the (a) $\langle 100 \rangle$, (b) $\langle 110 \rangle$ and (c) $\langle 111 \rangle$ directions using optimized elastic constants. The data points represent neutron scattering data (Dolling, 1963; Nilsson and Nelin, 1972).	41
3.4	Dispersion curves of Si along the (a) $\langle 100 \rangle$, (b) $\langle 110 \rangle$ and (c) $\langle 111 \rangle$ directions using molecular dynamics elastic constants extracted by Maranganti et al (2007). The data points represent neutron scattering data (Dolling, 1963 and Nilsson and Nelin, 1972).	41

3.5	Dispersion curves of InSb along the (a) $\langle 100 \rangle$, (b) $\langle 110 \rangle$ and (c) $\langle 111 \rangle$ directions. The data points represent neutron scattering data (Price et al, 1971).	47
3.6	Dispersion curves of InSb along the direction through the centre of the irreducible sector.	47
3.7	Dispersion curves of GaAs along the (a) $\langle 100 \rangle$, (b) $\langle 110 \rangle$ and (c) $\langle 111 \rangle$ directions using optimized values of the elastic constants. The data points represent neutron scattering data (Dolling et al, 1963).	51
3.8	Dispersion curves of GaAs along the direction through the centre of the irreducible sector.	52
3.9	Dispersion curves of GaAs along the (a) $\langle 100 \rangle$, (b) $\langle 110 \rangle$ and (c) $\langle 111 \rangle$ directions. The data points represent neutron scattering data (Dolling et al, 1963).	52
3.10a	Calculated dispersive phonon images of Ge in the (110) observation plane: (a) 0.0-0.3THz (b) 0.5-0.6THz.	54
3.10b	Calculated dispersive phonon images of Ge in the (110) observation plane: (a) 0.0-0.3THz (b) 0.5-0.6THz.	54
4.1a	Phonon images of Ge in the (110) observation plane: (a) measured image using a bolometric detector by Dietsche et al, (1981), (b) calculated non-dispersive phonon image.	56
4.1b	Phonon images of Ge in the (110) observation plane: (a) measured image using a bolometric detector by Dietsche et al, (1981), (b) calculated non-dispersive phonon image.	56

- 4.2a Phonon images of Ge in the (110) observation plane, (a) measured using a detector with 0.7THz onset frequency by Dietsche et al, (1981). Calculated images: (b) selecting wave vector k up to 0.3 for phonons with frequencies between 0.7THz and 1.0 THz, (c) selecting wave vector k up to 0.15 for phonons with frequencies near 0.85THz. 58
- 4.2b Phonon images of Ge in the (110) observation plane, (a) measured using a detector with 0.7THz onset frequency by Dietsche et al, (1981). Calculated images: (b) selecting wave vector k up to 0.3 for phonons with frequencies between 0.7THz and 1.0 THz, (c) selecting wave vector k up to 0.15 for phonons with frequencies near 0.85THz. 58
- 4.2c Phonon images of Ge in the (110) observation plane, (a) measured using a detector with 0.7THz onset frequency by Dietsche et al, (1981). Calculated images: (b) selecting wave vector k up to 0.3 for phonons with frequencies between 0.7THz and 1.0 THz, (c) selecting wave vector k up to 0.15 for phonons with frequencies near 0.85THz. 58
- 4.3a Phonon images of Ge in the (100) observation plane for the frequency range: $0.3 \leq f \leq 0.4$ THz. (a) measured image by Metzger and Huebener (1988). (b) Calculated image. 59
- 4.3b Phonon images of Ge in the (100) observation plane for the frequency range: $0.3 \leq f \leq 0.4$ THz. (a) measured image by Metzger and Huebener (1988). (b) Calculated image. 59
- 4.4a Phonon images of Ge in the (110) observation plane: (a) measured image using a bolometric detector by Dietsche et al, (1981), (b) calculated phonon image for essentially non-dispersive phonons in the 0.0 THz to 0.3THz frequency range using shell model elastic constants (Maranganti et al, 2007). 60

4.4b	Phonon images of Ge in the (110) observation plane: (a) measured image using a bolometric detector by Dietsche et al, (1981), (b) calculated phonon image for essentially non-dispersive phonons in the 0.0 THz to 0.3THz frequency range using shell model elastic constants (Maranganti et al, 2007).	60
4.5a	Phonon images of Ge in the (100) observation plane for the frequency range: $0.3 \leq f \leq 0.4$ THz. (a) measured image by Metzger and Huebener (1988). (b) Calculated phonon image using shell model elastic constants (Maranganti et al, 2007).	60
4.5b	Phonon images of Ge in the (100) observation plane for the frequency range: $0.3 \leq f \leq 0.4$ THz. (a) measured image by Metzger and Huebener (1988). (b) Calculated phonon image using shell model elastic constants (Maranganti et al, 2007).	60
4.6a	Calculated dispersive phonon images of germanium in the (110) imaging plane for the frequency ranges: (a) 0.0 - 0.3 THz (b) 0.5 - 0.6 THz (c) 0.7 - 0.8 THz (d) 0.9 - 1.0 THz.	61
4.6b	Calculated dispersive phonon images of germanium in the (110) imaging plane for the frequency ranges: (a) 0.0 - 0.3 THz (b) 0.5 - 0.6 THz (c) 0.7 - 0.8 THz (d) 0.9 - 1.0 THz.	61
4.6c	Calculated dispersive phonon images of germanium in the (110) imaging plane for the frequency ranges: (a) 0.0 - 0.3 THz (b) 0.5 - 0.6 THz (c) 0.7 - 0.8 THz (d) 0.9 - 1.0 THz.	61
4.6d	Calculated dispersive phonon images of germanium in the (110) imaging plane for the frequency ranges: (a) 0.0 - 0.3 THz (b) 0.5 - 0.6 THz (c) 0.7 - 0.8 THz (d) 0.9 - 1.0 THz.	61
4.7	The angle between FT caustics, θ_{FT} , as a function of phonon frequency for Ge.	62

4.8a	Calculated dispersive phonon images of germanium in the (100) imaging plane: (a) 0.0 - 0.3 THz (b) 0.5 - 0.6 THz (c) 0.7 - 0.8 THz (d) 0.9 - 1.0 THz.	63
4.8b	Calculated dispersive phonon images of germanium in the (100) imaging plane: (a) 0.0 - 0.3 THz (b) 0.5 - 0.6 THz (c) 0.7 - 0.8 THz (d) 0.9 - 1.0 THz.	63
4.8c	Calculated dispersive phonon images of germanium in the (100) imaging plane: (a) 0.0 - 0.3 THz (b) 0.5 - 0.6 THz (c) 0.7 - 0.8 THz (d) 0.9 - 1.0 THz.	63
4.8d	Calculated dispersive phonon images of germanium in the (100) imaging plane: (a) 0.0 - 0.3 THz (b) 0.5 - 0.6 THz (c) 0.7 - 0.8 THz (d) 0.9 - 1.0 THz.	63
4.9	The ratio u as a function of phonon frequency.	64
4.10a	Phonon images of Si in the (100) observation plane (a) measured image by Tamura, Shields and Wolfe (1991) using a PbTI tunnel junction detector with an onset frequency of 0.44THz. (b) Calculated image for the frequency range: $0.4 \leq f \leq 0.5$ THz	65
4.10b	Phonon images of Si in the (100) observation plane (a) measured image by Tamura, Shields and Wolfe (1991) using a PbTI tunnel junction detector with an onset frequency of 0.44THz. (b) Calculated image for the frequency range: $0.4 \leq f \leq 0.5$ THz	65
4.11a	Phonon images of Si in the (100) observation plane: (a) measured using a detector with onset frequency 0.7THz by Tamura, Shields and Wolfe (1991), (b) Calculated image for the frequency range: $0.7 \leq f \leq 0.9$ THz.	66

- 4.11b Phonon images of Si in the (100) observation plane: (a) measured using a detector with onset frequency 0.7THz by Tamura, Shields and Wolfe (1991), (b) Calculated image for the frequency range: $0.7 \leq f \leq 0.9$ THz. 66
- 4.12a Phonon images of Si in the (110) observation plane: (a) measured using a detector with onset frequency 0.82THz by Shields et al (1991), (b) Calculated image for the frequency range: $0.8 \leq f \leq 0.9$ THz. 67
- 4.12b Phonon images of Si in the (110) observation plane: (a) measured using a detector with onset frequency 0.82THz by Shields et al (1991), (b) Calculated image for the frequency range: $0.8 \leq f \leq 0.9$ THz. 67
- 4.13a . Phonon images of Si in the (100) observation plane (a) measured image by Tamura, Shields and Wolfe (1991) using a PbTI tunnel junction detector with an onset frequency of 0.44THz. (b) Calculated image for the frequency range: $0.44 \leq f \leq 0.54$ THz using MD lattice dynamics elastic constants extracted by Maranganti et al (2007). 68
- 4.13b . Phonon images of Si in the (100) observation plane (a) measured image by Tamura, Shields and Wolfe (1991) using a PbTI tunnel junction detector with an onset frequency of 0.44THz. (b) Calculated image for the frequency range: $0.44 \leq f \leq 0.54$ THz using MD lattice dynamics elastic constants extracted by Maranganti et al (2007). 68
- 4.14a Phonon images of Si in the (100) observation plane: (a) measured using a detector with onset frequency 0.7THz by Tamura, Shields and Wolfe (1991), (b) Calculated phonon image for the frequency range: $0.7 \leq f \leq 0.9$ THz using MD elastic constants extracted by Maranganti et al (2007). 68

4.14b	Phonon images of Si in the (100) observation plane: (a) measured using a detector with onset frequency 0.7THz by Tamura, Shields and Wolfe (1991), (b) Calculated phonon image for the frequency range: $0.7 \leq f \leq 0.9$ THz using MD elastic constants extracted by Maranganti et al (2007).	68
4.15a	Calculated dispersive phonon images of silicon in the (110) imaging plane: (a) 0.0 - 0.3 THz (b) 0.9 - 1.0 THz (c) 1.5 - 1.6 THz (d) 1.9 - 2.0 THz	69
4.15b	Calculated dispersive phonon images of silicon in the (110) imaging plane: (a) 0.0 - 0.3 THz (b) 0.9 - 1.0 THz (c) 1.5 - 1.6 THz (d) 1.9 - 2.0 THz	69
4.15c	Calculated dispersive phonon images of silicon in the (110) imaging plane: (a) 0.0 - 0.3 THz (b) 0.9 - 1.0 THz (c) 1.5 - 1.6 THz (d) 1.9 - 2.0 THz	69
4.15d	Calculated dispersive phonon images of silicon in the (110) imaging plane: (a) 0.0 - 0.3 THz (b) 0.9 - 1.0 THz (c) 1.5 - 1.6 THz (d) 1.9 - 2.0 THz	69
4.16a	Calculated dispersive phonon images of silicon in the (100) imaging plane: (a) 0.0 - 0.3 THz (b) 0.9 - 1.0 THz (c) 1.5 - 1.6 THz (d) 1.9 - 2.0 THz.	70
4.16b	Calculated dispersive phonon images of silicon in the (100) imaging plane: (a) 0.0 - 0.3 THz (b) 0.9 - 1.0 THz (c) 1.5 - 1.6 THz (d) 1.9 - 2.0 THz.	70
4.16c	Calculated dispersive phonon images of silicon in the (100) imaging plane: (a) 0.0 - 0.3 THz (b) 0.9 - 1.0 THz (c) 1.5 - 1.6 THz (d) 1.9 - 2.0 THz.	70

4.16d	Calculated dispersive phonon images of silicon in the (100) imaging plane: (a) 0.0 - 0.3 THz (b) 0.9 - 1.0 THz (c) 1.5 - 1.6 THz (d) 1.9 - 2.0 THz.	70
5.1a	Non-dispersive phonon images of InSb in the (110) observation plane. (a) Measured image by Hebboul and Wolfe (1989). (b) Calculated image.	72
5.1b	Non-dispersive phonon images of InSb in the (110) observation plane. (a) Measured image by Hebboul and Wolfe (1989). (b) Calculated image.	72
5.2a	Phonon images of InSb in the (110) observation (a) measured image using a tunnel junction detector with an onset frequency of 0.43 THz (b) Calculated image in the 0.4 - 0.45THz frequency range.	73
5.2b	Phonon images of InSb in the (110) observation (a) measured image using a tunnel junction detector with an onset frequency of 0.43 THz (b) Calculated image in the 0.4 - 0.45THz frequency range.	73
5.3a	Phonon images of InSb in the (110) observation (a) Experimental image using a tunnel junction detector with an onset frequency of 0.593THz. (b) Calculated image in the 0.575-0.625THz frequency range.	74
5.3b	Phonon images of InSb in the (110) observation (a) Experimental image using a tunnel junction detector with an onset frequency of 0.593THz. (b) Calculated image in the 0.575-0.625THz frequency range.	74
5.4a	Phonon images of InSb in the (110) observation (a) measured image using a tunnel junction detector with an onset frequency of 0.688 THz (b) Calculated image in the 0.67 - 0.72THz frequency range.	75

5.4b	Phonon images of InSb in the (110) observation (a) measured image using a tunnel junction detector with an onset frequency of 0.688 THz (b) Calculated image in the 0.67 - 0.72THz frequency range.	75
5.5a	Calculated phonon images of InSb in the (100) observation for the: (a) 0.40-0.45THz (b) 0.57-0.62THz (c) 0.66-0.70THz (d) 0.70-0.75THz, frequency ranges	76
5.5b	Calculated phonon images of InSb in the (100) observation for the: (a) 0.40-0.45THz (b) 0.57-0.62THz (c) 0.66-0.70THz (d) 0.70-0.75THz, frequency ranges	76
5.5c	Calculated phonon images of InSb in the (100) observation for the: (a) 0.40-0.45THz (b) 0.57-0.62THz (c) 0.66-0.70THz (d) 0.70-0.75THz, frequency ranges	76
5.5d	Calculated phonon images of InSb in the (100) observation for the: (a) 0.40-0.45THz (b) 0.57-0.62THz (c) 0.66-0.70THz (d) 0.70-0.75THz, frequency ranges	76
5.6a	Phonon images of InSb measured in the (110) plane with a smaller angular scan to record a magnified view of the focusing structures around the [100] direction. They have been obtained with tunnel junction detectors sensitive to frequencies of: (a) 430 ± 42 GHz (b) 593 ± 12 GHz (c) 688 ± 17 GHz (d) 727 ± 18 GHz, frequency ranges.	78
5.6b	Phonon images of InSb measured in the (110) plane with a smaller angular scan to record a magnified view of the focusing structures around the [100] direction. They have been obtained with tunnel junction detectors sensitive to frequencies of: (a) 430 ± 42 GHz (b) 593 ± 12 GHz (c) 688 ± 17 GHz (d) 727 ± 18 GHz, frequency ranges.	78

- 5.6c Phonon images of InSb measured in the (110) plane with a smaller angular scan to record a magnified view of the focusing structures around the [100] direction. They have been obtained with tunnel junction detectors sensitive to frequencies of: (a) 430 ± 42 GHz (b) 593 ± 12 GHz (c) 688 ± 17 GHz (d) 727 ± 18 GHz, frequency ranges. 78
- 5.6d Phonon images of InSb measured in the (110) plane with a smaller angular scan to record a magnified view of the focusing structures around the [100] direction. They have been obtained with tunnel junction detectors sensitive to frequencies of: (a) 430 ± 42 GHz (b) 593 ± 12 GHz (c) 688 ± 17 GHz (d) 727 ± 18 GHz, frequency ranges. 78
- 5.7a Phonon images of GaAs. Measured images by Northrop et al (1985): (a) $f < 0.3$ THz, (b) $f > 0.7$ THz, $2.9 < V < 3.9$ $\mu\text{m}/\text{ns}$, (c) $f > 0.7$ THz, $2.3 < V < 3.1$ $\mu\text{m}/\text{ns}$. Calculated images: (d) $f < 0.3$ THz, (e) $0.7 < f < 1.0$ THz, $2.9 < V < 3.9$ $\mu\text{m}/\text{ns}$, (f) $0.7 < f < 1.0$ THz, $2.3 < V < 3.1$ $\mu\text{m}/\text{ns}$. 80
- 5.7b Phonon images of GaAs. Measured images by Northrop et al (1985): (a) $f < 0.3$ THz, (b) $f > 0.7$ THz, $2.9 < V < 3.9$ $\mu\text{m}/\text{ns}$, (c) $f > 0.7$ THz, $2.3 < V < 3.1$ $\mu\text{m}/\text{ns}$. Calculated images: (d) $f < 0.3$ THz, (e) $0.7 < f < 1.0$ THz, $2.9 < V < 3.9$ $\mu\text{m}/\text{ns}$, (f) $0.7 < f < 1.0$ THz, $2.3 < V < 3.1$ $\mu\text{m}/\text{ns}$. 80
- 5.7c Phonon images of GaAs. Measured images by Northrop et al (1985): (a) $f < 0.3$ THz, (b) $f > 0.7$ THz, $2.9 < V < 3.9$ $\mu\text{m}/\text{ns}$, (c) $f > 0.7$ THz, $2.3 < V < 3.1$ $\mu\text{m}/\text{ns}$. Calculated images: (d) $f < 0.3$ THz, (e) $0.7 < f < 1.0$ THz, $2.9 < V < 3.9$ $\mu\text{m}/\text{ns}$, (f) $0.7 < f < 1.0$ THz, $2.3 < V < 3.1$ $\mu\text{m}/\text{ns}$. 80
- 5.7d Phonon images of GaAs. Measured images by Northrop et al (1985): (a) $f < 0.3$ THz, (b) $f > 0.7$ THz, $2.9 < V < 3.9$ $\mu\text{m}/\text{ns}$, (c) $f > 0.7$ THz, $2.3 < V < 3.1$ $\mu\text{m}/\text{ns}$. Calculated images: (d) $f < 0.3$ THz, (e) $0.7 < f < 1.0$ THz, $2.9 < V < 3.9$ $\mu\text{m}/\text{ns}$, (f) $0.7 < f < 1.0$ THz, $2.3 < V < 3.1$ $\mu\text{m}/\text{ns}$. 80

- 5.8f Phonon images of GaAs. Measured images by Northrop et al (1985): 82
(a) $f < 0.3$ THz, (b) $f > 0.7$ THz, $2.9 < V < 3.9$ $\mu\text{m/ns}$, (c) $f > 0.7$ THz,
 $2.3 < V < 3.1$ $\mu\text{m/ns}$. Calculated images: (d) $f < 0.3$ THz, (e) $0.7 < f < 1.0$
THz, $2.9 < V < 3.9$ $\mu\text{m/ns}$, (f) $0.7 < f < 1.0$ THz, $2.3 < V < 3.1$ $\mu\text{m/ns}$.
- 5.9a Calculated phonon images of GaAs in the (110) plane: (a) $f < 0.3$ 84
THz, (b) $0.7 < f < 0.8$ THz, (c) $0.9 < f < 1.0$ THz, (d) $1.1 < f < 1.2$ THz.
- 5.9b Calculated phonon images of GaAs in the (110) plane: (a) $f < 0.3$ 84
THz, (b) $0.7 < f < 0.8$ THz, (c) $0.9 < f < 1.0$ THz, (d) $1.1 < f < 1.2$ THz.
- 5.9c Calculated phonon images of GaAs in the (110) plane: (a) $f < 0.3$ 84
THz, (b) $0.7 < f < 0.8$ THz, (c) $0.9 < f < 1.0$ THz, (d) $1.1 < f < 1.2$ THz.
- 5.9d Calculated phonon images of GaAs in the (110) plane: (a) $f < 0.3$ 84
THz, (b) $0.7 < f < 0.8$ THz, (c) $0.9 < f < 1.0$ THz, (d) $1.1 < f < 1.2$ THz.

Acknowledgements

I thank God for raising me up to more than I can be in the words of King David in 1 Chronicles 29:11-13.

I am very thankful to my supervisor, Professor A. G Every, for his guidance and patience throughout the project. I also thank him for offering me the opportunity to study for an MSc and for the knowledge that I have acquired whilst working with him.

I am also grateful to Kibraeb M. Haile for the useful discussions and my fellow postgraduate students and colleagues. I thank Ronald Machaka for making the process of coming to South Africa very smooth. I also thank my parents, sisters and my brother for the constant encouragement.

Chapter 1

Introduction

A phonon is a quantum of elastic vibration analogous to a photon in an electromagnetic wave. Heat transport in insulators is largely due to the migration of phonons. They propagate uniformly in all directions in elastically isotropic media. However, in anisotropic materials the phonon flux is strongly directionally dependent (Maris, 1971). For cubic crystals, which are the concern of this thesis, this is not observed at normal temperatures where motion of phonons is diffusive but only at near absolute zero in temperature where they travel with minimal scattering. An image showing the directional dependence of the ballistic phonon flux emanating from a point source in a crystal is called a phonon image or a phonon focusing pattern.

The propagation of phonons with wavelengths much larger than the lattice spacing of a crystal is well accounted for by continuum elasticity theory (Wolfe, 1998). Dispersion i.e. the variation of velocity with wavelength, sets in when the phonon wavelengths become comparable to the lattice parameter of the crystal (Every, 2005). Dispersion has a significant effect on the focusing patterns and commonly causes shorter wavelength phonons to lag behind longer wavelength ones, thus arriving later at the detector and the dispersion relation i.e. the relation between angular frequency ω and wave number k becomes non-linear. In this dissertation, we are attempting to explain the observed changes in the phonon focusing patterns of a number of crystals by an extension of continuum theory developed by DiVincenzo in 1986.

A brief explanation of the phonon imaging principle and dispersive phonons is given in this chapter. This is followed by an outline of continuum elasticity theory and its application to non-dispersive phonon imaging in the next

chapter. Chapter 3 deals with the extension of continuum elasticity theory to include the first onset of spatial dispersion. Calculated phonon images using modified continuum theory for two cubic crystals with a centre of inversion, Ge and Si, are given in chapter 4 and for two non-centrosymmetric cubic crystals, InSb and GaAs, in chapter 5. In chapter 6 we set out the conclusions.

1.1 The phonon imaging principle

The first experimental investigation of the ballistic heat pulse phenomenon at low temperatures was performed by von Gutfeld and Nethercot in 1964 on quartz and sapphire. It is found from such experiments, that phonons propagate for macroscopic distances through the crystal with minimal scattering, that is, they travel ballistically. Further investigations by Taylor, Maris and Elbaum (1969) revealed that the intensity or flux of acoustic phonons excited by this technique is dependent upon propagation direction. The enhancement of phonons in certain directions in anisotropic media was mathematically described by Maris in 1971. Experimental investigations by Northrop and Wolfe (1980) on germanium resulted in the first spatial images of ballistic heat pulses, for which they coined the name “phonon image”. A physical picture of the heat flux distribution arriving at the surface of a silicon crystal was produced by Eisenmenger (1980) using the fountain effect of liquid helium.

The heat pulse technique is the basis of phonon imaging in these experiments. A highly focused pulsed laser or electron beam is used to excite non-equilibrium phonons in a crystal immersed in a liquid helium bath at about 2K by heating a small spot on one face of the crystal. The ballistic phonon flux emanating from the heated spot is detected on the opposite face of the crystal by a bolometric or a frequency selective tunnel junction detector, see Figure 1.1. Small detector sizes are required, 10 to 30 μm^2 , for good angular resolution of ballistic phonon flux (Wolfe, 1998).

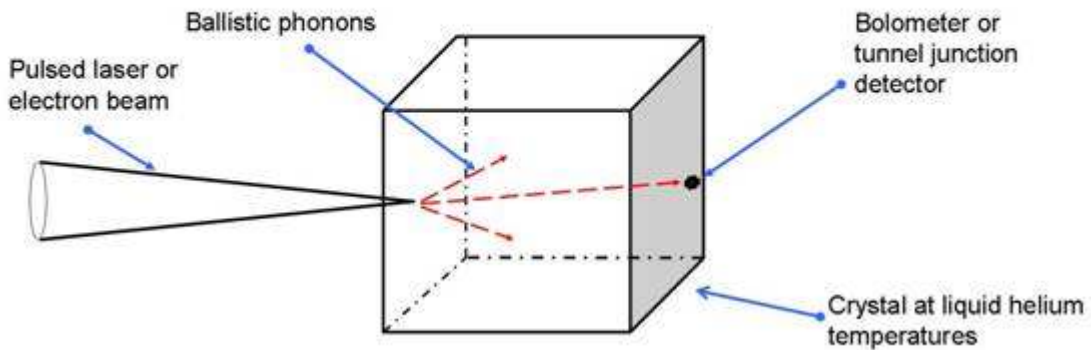


Figure 1.1 The phonon imaging principle

Raster scanning the phonon source with the detector at a fixed position, which is easier done than the other way round, shows that the phonon flux is highly directional, mainly due to phonon focusing which will be explained in detail later. The two dimensional image showing the spatial anisotropy of heat flow in a crystal which is obtained is called a phonon image.

The detected signal consists of a number of pulses corresponding to the arrival of phonons belonging to the fast transverse (FT), slow transverse (ST) and longitudinal (L) acoustic branches. The times of flight of the detected heat pulses are a measure of the phonon group velocities along a given propagation direction and the magnitudes of these pulses vary considerably with direction, which is mainly due to phonon focusing and to a lesser extent on geometrical factors, variation of the distance of travel and projection of the source and detector on the propagation direction.

Figure 1.2 below shows examples of calculated phonon images for non-dispersive phonons in a crystal of GaAs for the (100), (111) and (110) observation planes. The bright areas represent a high concentration of phonon

flux and caustics, the sharp bright lines, are regions where the phonon flux is mathematically infinite.

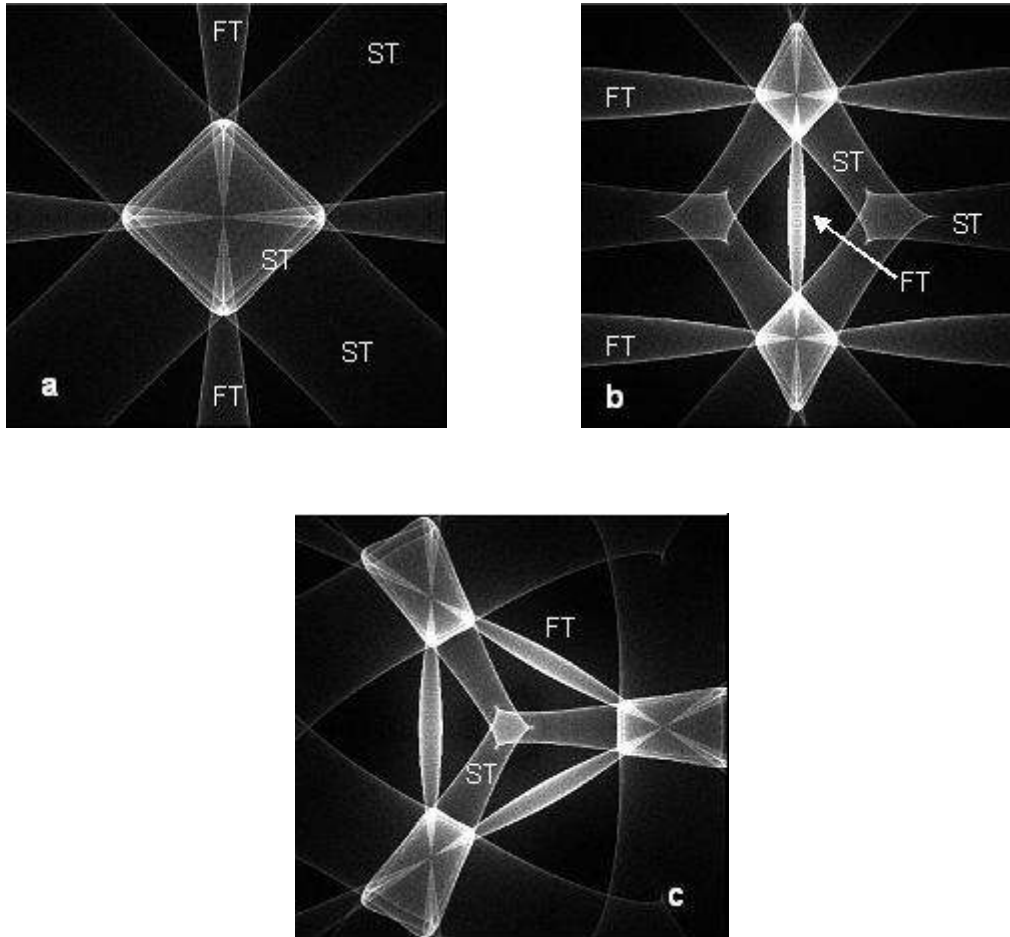


Figure 1.2 Calculated non-dispersive phonon images of the FT and ST modes of GaAs in the (a) $\langle 100 \rangle$, (b) $\langle 110 \rangle$ and (c) $\langle 111 \rangle$ observation planes

Figure 1.2a is centered on the $\langle 100 \rangle$ direction. The box structure around the $\langle 100 \rangle$ direction labeled ST is due to slow transverse branch phonons whilst the structures labeled FT are due to fast transverse phonons. Longitudinal phonons are not included in the calculations for these and other images presented in this thesis, since they do not give rise to any caustic structures. The box structures in figure 1.2a show up as the diamond shaped structures in figure 1.2b for the $\langle 110 \rangle$ plane, and are distorted because they are now projected

onto a different plane. In fact, the three images in figure 1.2 represent the same focusing pattern, and only look different because they are projected onto different imaging planes. The image in the (111) observation plane, figure 1.2c, is centered on the $\langle 111 \rangle$ direction. The structure at the centre and the three boxes are due to ST phonons whilst the ridges forming the triangular shape are due to FT phonons.

1.2 Dispersive phonons

A number of experimental and theoretical investigations of dispersive phonon images have been carried out by for example Dietsche et al (1981), Northrop (1982), Metzger and Huebener (1988), and Tamura (1982). In these experiments, frequency selective tunnel junction phonon detectors have been employed instead of the bolometric detectors used at non-dispersive frequencies. It is found that there are significant changes in the phonon focusing patterns of crystals at dispersive frequencies.

Theoretical studies of dispersive phonon images in the past have made use of lattice dynamics models. These include the shell model, rigid ion model (Hebboul and Wolfe, 1986), and the bond charge model (Tamura, 1981). The parameters of these models are adjusted to obtain agreement with the full phonon dispersion relation for optical and acoustical branches obtained from neutron scattering data. The observed images are not entirely satisfactorily reproduced by these models and moreover, different models predict markedly different phonon focusing patterns. In this thesis, we are attempting to explain the measured images on the basis of continuum theory modified to take into account the first onset of spatial dispersion as formulated by DiVincenzo in 1986. This is done through the inclusion of third and fourth order spatial derivatives of the displacement field in the wave equation. The coefficients of the higher order terms, the dispersive elastic constants are determined through

fitting to the near zone centre acoustic mode dispersion relations for the $\langle 100 \rangle$, $\langle 111 \rangle$ and $\langle 110 \rangle$ symmetry directions in cubic crystals obtained from neutron scattering experiments. Dispersive phonon images are then calculated using these dispersive elastic constants. With this approach, we investigate the phonon focusing patterns of Ge, Si, InSb and GaAs.

Chapter 2

Elastic waves in crystals:

The long wavelength limit

The propagation of acoustic waves in a solid is associated with dynamic stresses and strains which are related through the elastic constants of the medium. The continuum approximation is valid when the wavelength is much larger than the natural scale of length of the medium. The characteristic scale of length in a crystal is the lattice parameter which is of the order of $\sim 10^{-3}$ μm . For phonons propagating with wavelengths much larger than the lattice spacing, phonon focusing patterns are independent of frequency. Experimental investigations on these non-dispersive phonon images are usually carried out with a superconducting bolometric detector (Wolfe, 1998). It is sensitive to low frequency phonons, usually below about 100 GHz. A brief outline of the non-dispersive continuum elasticity theory explanation of non dispersive phonon images is given in this chapter.

2.1 Stress, strain and Hooke's law

Strain describes the change in length, relative displacement in parallel layers and the changes in volume of a solid when a force is applied to it. If a material particle moves from a point $\mathbf{x} = (x_1, x_2, x_3)$ to a point $\mathbf{X} = (X_1, X_2, X_3)$ in Cartesian coordinates, then it has undergone a displacement $\mathbf{u}(\mathbf{x}) = \mathbf{X}(\mathbf{x}) - \mathbf{x}$. The material is distorted in shape if the absolute distance between the particles changes. This distortion can be described as formulated by Every (2001), by choosing two particles in the solid at points \mathbf{x} and $\mathbf{x} + \delta\mathbf{x}$ which will be at $\mathbf{X}(\mathbf{x})$ and $\mathbf{X}(\mathbf{x} + \delta\mathbf{x})$ after the displacement. If we let the original distance between the particles be δl and δL be the distance after the displacement has taken

place then assuming that $\mathbf{X}(\mathbf{x}+\delta\mathbf{x})$ can be expanded in a Taylor series in δx_i , we can write,

$$\delta L^2 = |\mathbf{X}(\mathbf{x} + \delta\mathbf{x}) - \mathbf{X}(\mathbf{x})| = \frac{\partial X_k}{\partial x_l} \frac{\partial X_k}{\partial x_m} \delta x_l \delta x_m. \quad (l, m = 1, 2, 3) \quad (2.1)$$

The change in the square of the separation of the particles is thus given by

$$\delta L^2 - \delta l^2 = 2\eta_{lm} \delta x_l \delta x_m, \quad (2.2)$$

where

$$\eta_{lm} = \frac{1}{2} \left(\frac{\partial X_k}{\partial x_l} \frac{\partial X_k}{\partial x_m} - \delta_{lm} \right), \quad (2.3)$$

is called the Lagrangian or Almansi tensor and δ_{lm} is the Kronecker delta. The strain may also be expressed in terms of the displacement field gradients by

$$\eta_{lm} = \frac{1}{2} \left(\frac{\partial u_l}{\partial x_m} + \frac{\partial u_m}{\partial x_l} + \frac{\partial u_k}{\partial x_l} \frac{\partial u_k}{\partial x_m} \right). \quad (2.4)$$

For infinitesimal displacements, η_{lm} is equal, to first order in $\partial u_i / \partial x_m$, to the Cauchy strain tensor,

$$\varepsilon_{lm} = \frac{1}{2} \left(\frac{\partial u_l}{\partial x_m} + \frac{\partial u_m}{\partial x_l} \right). \quad (2.5)$$

In this thesis, we will be considering infinitesimal elastic strains and as a result our discussion will refer to the Cauchy strain tensor .

Stress is the force divided by the area on which the force acts. If we consider an infinitesimal cube centered at a point \mathbf{x} in a medium (see figure 2.1), then the Cauchy stress tensor has the nine components (Every, 2001),

$$\sigma_{ij} = \lim_{\delta A \rightarrow 0} \frac{\delta F_i^j}{\delta A} \quad (i, j = 1, 2, 3), \quad (2.6)$$

where δF_i^j is the i 'th component of the force acting across the surface facing outwards along the x_j direction and δA is the area of that face. The six off-

diagonal components of the stress tensor are the shear components whilst the three diagonal components are the normal components of stress.

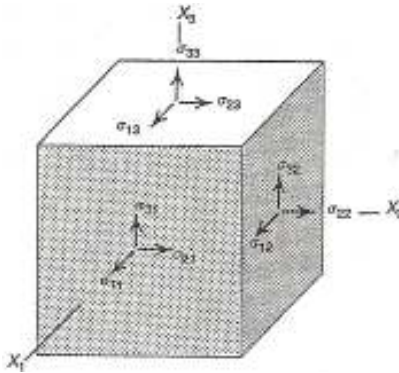


Figure 2.1. The force per unit area, σ_{ij} , transmitted across the faces pointing along the x_1 , x_2 and x_3 Cartesian directions.

We confine our attention to ideal solids which conform to Hooke's law, according to which stress and strain are related by the equation

$$\sigma_{ij} = C_{ijlm} \varepsilon_{lm}, \quad (2.7)$$

where C_{ijlm} is the fourth rank elastic modulus or stiffness tensor. The Einstein summation convention for repeated subscripts has been assumed.

The stress and strain tensors are symmetric with respect to interchange of their indices. This is because the moment of forces acting on the cubic element should tend to zero in the stress tensor to avoid infinite angular acceleration (Every, 2001). The strain tensor is symmetric by its definition (2.5). It follows that C_{ijlm} is invariant to interchange of i and j or l and m , i.e. $C_{ijlm} = C_{jilm} = C_{ijml} = C_{jml i}$. From elastic energy considerations it can be shown that $C_{ijlm} = C_{lmij}$. The number of independent elastic constants in any crystal is thus

reduced from 81 to 21 by the above mentioned index symmetries of the elastic stiffness tensor. The symmetry of the C_{ijkl} , also allows us to abbreviate the pairs of indices ij and lm into a single one running from 1 to 6. This is called Voigt contraction, in which the following association is made:

Original notation	11	22	33	23,32	31,13	12,21
Voigt contracted	1	2	3	4	5	6

The stress and strain components can now be written with a single suffix and we can rewrite Hooke's law in the form,

$$\sigma_I = C_{IJ} \varepsilon_J \quad (I, J = 1, 2, \dots, 6), \quad (2.8)$$

The presence of symmetry in the crystal can further reduce the number of independent C_{IJ} . In cubic crystals one ends up with only three independent constants, $C_{11} = C_{22} = C_{33}$, $C_{44} = C_{55} = C_{66}$ and $C_{12} = C_{23} = C_{13} = C_{21} = C_{32} = C_{31}$, all the others being zero.

2.2 Christoffel's equation

The particles of a solid under the influence of a uniform stress field and in cases where there are no body forces or torques do not experience any acceleration. A stress gradient however, results in the accelerated motion of these particles (Every, 2001). The resultant force acting across each one of the two faces normal to the x_1 , x_2 and x_3 directions of a cubic volume of side δx is given by,

$$\delta F_i = \frac{\partial \sigma_{ij}}{\partial x_j} \delta x^3. \quad (2.9)$$

Applying Newton's second law to equation (2.9), we obtain the equations of motion,

$$\frac{\partial \sigma_{ij}}{\partial x_j} = \rho \frac{\partial^2 u_i}{\partial t^2}, \quad (2.10)$$

where ρ is the density of the volume element. Combining this equation with Hooke's law, equation (2.7) we obtain,

$$\rho \frac{\partial^2 u_i}{\partial t^2} = \frac{\partial}{\partial x_j} (C_{ijlm} \varepsilon_{lm}). \quad (2.11)$$

Assuming homogeneity of C_{ijlm} we obtain the elastic wave equation for a general anisotropic solid,

$$\rho \frac{\partial^2 u_i}{\partial t^2} = C_{ijlm} \frac{\partial^2 u_l}{\partial x_j \partial x_m}. \quad (2.12)$$

Equation (2.12) admits plane wave solutions of the form, $u_i = U_i \exp[i(\mathbf{k} \cdot \mathbf{r} - \omega t)]$ subject to,

$$\rho \omega^2 U_i = C_{ijlm} k_j k_m U_l. \quad (2.13)$$

Equation (2.13) can be recast in the form,

$$[\Gamma_{il} - \rho v^2 \delta_{il}] U_l = 0, \quad (2.14)$$

where

$$\Gamma_{il} = C_{ijlm} n_j n_m,$$

Γ_{il} is the Christoffel matrix, $\mathbf{n} = \mathbf{k}/|\mathbf{k}|$ is the wave normal and δ_{il} is the Kronecker delta. Equation (2.14) is a set of three equations for the components of the unit polarization vector U_l , and is known as Christoffel's equation. The eigenvalues, v^2 , are the squares of the phase velocities, $v = \omega/k$, of the three modes of polarization of the acoustic waves. This gives us the secular equation for an elastic wave with wave normal direction (n_1, n_2, n_3) as

$$\begin{bmatrix} \Gamma_{11} - \rho v^2 & \Gamma_{12} & \Gamma_{13} \\ \Gamma_{21} & \Gamma_{22} - \rho v^2 & \Gamma_{23} \\ \Gamma_{31} & \Gamma_{32} & \Gamma_{33} - \rho v^2 \end{bmatrix} = 0, \quad (2.15)$$

where the subscripts 1, 2 and 3 represent the Cartesian coordinate axes. This determinantal equation is a cubic equation in v^2 and has roots corresponding to the longitudinal (L), slow transverse (ST) and fast transverse (FT) modes. The longitudinal mode generally has a higher velocity than the transverse modes because a compressional wave involves a local change of volume that gives a greater restoring force than the shear distortions of a transverse wave (Wolfe, 1998). For a general wave vector direction in an anisotropic solid we do not have pure longitudinal and transverse modes except along high symmetry directions. As a result, they are sometimes called quasi-longitudinal and quasi-transverse modes but here we shall use the compact notation, L, ST, and FT.

2.3 The slowness surface and group velocity

The slowness or inverse phase velocity vector is defined as $\mathbf{s} = \mathbf{k}/\omega$ with direction along \mathbf{k} . A radial plot of the locus of the slowness vectors gives the slowness surface. This surface has the shape of a constant frequency surface in \mathbf{k} space. The above definition of the slowness vector allows Christoffel's secular equation to be written in the form (Wolfe, 1998),

$$S(\mathbf{s}) = |C_{ijkl} s_j s_m - \rho \delta_{il}| = 0, \quad (2.16)$$

which is an equation of degree six in \mathbf{s} .

There are three sheets to the slowness surface corresponding to the L, FT and ST modes of acoustic wave propagation. Figure 2.1 shows a cross-section of the slowness surface for Si in the (100) plane and figure 2.2a shows a (110) cross

section. The slow transverse phase velocity is smaller than the fast transverse velocity for any given k -vector direction, and hence the ST sheet of the slowness surface lies on the outside. The L sheet lies entirely on the inside.

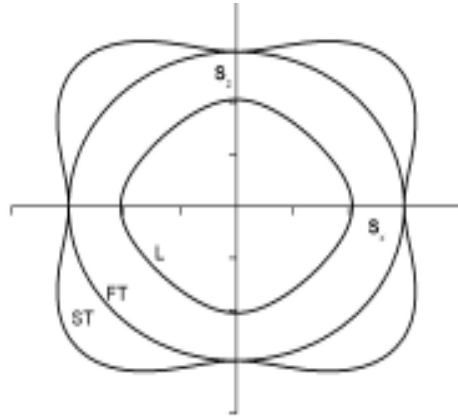


Figure. 2.2 . Cross section of the slowness surface for Si in the (010) plane.

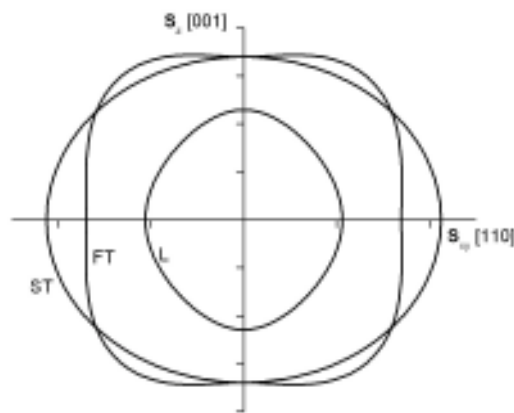


Figure. 2.3 . Cross section of the slowness surface of Si in the (110) plane.

Along the four fold $\langle 100 \rangle$ axes and threefold $\langle 111 \rangle$ axes, the ST and FT modes are degenerate. Axes along which the slowness surfaces have contact are called acoustic axes. Degeneracy can be conical, tangential, sporadic, triple degeneracy or in the form of lines of wedge shaped degeneracy (Every, 1986). For cubic crystals there is always tangential degeneracy along the [100]

directions and conical degeneracy along the [111] directions. The two transverse sheets are completely degenerate for an isotropic medium.



Figure. 2.4. Three dimensional ST sheet of the slowness surface for a Si crystal. Shaded regions are of saddle curvature and unshaded regions have convex or concave curvature (Calculated by A.G. Every).

In three dimensions the transverse sheets of the slowness surfaces have regions of positive and negative Gaussian curvature, see figure 2.3. The boundaries between such regions are parabolic lines of zero Gaussian curvature. It follows from the fact that the equation of the slowness surface is of degree six, that the inner longitudinal sheet is entirely convex. The significance of Gaussian curvature will become evident later.

The velocity of the modulation envelope of a wave packet is its group velocity. This is also parallel to the energy flux of the elastic wave and is the velocity of energy transmission (Wolfe, 1998). The group velocity of phonons in an elastically anisotropic medium is given by the gradient of $\omega(\mathbf{k})$ in k space,

$$\mathbf{V} = \nabla_{\mathbf{k}} \omega(\mathbf{k}) = \left(\frac{\partial \omega}{\partial k_1}, \frac{\partial \omega}{\partial k_2}, \frac{\partial \omega}{\partial k_3} \right). \quad (2.17)$$

Equation (2.17) implies that phonon group velocity vectors are normal to their constant frequency or slowness surface. As shown by Every (2001), this is because for any two neighboring points \mathbf{k} and $\mathbf{k} + \delta\mathbf{k}$ on a constant frequency

surface, $\omega(\mathbf{k} + \delta\mathbf{k}) - \omega(\mathbf{k}) = \delta\mathbf{k} \cdot \nabla_{\mathbf{k}} \omega(\mathbf{k}) = 0$. The collection of these group velocity vectors gives the group velocity or wave surface. The wave surface has a complex shape with folds corresponding to parabolic lines on the slowness surface as shown in figure 2.4 which shows a (100) section of the ST and FT sheets of the wave surface of Si.

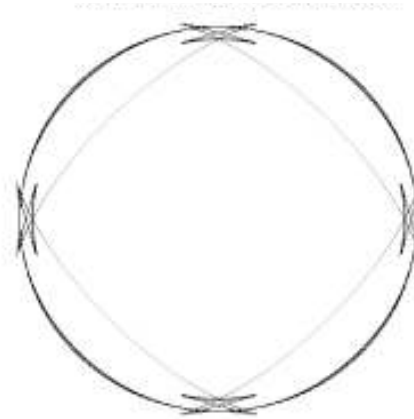


Figure. 2.5. Cross section of the ST and FT sheets of the wave surface for a Si crystal in the (100) plane.

The cross sections of the transverse wave surfaces in figure 2.4 were calculated by generating a large number of wave vectors and then calculating their corresponding group velocity vectors. Then those lying within an angle of 1° of the sectioning plane are represented graphically by dots. The sectioned folds show up as cusps in this diagram. The wave surface gives the shape of the heat pulse distribution emanating from a pulsed point source at some time after the pulse.

Folds on the wave surface originate from parabolic lines on the slowness surface where the Gaussian curvature is zero. This is because many of the wave vectors near the parabolic lines have nearly the same group velocity (Wolfe, 1998) and wave vectors can be found on the two sides of the parabolic line that have the same group velocity direction. The folds on the wave surface map

onto regions of infinite phonon focusing on the phonon image called caustics where the phonon flux is singular, as will be shown later.

2.4 Maris phonon enhancement factor

The focusing of phonons in crystals is due to the fact that waves with different wave vector directions can have almost the same group velocity vectors. We then have phonons tending to bunch up along certain directions (Wolfe, 1998). The Maris phonon enhancement factor is a useful measure for quantifying the angular variation in phonon intensity.

Let a phonon detector subtend a solid angle $d\Omega_V$ in real space as viewed from a point source of phonons. In an elastically isotropic solid, waves leaving the source with wave vectors in the same solid angle will reach the detector. However, in an anisotropic solid because wave vectors are not collinear with the group velocity vectors, waves leaving the source with wave vectors in a different solid angle, $d\Omega_k$, whose group velocities lie within the solid angle $d\Omega_V$ reach the detector (Maris, 1970). The ratio of the solid angle in wave vector space to the solid angle in real space,

$$A = \frac{d\Omega_k}{d\Omega_V}, \quad (2.18)$$

is called the Maris phonon enhancement factor.

When the enhancement factor is greater than unity then there is focusing of phonon i.e. greater intensity than there would be in a comparable isotropic medium, whilst there is defocusing if this factor is less than unity. There is no focusing of phonons in isotropic crystals since the wave vectors and group velocity vectors are parallel and $d\Omega_k = d\Omega_V$ resulting in $A = 1$. Calculations of the phonon enhancement factor along symmetry directions have been carried

out by Maris, 1971 and McCurdy, 1974. The Gaussian curvature of the slowness surface and the enhancement factor are related by (Every, 1981),

$$A = |s^3 VK|^{-1}, \quad (2.19)$$

where $K = L_1 L_2$ is the Gaussian curvature and L_1 and L_2 are the two principal curvatures of the slowness surface and s is the magnitude of slowness. So, the smaller the Gaussian curvature, the greater is the focusing. At parabolic lines, where K is zero, the phonon intensity is infinite and this maps onto a caustic in the phonon intensity.

2.5 Phase velocity along symmetry directions

There usually arises a need to check for the validity of phonon imaging and related calculations. This is because there is a possibility of obtaining reasonable results whilst the calculations have embedded errors. Expressions for the phase velocity along symmetry directions involve only the elastic constants and the density of the material and therefore one can obtain some expected results which can then be used to ascertain the validity of the calculations. Their derivation starts from the Christoffel matrix for a cubic crystal (Wolfe, 1998),

$$\begin{vmatrix} C_{11}k_x^2 + C_{44}(k_y^2 + k_z^2) - \rho\omega^2 & (C_{12} + C_{44})k_x k_y & (C_{12} + C_{44})k_x k_z \\ (C_{12} + C_{44})k_y k_x & C_{11}k_y^2 + C_{44}(k_x^2 + k_z^2) - \rho\omega^2 & (C_{12} + C_{44})k_y k_z \\ (C_{12} + C_{44})k_z k_x & (C_{12} + C_{44})k_z k_y & C_{11}k_z^2 + C_{44}(k_x^2 + k_y^2) - \rho\omega^2 \end{vmatrix} = 0, \quad (2.20)$$

or

$$\begin{vmatrix} C_{11}n_x^2 + C_{44}(n_y^2 + n_z^2) - \rho v^2 & (C_{12} + C_{44})n_x n_y & (C_{12} + C_{44})n_x n_z \\ (C_{12} + C_{44})n_y n_x & C_{11}n_y^2 + C_{44}(n_x^2 + n_z^2) - \rho v^2 & (C_{12} + C_{44})n_y n_z \\ (C_{12} + C_{44})n_z n_x & (C_{12} + C_{44})n_z n_y & C_{11}n_z^2 + C_{44}(n_x^2 + n_y^2) - \rho v^2 \end{vmatrix} = 0. \quad (2.21)$$

If one considers a wave normal directed along the [100] axis of a cubic crystal the wave normal components are $n_x=1$ and $n_y=n_z=0$. The off diagonal elements in equation (2.21) are zero and this gives us,

$$(C_{11} - \rho v^2)(C_{44} - \rho v^2)(C_{44} - \rho v^2) = 0. \quad (2.22)$$

The roots of this equation give us the velocity for the mode with longitudinal polarization,

$$v_L = \sqrt{\frac{C_{11}}{\rho}}, \quad (2.23)$$

and the two degenerate transverse polarization modes,

$$v_T = \sqrt{\frac{C_{44}}{\rho}}. \quad (2.24)$$

Along the [110] direction the wave normal components are $n_x=n_y=1/\sqrt{2}$ and $n_z=0$. Again from (2.21) the expressions for the phase velocities are,

$$v_L = \sqrt{\frac{(C_{11} + C_{12} + 2C_{44})}{2\rho}}, \quad (2.25)$$

$$v_{T1} = \sqrt{\frac{C_{44}}{\rho}}, \quad (2.26)$$

$$v_{T2} = \sqrt{\frac{(C_{11} - C_{12})}{2\rho}}. \quad (2.27)$$

Finally, for a wave normal directed along the [111] crystal axis, using the wave normal components $n_x=n_y=n_z=1/\sqrt{3}$ we have,

$$v_L = \sqrt{\frac{(C_{11} + 2C_{12} + 4C_{44})}{3\rho}}, \quad (2.28)$$

and

$$v_T = \sqrt{\frac{(C_{11} - C_{12} + C_{44})}{3\rho}}. \quad (2.29)$$

The condition among the elastic constants that corresponds to perfect isotropy is,

$$C_{11} - C_{12} - 2C_{44} = 0. \quad (2.30)$$

The degree of anisotropy of a crystal can be characterized by a dimensionless anisotropy factor defined by

$$\eta = \frac{2C_{44}}{(C_{11} - C_{12})}, \quad (2.31)$$

or

$$\Delta = (C_{11} - C_{12} - 2C_{44})/C_{44}. \quad (2.32)$$

For perfect isotropy, $\eta = 1$ and $\Delta = 0$. For a given anisotropy factor, the ratios of [100], [110] and [111] velocities for the transverse modes are determined.

2.6 Elastic parameter space

The phonon focusing pattern of a crystal depends only on the ratios of the elastic constants and not on the numerical values of each C_{ij} or the density of the material (Every, 1981). When the Christoffel matrix is divided by C_{44}/ρ , the resulting matrix depends on two parameters,

$$a = \frac{C_{11}}{C_{44}}, \quad (2.33)$$

and

$$b = \frac{C_{12}}{C_{44}}. \quad (2.34)$$

Using these ratios, one can plot an elastic parameter space of a versus b and map crystals according to the ratios of their elastic constants, see figure 2.6. A crystal must be located between the lines $a = -2b$ and $a = b$ in order to satisfy the thermodynamic constraints $C_{11} + 2C_{12} > 0$, $C_{11} > |C_{12}|$ and $C_{44} > 0$ (Nye, 1957). A crystal lying to the left of $a = -2b$ will have a negative bulk modulus and a crystal lying to the right of the line $a = b$ will have a negative shear modulus in certain orientations.

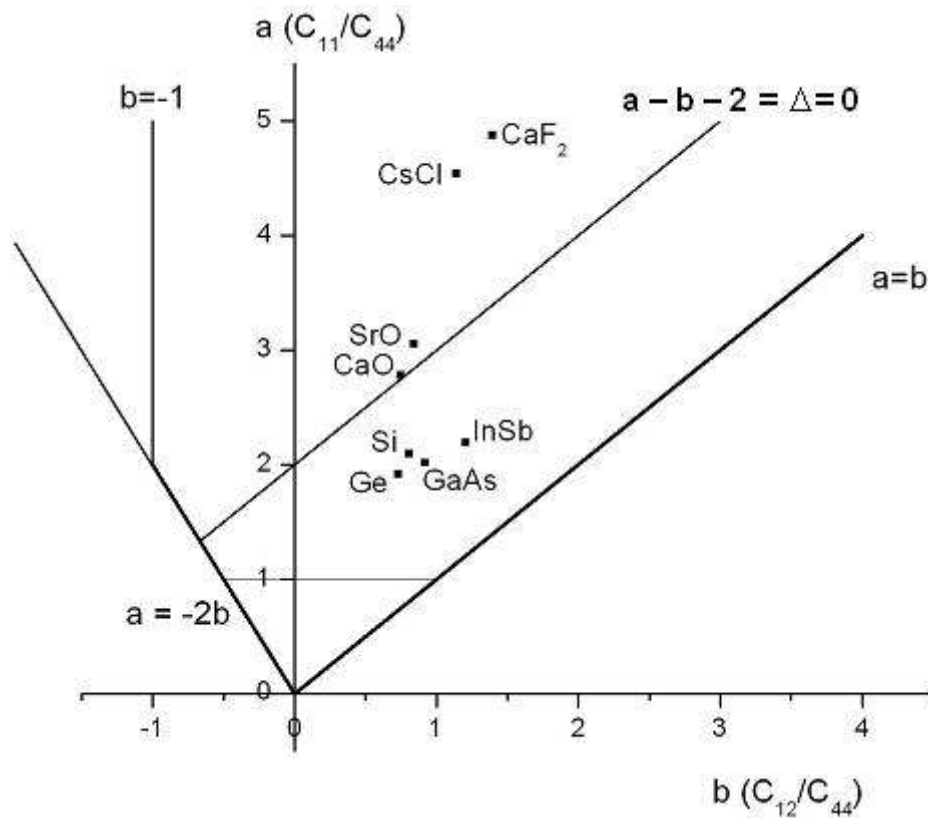


Figure. 2.6. Elastic parameter space for cubic crystals using elastic constants compiled by Every and McCurdy in the Landolt-Börnstein Series, (1992).

C_{11} is less than C_{44} in the region below the line $a = 1$ and for crystals satisfying this condition, the transverse phase velocities are higher than the longitudinal

velocity in the $\langle 100 \rangle$ directions. Transverse velocities again exceed the longitudinal phase velocities in the $\langle 111 \rangle$ directions in the area to the left of the line $b = -1$ where C_{12} is less than $-C_{44}$. Cases where the transverse velocities exceed the longitudinal velocities are rare and they have received relatively little attention as a result (Every and Stoddart, 1985). A line of points corresponding to the condition of elastic isotropy, $\Delta = 0$ cuts across the region of stability. Along this line the three sheets of the slowness surface are spherical and the two transverse sheets are completely degenerate. Materials lying to the left of the isotropy line can be classified as positive- Δ and those to the right of this line as negative- Δ crystals. Crystals lying on different sides of the isotropy line have different slowness surface topologies and phonon focusing patterns. The space below and above the isotropy line can be further divided into regions where different topologies appear on the slowness surfaces of the crystals. This has been done by Every, 1981 and Hurley and Wolfe, 1985. Figure 2.6 shows a cross section of the slowness surface of a positive- Δ crystal, CaF_2 , in the (110) plane, while Si depicted in figures 2.1 - 2.4 is a negative- Δ crystal.

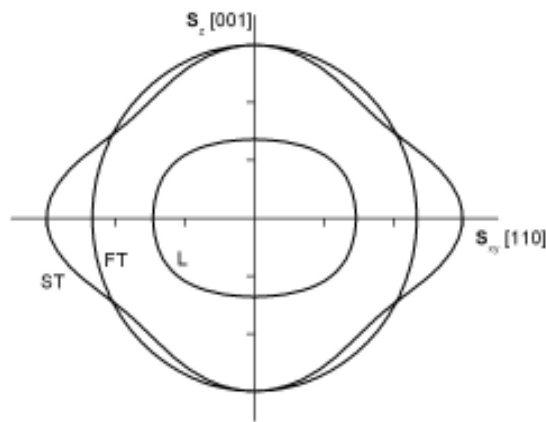


Figure 2.7. Cross section of the slowness surface for a positive- Δ crystal, CaF_2 , in the (110) plane.

2.7 Non-dispersive phonon focusing

In phonon imaging, phonon excitation is carried out in a crystal by heating a small spot on a metal film in transparent crystals or by heating the crystal surface of an opaque crystal directly using a pulsed laser or an electron beam. Investigations by Weis et al in 1969 and 1990 have shown that the frequency distribution of the non-equilibrium phonons can be modeled as Planckian. Long wavelength phonon focusing patterns of cubic crystals are calculated using a program written in the FORTRAN programming language. We first generate \mathbf{k} vectors with an isotropic distribution of directions in \mathbf{k} space. For each of these wave normals, we calculate the roots of the cubic equation in $\lambda = \rho\omega^2$,

$$-\lambda^3 + c(\mathbf{k})\lambda^2 + d(\mathbf{k})\lambda + e(\mathbf{k}) = 0, \quad (2.35)$$

derived from (2.20) using a root finding procedure, Laguer, (Press et al, 1986).

The coefficients of this equation are,

$$\begin{aligned} c(\mathbf{k}) &= Q + T + S, \\ d(\mathbf{k}) &= T^2 + U^2 + V^2 - SQ - SR - QR, \\ e(\mathbf{k}) &= QRS - V^2U - T^2S - U^2R + 2TUV. \end{aligned}$$

Q, T and S are the diagonal components of equation (2.20) for a crystal with cubic symmetry defined as,

$$\begin{aligned} Q &= C_{11}k_x^2 + C_{44}(k_y^2 + k_z^2), \\ S &= C_{11}k_z^2 + C_{44}(k_x^2 + k_y^2), \\ R &= C_{11}k_y^2 + C_{44}(k_x^2 + k_z^2), \end{aligned}$$

and the off-diagonal components T, U and V are given by,

$$\begin{aligned} T &= k_x k_y (C_{12} + C_{44}), \\ U &= k_x k_z (C_{12} + C_{44}), \\ V &= k_y k_z (C_{12} + C_{44}). \end{aligned}$$

The roots of equation (2.35) give us the frequencies, ω , of each wave vector. We then compute the corresponding group velocity vectors, \mathbf{V}_g , for each phonon wave vector. This is done by finding the gradient of (2.35) and we obtain the following expression for the group velocity,

$$\mathbf{V}_g = \nabla_{\mathbf{k}} \omega(\mathbf{k}) = \frac{\frac{\partial e(\mathbf{k})}{\partial \mathbf{k}} + \lambda \frac{\partial d(\mathbf{k})}{\partial \mathbf{k}} + \lambda^2 \frac{\partial c(\mathbf{k})}{\partial \mathbf{k}}}{3\lambda^2 - 2\lambda c(\mathbf{k}) - d(\mathbf{k})} \times \frac{1}{2\rho\omega}. \quad (2.36)$$

The points where the ray or group velocity vectors pass through the observation plane are sorted into a 500×500 array of bins. The number of vectors falling into each bin is counted and this is output in matrix form in a file that is saved in data format. A high density of the ray vectors in any direction represents strong phonon focusing. The data file is imported into the software Origin 6.1 where we plot a gray scale image representing the phonon image. Phonon focusing patterns of a positive $-\Delta$ crystal, CaF_2 are shown in figure 2.7. The phonon focusing structures in these images are due to slow transverse and fast transverse phonons only, we do not include L phonons in our calculations since they do not give rise to caustics for reasons touched on earlier. The images in the (100) and (110) planes span an angle of 90° whilst the image in the (111) plane spans an angle of 53.13° from left to right. The image in the (111) observation plane, figure 2.7a is centered around the $\langle 111 \rangle$ direction. Figure 2.7b is centered around the $\langle 100 \rangle$ direction and figure 2.7c is centered around the $\langle 110 \rangle$ direction. Bright areas in these phonon images represent high phonon intensity. This is all we will have to say about positive- Δ crystals. Most of the experimental investigations on the dispersive phonon focusing patterns of crystals have pertained to negative- Δ crystals and for this reason, in the remainder of this thesis we study the phonon images of negative $-\Delta$ crystals.

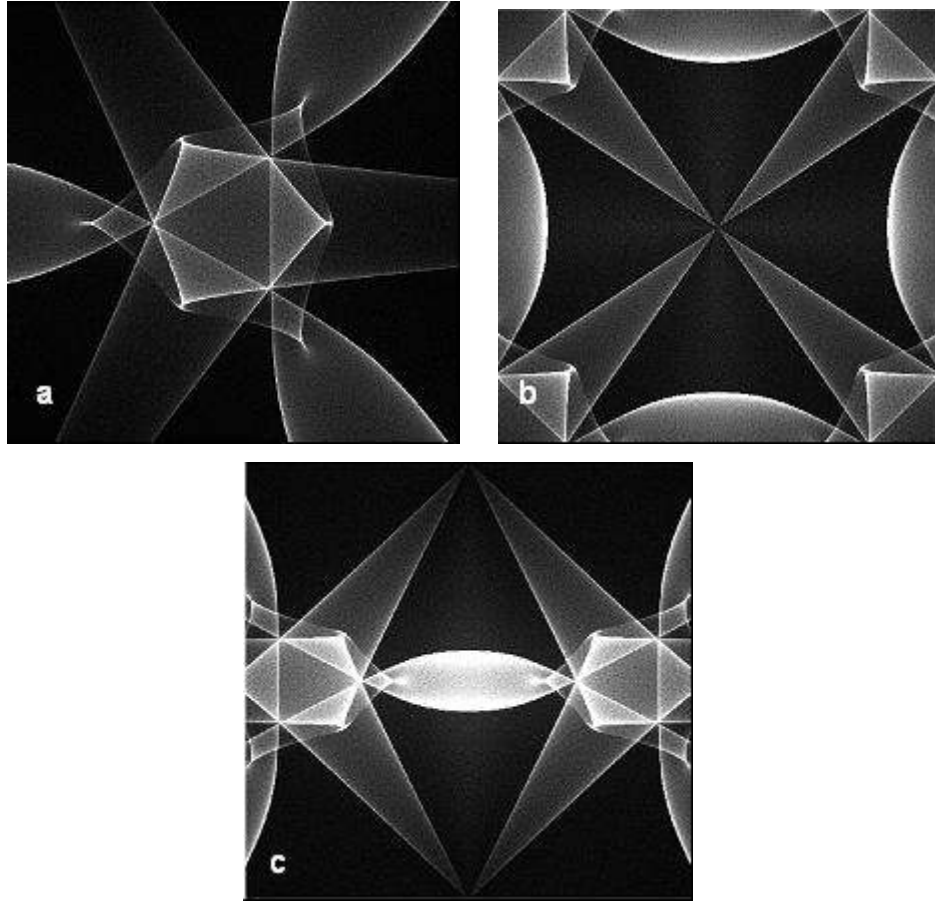


Figure. 2.8. Non dispersive FT and ST phonon focusing pattern of CaF_2 , a positive- Δ crystal, in the (a) (111) with an angular width of 53.13° , (b) (100) and (c) (110) observation planes with angular widths of 90° from left to right.

To calculate the phonon images in figure 2.7, we used a density of $3.21 \times 10^3 \text{ kg m}^{-3}$ (Wolfe, 1998) and the elastic constants in units of $\text{kg m}^{-1} \text{ s}^{-2}$ are $C_{11} = 1.65 \times 10^{11}$, $C_{12} = 0.473 \times 10^{11}$ and $C_{44} = 0.339 \times 10^{11}$, tabulated by Every and McCurdy in the Landolt-Börnstein series in 1992.

Chapter 3

Dispersive phonons in cubic crystals

Spatial dispersion is the variation of acoustic wave speed with wavelength (Mittal and Every, 2007). It sets in when the wavelength becomes comparable to the lattice parameter in a crystal. Various lattice dynamics models have been used to explain the changes in the phonon focusing patterns of crystals as a result of dispersion. These include the bond charge model (Rustagi and Weber, 1976), the shell model (Dolling and Waugh, 1965), the deformation dipole model (Kunc et al, 1975) and the valence force field model (Price et al, 1971). These models have had mixed success in accounting for the measured focusing patterns of a number of crystals (Wolfe, 1998).

In this thesis, we attempt to explain the first onset of spatial dispersion within continuum elasticity theory by the inclusion of third and fourth order spatial derivatives of the displacement field in the elastic wave equation (DiVincenzo, 1986). This adaptation of continuum elasticity gives us a formulation that applies to many types of solids and removes the need for one to construct a specific microscopic model for each medium (Every and Jakata, 2007). Our approach is applicable in principle to crystals of any symmetry, but the examples we treat are limited to crystals of cubic symmetry. For our investigations, we have chosen two crystals belonging to the crystal class (point symmetry group) O_h with a centre of inversion namely, germanium and silicon, and two crystals belonging to the crystal class T_d which lacks a centre of inversion namely, indium antimonide and gallium arsenide.

3.1 Extension of continuum elasticity theory to include dispersive effects

Phonon imaging of long wavelength elastic waves has been explained by continuum elasticity theory in the previous chapter. Higher frequency phonons are sensitive to the discrete nature of the crystal and the dispersion relation is non-linear. The classical wave equation given in section 2.2 can be modified within continuum elasticity theory to accommodate the effects of spatial dispersion as done by DiVincenzo in 1986. One starts from the elastodynamic Lagrangian density for a solid,

$$L = \frac{1}{2} \rho \frac{\partial u_i}{\partial t} \frac{\partial u_i}{\partial t} - \frac{1}{2} C_{ijlm} \frac{\partial u_i}{\partial x_j} \frac{\partial u_l}{\partial x_m} - D_{ijlmn} \frac{\partial u_i}{\partial x_j} \frac{\partial^2 u_l}{\partial x_m \partial x_n} - F^1_{ijlmnk} \frac{\partial u_i}{\partial x_j} \frac{\partial^3 u_l}{\partial x_m \partial x_n \partial x_k} - F^2_{ijlmnk} \frac{\partial^2 u_i}{\partial x_j \partial x_m} \frac{\partial^3 u_l}{\partial x_n \partial x_k} - \dots \quad (3.1)$$

This assumes that L is translationally invariant, time independent, and invariant under inversion and time reversal, and that the displacement field is infinitesimal so that L is a quadratic function of the displacement derivatives. The first term on the right hand side represents the kinetic energy whilst the remaining terms represent the potential energy. The coefficients of the second term, C_{ijlm} , are the non-dispersive elastic constants. The coefficients of the higher order terms, D_{ijlmn} and F_{ijlmnk} , are the dispersive elastic constants. For the action to be stationary (Goldstein, 1950),

$$\delta A = \delta \left(\int L dx dt \right) = 0. \quad (3.2)$$

As shown by DiVincenzo, the wave equation is obtained by integrating (3.2) by parts with the following result,

$$\rho \frac{\partial^2 u_i}{\partial t^2} = c_{ijlm} \frac{\partial^2 u_l}{\partial x_j \partial x_m} + d_{ijlmn} \frac{\partial^3 u_l}{\partial x_j \partial x_m \partial x_n} - f_{ijklmn} \frac{\partial^4 u_l}{\partial x_j \partial x_m \partial x_n \partial x_k}. \quad (3.3)$$

The coefficients c_{ijlm} , d_{ijlmn} and f_{ijklmn} are related to the static constants C_{ijlm} , D_{ijlmn} and F_{ijklmn} by symmetrisation's or anti-symmetrisation's of indices (Lax, 1974),

$$c_{ijlm} = \text{sym}_{(i,l)} \text{sym}_{(j,m)} C_{ijlm}, \quad (3.4)$$

$$d_{ijlmn} = \text{asym}_{(i,l)} \text{sym}_{(j,m,n)} D_{ijlmn}, \quad (3.5)$$

$$f_{ijklmn} = \text{sym}_{(i,l)} \text{sym}_{(j,k,m,n)} (F_{ijklmn}^1 - F_{ijklmn}^2). \quad (3.6)$$

The symmetrisation's and anti-symmetrisation's in the equations (3.4), (3.5) and (3.6) arise because of the terms generated through integration by parts (DiVincenzo, 1986).

Assuming a plane wave solution to equation (3.3) of the form $u_i = U_i \exp[i(\mathbf{k} \cdot \mathbf{r} - \omega t)]$, we obtain the linear equations for the polarization vector U_k ,

$$\{c_{ijlm} k_j k_m + i d_{ijlmn} k_j k_m k_n + f_{ijlmnk} k_j k_m k_n k_k - \rho \omega^2 \delta_{il}\} U_l = 0, \quad (3.7)$$

and the secular equation,

$$\det \left| c_{ijlm} k_j k_m + i d_{ijlmn} k_j k_m k_n + f_{ijlmnk} k_j k_m k_n k_k - \rho \omega^2 \delta_{il} \right| = 0, \quad (3.8)$$

that represents the dispersion relation $\Omega(\mathbf{k}, \omega) = 0$.

In chapter 2 it was pointed out that in crystals of cubic symmetry, the elastic tensor c_{ijlm} has three independent components which we take as $c_{1111} = C_{11}$, $c_{1122} = C_{12}$ and $c_{1212} = C_{44}$. The fifth rank tensor d_{ijlmn} is called the acoustic gyrotropic tensor and is implicated in the rotation of the plane of polarisation of a transverse acoustic wave along an acoustic axis. All components of this tensor vanish in crystals with a centre of inversion, whilst this is not the case

for non-centrosymmetric crystal classes like the point group T_d (Portugal et al 1968).

Crystal symmetry and group theory considerations can be used to reduce the number of independent components in the d and f tensors. It is found that there is only one independent component of the d_{ijklmn} tensor for the point group T_d , which is zero for the point group O_h , and six independent components of the f_{ijklmn} tensor (DiVincenzo, 1986) for both point symmetry groups T_d and O_h . We call the single component of the d_{ijklmn} tensor the dispersive elastic constant d and the six independent components of the tensor f_{ijklmn} we call f_1, f_2, f_3, f_4, f_5 , and f_6 .

If equation 3.7 is written in the form,

$$\rho\omega^2 U_i = D_{il} U_l,$$

then the components of the dynamical matrix are given by (DiVincenzo, 1986),

$$D_{ii} = C_{11}k_i^2 + C_{44}(k_j^2 + k_k^4) + f_1k_i^4 + f_2(k_j^4 + k_k^4) + 6f_3k_j^2k_k^2 + 6f_4k_i^2(k_j^2 + k_k^2), \quad (3.9)$$

and,

$$D_{il} = (C_{12} + C_{44})k_i k_j + 3id(k_i^2 k_k - k_j^2 k_k) + 4f_5(k_i k_j^3 + k_i^3 k_j) + 12f_6(k_i k_j k_k^2), \quad i \neq l. \quad (3.10)$$

The subscripts i, j and k refer to the Cartesian directions and no summation is implied by repeated indices in these expressions and $i \neq j, j \neq k$ and $k \neq i$.

We can therefore write the dispersion relation in the form,

$$\Omega(\mathbf{k}, \omega) = \begin{vmatrix} Q - \lambda & T + iT' & U - iU' \\ T - iT' & R - \lambda & V + iV' \\ U + iU' & V - iV' & S - \lambda \end{vmatrix} = 0 \quad (3.11)$$

where again $\lambda = \rho\omega^2$ and for the diagonal components are,

$$\begin{aligned} Q &= C_{11}k_x^2 + C_{44}(k_y^2 + k_z^2) + f_1k_x^4 + f_2(k_y^4 + k_z^4) + 6f_3k_y^2k_z^2 + 6f_4k_x^2(k_y^2 + k_z^2), \\ R &= C_{11}k_y^2 + C_{44}(k_x^2 + k_z^2) + f_1k_y^4 + f_2(k_x^4 + k_z^4) + 6f_3k_x^2k_z^2 + 6f_4k_y^2(k_x^2 + k_z^2), \\ S &= C_{11}k_z^2 + C_{44}(k_x^2 + k_y^2) + f_1k_z^4 + f_2(k_x^4 + k_y^4) + 6f_3k_x^2k_y^2 + 6f_4k_z^2(k_x^2 + k_y^2), \end{aligned}$$

and the off-diagonal components, T, U, V, T', U' and V' are given by,

$$\begin{aligned} T &= (C_{12} + C_{44})k_xk_y + 4f_5(k_xk_y^3 + k_x^3k_y) + 12f_6k_xk_yk_z^2, \\ U &= (C_{12} + C_{44})k_xk_z + 4f_5(k_xk_z^3 + k_x^3k_z) + 12f_6k_xk_zk_y^2, \\ V &= (C_{12} + C_{44})k_yk_z + 4f_5(k_yk_z^3 + k_y^3k_z) + 12f_6k_yk_zk_x^2, \\ T' &= 3dk_z(k_x^2 - k_y^2), \\ U' &= 3dk_y(k_z^2 - k_x^2), \\ V' &= 3dk_x(k_y^2 - k_z^2). \end{aligned}$$

From equation (3.11) we come up with the cubic expression in $\lambda = \rho\omega^2$,

$$-\lambda^3 + c(\mathbf{k})\lambda^2 + d(\mathbf{k})\lambda + e(\mathbf{k}) = 0, \quad (3.12)$$

where the coefficients $c(\mathbf{k}), d(\mathbf{k})$ and $e(\mathbf{k})$ are given by,

$$c(\mathbf{k}) = Q + R + S,$$

$$d(\mathbf{k}) = T^2 + T'^2 + U^2 + U'^2 + V^2 + V'^2 - QR - RS - SQ,$$

$$e(\mathbf{k}) = QRS - T^2S - T'^2S - U^2R - U'^2R - V^2Q - V'^2Q + 2TUV - 2TUV' - 2T'UV' - 2T'UV.$$

For a given wave vector, the gradient of (3.12) gives the group velocity.

3.2 Dispersion relations along symmetry directions

Using equations (3.9) and (3.10) we can derive analytical expressions relating the wave vector and the frequency in the $\langle 100 \rangle$, $\langle 111 \rangle$ and $\langle 110 \rangle$ symmetry directions. For the $\langle 100 \rangle$ directions where the wave vector components are

$k = k_x$, $k_y = 0$ and $k_z = 0$ the dynamic matrix has only got components along the diagonal and is given by,

$$\begin{vmatrix} C_{11}k^2 + f_1k^4 - \lambda & 0 & 0 \\ 0 & C_{44}k^2 + f_2k^4 - \lambda & 0 \\ 0 & 0 & C_{44}k^2 + f_2k^4 - \lambda \end{vmatrix} = 0. \quad (3.13)$$

This gives us the dispersion relation for the longitudinal mode along the $\langle 100 \rangle$ axis as

$$\frac{\rho\omega_L^2}{k^2} = C_{11} + f_1k^2, \quad (3.14)$$

and for the two degenerate transverse modes we have,

$$\frac{\rho\omega_T^2}{k^2} = C_{44} + f_2k^2. \quad (3.15)$$

The subscripts L and T denote longitudinal and transverse modes of wave propagation respectively. Along the threefold $\langle 111 \rangle$ axis, where the wave vector components along the coordinate axes are equal, $k_x = k_y = k_z = k/\sqrt{3}$, the diagonal components of the dynamic matrix are given by

$$Q = D_{xx} = D_{yy} = D_{zz} = C_{11} \frac{k^2}{3} + 2C_{44} \frac{k^2}{3} + f_1 \frac{k^4}{9} + 2f_2 \frac{k^4}{9} + 6f_3 \frac{k^4}{9} + 12f_4 \frac{k^4}{9}, \quad (3.16)$$

and the off diagonal components are given by,

$$T = D_{ij} = (C_{12} + C_{44}) \frac{k^2}{3} + 8f_5 \frac{k^4}{9} + 12f_6 \frac{k^4}{9}, \quad (3.17)$$

where the subscripts i and j represent Cartesian coordinates x, y and z with $i \neq j$. Using this dynamical matrix we can derive the dispersion relation for the pure longitudinal mode from,

$$\begin{pmatrix} Q & T & T \\ T & Q & T \\ T & T & Q \end{pmatrix} \begin{pmatrix} 1 \\ 1 \\ 1 \end{pmatrix} = \lambda \begin{pmatrix} 1 \\ 1 \\ 1 \end{pmatrix}. \quad (3.18)$$

Equation (3.18) gives us the expression, $\lambda = Q + 2T$, from which we obtain the dispersion relation for the L mode as,

$$\frac{\rho\omega_L^2}{k^2} = \frac{1}{3}(C_{11} + 2C_{12} + 4C_{44}) + \frac{k^2}{9}(f_1 + 2f_2 + 6f_3 + 12f_4 + 16f_5 + 24f_6). \quad (3.19)$$

We obtain the two degenerate transverse modes from,

$$\begin{pmatrix} Q & T & T \\ T & Q & T \\ T & T & Q \end{pmatrix} \begin{pmatrix} 1 \\ -1 \\ 0 \end{pmatrix} = \lambda \begin{pmatrix} 1 \\ -1 \\ 0 \end{pmatrix}. \quad (3.20)$$

This gives us the expression $\lambda = Q - T$, and the dispersion relation for the T modes are,

$$\frac{\rho\omega_T^2}{k^2} = \frac{1}{3}(C_{11} - C_{12} + C_{44}) + \frac{k^2}{9}(f_1 + 2f_2 + 6f_3 + 12f_4 - 8f_5 - 12f_6). \quad (3.21)$$

Along the $\langle 110 \rangle$ crystal axes where the wave vector components along the coordinate axis are $k_x = k_y = k/\sqrt{2}$ and $k_z = 0$, the dynamical matrix has the form,

$$\begin{pmatrix} Q & T & -iU' \\ T & Q & -iU' \\ iU' & iU' & S \end{pmatrix}, \quad (3.22)$$

where the Q, T, U and S components of this matrix are given by,

$$Q = \frac{k^2}{2}(C_{11} + C_{44}) + \frac{k^4}{4}(f_1 + f_2 + 6f_4), \quad (3.23)$$

$$S = 2C_{44} \frac{k^2}{2} + \frac{k^4}{4} (2f_2 + 6f_3), \quad (3.24)$$

$$T = \frac{k^2}{2} (C_{12} + C_{44}) + 8f_5 \frac{k^4}{4}, \quad (3.25)$$

$$U' = \frac{-3dk^3}{2\sqrt{2}}. \quad (3.26)$$

One of the transverse modes is mixed with the longitudinal mode along the $\langle 110 \rangle$ direction. This leads to modes with elliptical polarization and so we derive dispersion relations for the two mixed modes along the $\langle 110 \rangle$ direction from,

$$\begin{pmatrix} Q & T & -iU' \\ T & Q & -iU' \\ iU' & iU' & S \end{pmatrix} \begin{pmatrix} \alpha \\ \alpha \\ \beta \end{pmatrix} = \lambda \begin{pmatrix} \alpha \\ \alpha \\ \beta \end{pmatrix}. \quad (3.27)$$

This gives us the equation,

$$\rho\omega^2 = \frac{(Q+T+S)}{2} \pm \frac{\left[(Q+T-S)^2 + 8U'^2 \right]^{\frac{1}{2}}}{2}, \quad (3.28)$$

with the positive sign pertaining to the longitudinal mode and the negative sign pertaining to the transverse mode. For crystals with a centre of inversion, for example Ge and Si, where $d=0$ and so $U'=0$ in (3.28) we obtain the expressions,

$$\rho\omega_L^2 = (C_{11} + C_{12} + 2C_{44}) \frac{k^2}{2} + (f_1 + f_2 + 6f_4 + 8f_5) \frac{k^4}{4}, \quad (3.29)$$

and

$$\rho\omega_{T1}^2 = C_{44}k^2 + (f_2 + 3f_3) \frac{k^4}{2}. \quad (3.30)$$

In crystals without a centre of inversion where $d \neq 0$ one can only obtain simple expressions like (3.29) and (3.30) as an approximation and this does not give a good fit to the experimental data. We have used the exact expression,

equation (3.28), to fit the dispersion parameters to the neutron scattering data for InSb and GaAs which do not have a centre of inversion.

We finally derive the expression for the other non-degenerate pure transverse mode along the $\langle 110 \rangle$ directions from,

$$\begin{pmatrix} Q & T & -iU \\ T & Q & -iU \\ iU & iU & S \end{pmatrix} \begin{pmatrix} 1 \\ -1 \\ 0 \end{pmatrix} = \lambda \begin{pmatrix} 1 \\ -1 \\ 0 \end{pmatrix}. \quad (3.31)$$

Equation (3.31) gives us the dispersion relation,

$$\frac{\rho\omega_{T2}^2}{k^2} = \frac{1}{2}(C_{11} - C_{12}) + \frac{k^2}{4}(f_1 + f_2 + 6f_4 - 8f_5). \quad (3.32)$$

3.3 Determination of elastic constants and dispersion parameters of crystals with a centre of inversion

Neutron scattering experiments provide frequency versus wave vector data along symmetry directions in crystals from which we can infer the elastic constants and dispersion parameters. We have extracted wave vector k up to 0.4 in reduced wave vector coordinates versus frequency, ω , for germanium and silicon. Wave vector k is in units of $2\pi/a$, where a is the lattice parameter of the crystal. For germanium, data was obtained from Nilsson and Nelin (1971). We obtained data for silicon for the $\langle 100 \rangle$, $\langle 111 \rangle$ directions and for the longitudinal and one of the transverse acoustic modes in the $\langle 110 \rangle$ directions from Dolling (1963). Data for the remaining transverse acoustic mode in silicon was extracted from Nilsson and Nelin (1972).

The extracted data gives us the origin plus two points on each acoustic dispersion curve along each symmetry direction for the limited range of k we are considering. This data, frequency, ω , versus wave vector k , is then

inserted into the appropriate dispersion relation and solved for the relevant elastic constant (combination) and dispersion parameter (combination). In this way we obtain numerical values h_i for the following combinations of the non-dispersive elastic constants:

$$\begin{aligned}
C_{11} &= h_1 \\
C_{44} &= h_2 \\
\frac{1}{3}(C_{11} + 2C_{12} + 4C_{44}) &= h_3 \\
\frac{1}{3}(C_{11} - C_{12} + C_{44}) &= h_4 \\
\frac{1}{2}(C_{11} + C_{12} + 2C_{44}) &= h_5 \\
C_{44} &= h_6 \\
\frac{1}{2}(C_{11} - C_{12}) &= h_7
\end{aligned}$$

and numerical values g_i for the following combinations of the dispersive elastic constants:

$$\begin{aligned}
f_1 &= g_1 \\
f_2 &= g_2 \\
\frac{1}{9}(f_1 + 2f_2 + 6f_3 + 12f_4 + 16f_5 + 24f_6) &= g_3 \\
\frac{1}{9}(f_1 + 2f_2 + 6f_3 + 12f_4 - 8f_5 - 12f_6) &= g_4 \\
\frac{1}{4}(f_1 + f_2 + 6f_4 + 8f_5) &= g_5 \\
\frac{1}{2}(f_2 + 3f_3) &= g_6 \\
\frac{1}{4}(f_1 + f_2 + 6f_4 - 8f_5) &= g_7
\end{aligned}$$

These fourteen equations have nine parameters, three non-dispersive elastic constants and six dispersive elastic constants. This is an over determined problem which has been solved by optimization. We performed the optimisation of the non-dispersive elastic constants separately from that of the dispersive elastic constants because of the large numbers of parameters involved. The tabulated values of the non-dispersive elastic constants of Ge in

units of $\text{kg m}^{-1} \text{s}^{-2}$ are $C_{11} = 1.29 \times 10^{11}$, $C_{12} = 0.48 \times 10^{11}$ and $C_{44} = 0.671 \times 10^{11}$. For Si they are $C_{11} = 1.65 \times 10^{11}$, $C_{12} = 0.63 \times 10^{11}$ and $C_{44} = 0.791 \times 10^{11}$ all in units of $\text{kg m}^{-1} \text{s}^{-2}$ (Every and McCurdy in Landolt-Börnstein Series, 1992). We used a chi-square optimization technique where we varied the three non-dispersive elastic constants within ± 40 of the tabulated values while calculating the “theoretical” values of h_i which we call H_i for each set of constants. We then summed the squares of the differences between the h_i 's and the H_i 's and obtain χ^2 ,

$$\chi^2 = \sum_{i=1}^7 (h_i - H_i)^2.$$

We adopt the set of elastic constants at the point where we obtained a minimum value of χ^2 . These values for Ge and Si are listed in table 3.1 and 3.2 respectively.

We followed the same procedure for the dispersive elastic constants. In this case we started by varying the values of f_1, f_2, f_3, f_4, f_5 and f_6 between -1×10^{-8} and 1×10^{-8} in units of kg m s^{-2} . For each set of values of these dispersive parameters we obtained “theoretical” values of g_i , which we call G_i and calculated the sum of the difference between the g_i and G_i to obtain,

$$\chi^2 = \sum_{i=1}^7 (g_i - G_i)^2.$$

We took the values of the dispersive elastic constants at the point where χ^2 had its minimum value.

3.3.1 Elastic constants, dispersion parameters and dispersion curves of Ge

Using the seven dispersion relations derived in section 3.2 we fitted the calculated dispersion curves to the neutron scattering data. We used a density of $5.34 \times 10^3 \text{ kg m}^{-3}$ (Wolfe, 1998) and a lattice parameter of 5.65\AA (Kittel, 1956) for calculations on germanium. Using this procedure, the non-dispersive and dispersive elastic constants of germanium obtained are shown in the left hand column of table 3.1. The non-dispersive elastic constants of Ge obtained using these procedures are all slightly larger than the tabulated values. However, it is the anisotropy factor, η , which determines the phonon focusing pattern. The value obtained from the tabulated values is 0.604 whilst the one obtained from the elastic constants extracted directly from neutron scattering data is 0.595 which is in good agreement with the one obtained from the tabulated values.

Elastic constants of Ge have also been obtained by Maranganti et al (2007) through the intermediary of the shell lattice dynamics model. On the basis of this model they constructed the dynamical matrix whose parameters they adjusted to fit their full set of calculated dispersion curves for the entire Brillouin zone to the neutron scattering data of Dolling et al, 1963. From the dynamical matrix they then obtained the non-dispersive and dispersive elastic constants. The elastic constants and dispersion parameters of Ge obtained in this way are also shown in table 3.1, in the right hand column.

The comparison of the acoustic mode dispersion curves obtained from continuum theory with parameters determined directly from experimental neutron scattering data is shown in figure 3.1 for germanium. The wave vector coordinates are in the reduced wave vector form. The data points in the

dispersion curves represent the experimental neutron scattering data extracted from Nilsson and Nelin (1971).

Ge (<i>neutron scattering</i>)	Ge (<i>shell model</i>)
$C_{11} = 1.3908 \times 10^{11} \text{ (kg m}^{-1} \text{ s}^{-2}\text{)}$	$C_{11} = 1.310 \times 10^{11} \text{ (kg m}^{-1} \text{ s}^{-2}\text{)}$
$C_{12} = 0.560 \times 10^{11} \text{ (kg m}^{-1} \text{ s}^{-2}\text{)}$	$C_{12} = 0.3000 \times 10^{11} \text{ (kg m}^{-1} \text{ s}^{-2}\text{)}$
$C_{44} = 0.698 \times 10^{11} \text{ (kg m}^{-1} \text{ s}^{-2}\text{)}$	$C_{44} = 0.6800 \times 10^{11} \text{ (kg m}^{-1} \text{ s}^{-2}\text{)}$
$f_1 = -8.029 \times 10^{-10} \text{ (kg m s}^{-2}\text{)}$	$f_1 = -0.800 \times 10^{-10} \text{ (kg m s}^{-2}\text{)}$
$f_2 = -15.060 \times 10^{-10} \text{ (kg m s}^{-2}\text{)}$	$f_2 = -25.200 \times 10^{-10} \text{ (kg m s}^{-2}\text{)}$
$f_3 = -0.077 \times 10^{-10} \text{ (kg m s}^{-2}\text{)}$	$f_3 = -6.300 \times 10^{-10} \text{ (kg m s}^{-2}\text{)}$
$f_4 = -4.892 \times 10^{-10} \text{ (kg m s}^{-2}\text{)}$	$f_4 = -0.300 \times 10^{-10} \text{ (kg m s}^{-2}\text{)}$
$f_5 = -4.387 \times 10^{-10} \text{ (kg m s}^{-2}\text{)}$	$f_5 = -0.100 \times 10^{-10} \text{ (kg m s}^{-2}\text{)}$
$f_6 = 3.197 \times 10^{-10} \text{ (kg m s}^{-2}\text{)}$	$f_6 = 2.900 \times 10^{-10} \text{ (kg m s}^{-2}\text{)}$

Table 3.1. Non-dispersive and dispersive elastic constants of germanium obtained by fitting to neutron scattering data to the continuum model versus a shell model.

For Ge, continuum elasticity theory fits well the experimental dispersion relation data for the symmetry directions up to $k = 0.4$ but not much beyond that, particularly for the transverse modes. The breakdown beyond $k = 0.4$ is expected because the extension of continuum theory involves a truncated Taylor series expansion of the real microscopic lattice dynamics which must eventually fail (DiVincenzo, 1986 and Krumhansl, 1968). This model is therefore limited to the first bending over of the dispersion relation as we have emphasised all along. It does not apply to near Brillouin zone boundary phonons. These do not in any case have a significant effect in phonon imaging because of their small group velocities and high scattering probabilities.

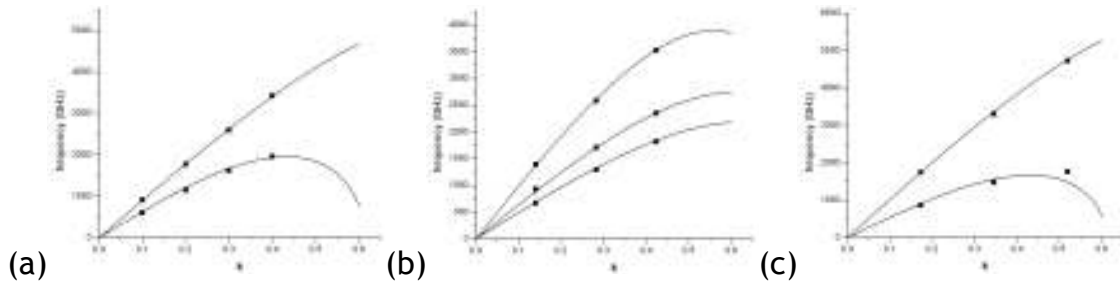


Figure 3.1 Dispersion curves of Ge along the (a) $\langle 100 \rangle$, (b) $\langle 111 \rangle$ and (c) $\langle 110 \rangle$ directions using continuum theory with optimized values of the elastic constants. The data points represent neutron scattering data (Nilsson and Nelin, 1971).

We have also plotted the dispersion curves of Ge in the $\langle 100 \rangle$, $\langle 111 \rangle$ and $\langle 110 \rangle$ symmetry directions using the elastic constants extracted by Maranganti et al (2007) in figure 3.2. These are compared with neutron scattering data represented by the data points in these curves (Nilsson and Nelin, 1971).

The dispersion curves of Ge plotted using the dispersion relations of section 3.2 and elastic constants extracted directly from neutron scattering data in figure 3.1 give a better fit to neutron scattering dispersion relations for the near zone centre acoustic modes than the ones calculated using elastic constants derived from the shell model. This may be explained by the fact that the lattice dynamics model is simultaneously fitted to experimental data for all the optical and acoustic branches and is therefore in a sense a compromise. It should not therefore be expected to necessarily give the best possible fit to the acoustic branches near the zone centre. Another possible explanation is that the expressions used to evaluate the dynamical matrix are correct up to order k^4 (Maranganti and Sharma, 2007). The parameters of this model, the force constants, can therefore only give a good fit to the dispersion relation data for asymptotically small wave vector values, whereas our parameters have been

chosen to give a good fit to the neutron scattering data over a larger range of k .

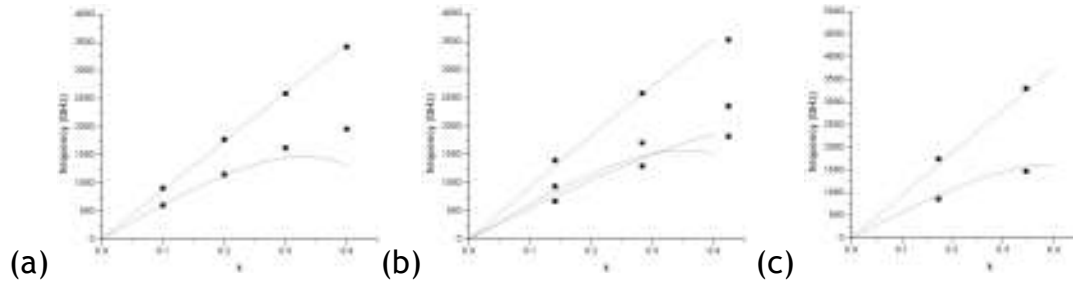


Figure 3.2 Dispersion curves of Ge along the (a) $\langle 100 \rangle$, (b) $\langle 110 \rangle$ and (c) $\langle 111 \rangle$ directions using elastic constants extracted by Maranganti et al (2007). The data points represent neutron scattering data (Nilsson and Nelin, 1971).

3.3.2 Elastic constants, dispersion parameters and dispersion curves of Si along symmetry directions

For Si, we used the same procedures as for Ge to obtain the non-dispersive and dispersive elastic constants. We used a density of $2.33 \times 10^3 \text{ kg m}^{-3}$ and lattice parameter of 5.43\AA was used for calculations on silicon (Kittel, 1956). The dispersive and non-dispersive elastic constants extracted from neutron scattering data of silicon obtained are shown in the left hand column of table 3.2. The non-dispersive elastic constants give an anisotropy factor of 0.638 which is in good agreement with the value of 0.645 obtained from the tabulated values of elastic constants, although as with Ge, the actual values of the elastic constants are larger than the tabulated values.

The dispersive parameters of Si were also recently obtained from atomic displacement correlation functions in an NVT (constant number of particles N , constants volume V and constant temperature T) molecular dynamics ensemble by Maranganti and Sharma, (2007) and are shown in the right hand column of

table 3.2. They used a method based upon calculating the displacements of all atoms in an ensemble for wave vectors along symmetry directions.

Si (<i>neutron scattering</i>)	Si (<i>molecular dynamics</i>)
$C_{11} = 1.7750 \times 10^{11} \text{ (kg m}^{-1} \text{ s}^{-2}\text{)}$	$C_{11} = 1.450 \times 10^{11} \text{ (kg m}^{-1} \text{ s}^{-2}\text{)}$
$C_{12} = 0.745 \times 10^{11} \text{ (kg m}^{-1} \text{ s}^{-2}\text{)}$	$C_{12} = 0.840 \times 10^{11} \text{ (kg m}^{-1} \text{ s}^{-2}\text{)}$
$C_{44} = 0.807 \times 10^{11} \text{ (kg m}^{-1} \text{ s}^{-2}\text{)}$	$C_{44} = 0.700 \times 10^{11} \text{ (kg m}^{-1} \text{ s}^{-2}\text{)}$
$f_1 = -7.515 \times 10^{-10} \text{ (kg m s}^{-2}\text{)}$	$f_1 = -3.700 \times 10^{-10} \text{ (kg m s}^{-2}\text{)}$
$f_2 = -12.500 \times 10^{-10} \text{ (kg m s}^{-2}\text{)}$	$f_2 = -2.700 \times 10^{-10} \text{ (kg m s}^{-2}\text{)}$
$f_3 = 0.126 \times 10^{-10} \text{ (kg m s}^{-2}\text{)}$	$f_3 = 1.900 \times 10^{-10} \text{ (kg m s}^{-2}\text{)}$
$f_4 = -5.243 \times 10^{-10} \text{ (kg m s}^{-2}\text{)}$	$f_4 = -3.400 \times 10^{-10} \text{ (kg m s}^{-2}\text{)}$
$f_5 = -3.775 \times 10^{-10} \text{ (kg m s}^{-2}\text{)}$	$f_5 = -3.200 \times 10^{-10} \text{ (kg m s}^{-2}\text{)}$
$f_6 = 1.250 \times 10^{-10} \text{ (kg m s}^{-2}\text{)}$	$f_6 = 1.000 \times 10^{-10} \text{ (kg m s}^{-2}\text{)}$

Table 3.2. Non-dispersive and dispersive elastic constants of silicon obtained by fitting neutron scattering data to the continuum model versus a molecular dynamics model.

The dispersion curves of silicon plotted using the elastic constants extracted directly from neutron scattering data are shown in figure 3.3. The data points in the dispersion curves represent the experimental neutron scattering data extracted from Dolling (1963), Nilsson and Nelin (1972) for Si. Again the neutron scattering elastic constants give a good fit to the experimental data up to about $k = 0.4$ for all the acoustic branches in the three symmetry directions and they give a particularly accurate fit for the longitudinal modes.

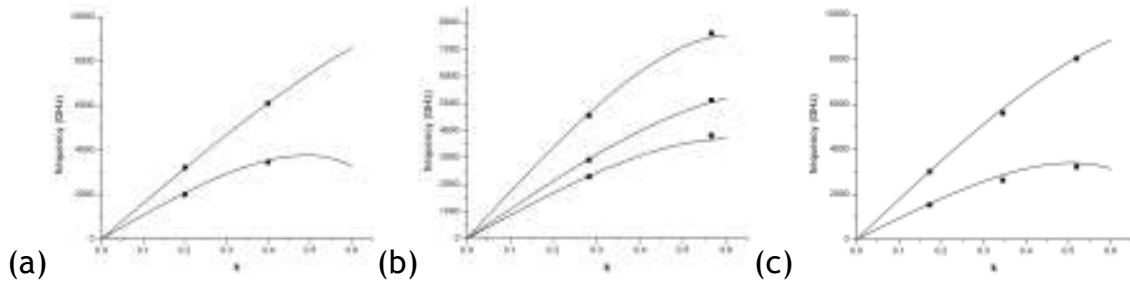


Figure 3.3 Dispersion curves of Si along the (a) $\langle 100 \rangle$, (b) $\langle 110 \rangle$ and (c) $\langle 111 \rangle$ directions using continuum theory with optimized elastic constants. The data points represent neutron scattering data (Dolling, 1963; Nilsson and Nelin, 1972).

We have also plotted dispersion curves of Si, figure 3.4, using non-dispersive and dispersive elastic constants extracted using the molecular dynamics (MD) approach by Maranganti et al (2007). These curves are compared with experimental dispersion relation data from neutron scattering experiments represented by the data points (Dolling, 1963; Nilsson and Nelin, 1972).

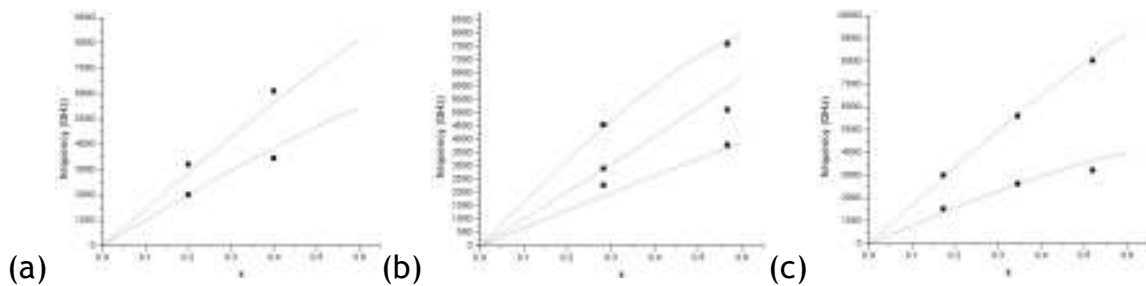


Figure 3.4 Dispersion curves of Si along the (a) $\langle 100 \rangle$, (b) $\langle 110 \rangle$ and (c) $\langle 111 \rangle$ directions using molecular dynamics elastic constants extracted by Maranganti et al (2007). The data points represent neutron scattering data (Dolling, 1963 and Nilsson and Nelin, 1972).

Dispersion curves obtained using MD elastic constants in figure 3.4 are not as consistent with neutron scattering data as the ones obtained using the elastic

constants derived directly from neutron scattering data in figure 3.3. A possible explanation is that the fitting of MD elastic constants is carried out for wave vector values near $k = 0$ (Maranganti, 2007) and as a result one obtains a good fit to experimental data for small wave vector values. At large wave vector values however, a small deviation resulting from the approximations may not give a good fit to the experimental data.

We are only going to use wave vector data up to $k = 0.3$ in our phonon imaging calculations for germanium and silicon. In this region, all the dispersion curves are in very good agreement with experimental dispersion relation data. We note here that for k values up to 0.4, the frequencies of the acoustic mode of Ge extend up to about 3500GHz while for Si they extend a bit beyond 6000GHz, which is almost twice as high. Thus, to observe a similar degree of dispersion, one must expect to go twice as high in frequency for Si as for Ge.

3.4 Determination of elastic constants and dispersion parameters of InSb

For indium antimonide and gallium arsenide, for which the parameter d is not equal to zero and the dispersion relations for the quasi longitudinal and quasi transverse modes in the $\langle 110 \rangle$ direction take on the more complicated form,

$$\rho\omega^2 = \frac{(Q+T+S)}{2} \pm \frac{\left[(Q+T-S)^2 + 8U'^2 \right]^{\frac{1}{2}}}{2}, \quad (3.33)$$

while the dispersion relations for the $\langle 100 \rangle$ and $\langle 111 \rangle$ directions are the same as for Ge and Si, and do not depend on d . An attempt was made to approximate (3.33) by polynomial expressions of the same form as the other dispersion relations through power series expansion of the surd, but this was not successful in fitting the dispersion relations. The reason could be traced to the comparable magnitude of certain terms of different power in the

discriminant. For extracting the parameters f_i and d from neutron scattering data it is convenient to work with polynomial expressions in k and we have obtained these from (3.33) by combining the L and T1 expressions as follows,

$$\frac{\rho\omega_L^2 + \rho\omega_{T1}^2}{k^2} = \frac{1}{k^2}(Q+T+S) = \frac{1}{2}(C_{11} + C_{12} + 4C_{44}) + (g_2 + 6g_3 + 3g_4 - 6f_4 - 12f_6)\frac{k^2}{4}, \quad (3.34)$$

and

$$\left(\frac{\rho\omega_L^2 - \rho\omega_{T1}^2}{k^2}\right)^2 = \frac{1}{k^4}\left\{(Q+T-S)^2 + 8U'^2\right\} \\ = \frac{1}{4}(C_{11} + C_{12})^2 + \left[\frac{1}{4}(C_{11} + C_{12})(2g_1 + g_2 - 9g_4 + 18f_4 - 12f_6) + 9d^2\right]k^2. \quad (3.35)$$

For InSb we have not been able to exploit the dispersion relation for the pure T mode in the $\langle 110 \rangle$ direction since there is no neutron scattering data available for that particular branch for InSb.

For the $\langle 100 \rangle$ direction, equations (3.14) and (3.15) apply while for the $\langle 111 \rangle$ direction; equations (3.19) and (3.21) apply. To obtain the three elastic constants and the seven dispersion constants f_i and d , we have fitted the above mentioned expressions to neutron scattering data reported by Price et al (1971).

We first of all determined the non-dispersive elastic constants of InSb by fitting to the initial slopes of the measured dispersion relations. Our starting values were the tabulated values (Every and McCurdy, 1992) in the Landolt-Börnstein series, $C_{11} = 0.662 \times 10^{11}$, $C_{12} = 0.359 \times 10^{11}$ and $C_{44} = 0.302 \times 10^{11}$, all in units of $\text{kg m}^{-1} \text{s}^{-2}$. We made use of the same optimization technique as used for germanium and silicon in 3.3 and the values we obtained for the elastic constants are tabulated in table 3.3.

Extracting the values of the dispersive elastic constants is an underdetermined problem since these are obtained from the coefficients of k^2 in (3.14), (3.15), (3.19), (3.21), (3.34) and (3.35) and there are only six of these while there are seven dispersion coefficients. We have dealt with this problem as follows using the neutron scattering data of Price et al (1971). Taking the L and T branch data for reduced wave vector values up to 0.4 in the $\langle 100 \rangle$ direction and using (3.14) and (3.15) we have obtained the values of f_1 and f_2 . From data for the $\langle 111 \rangle$ direction we obtain the values of the combinations of the dispersive elastic constants g_3 and g_4 . We consider these values as precisely determined and we now have these expressions for the [111] direction,

$$f_1 + 2f_2 + 6f_3 + 12f_4 + 16f_5 + 24f_6 = 9g_3, \quad (3.36)$$

$$f_1 + 2f_2 + 6f_3 + 12f_4 - 8f_5 - 12f_6 = 9g_4. \quad (3.37)$$

By subtracting (3.36) from (3.37), f_3 and f_4 are eliminated and we can express f_5 in terms of f_6 and the known quantities g_1 , g_2 , g_3 and g_4 . Likewise by adding twice (3.36) to (3.37), f_5 and f_6 are eliminated and we can express f_3 in terms of f_4 and the known quantities g_1 , g_2 , g_3 and g_4 . In this way we obtain,

$$f_5 = \frac{1}{8}(3g_3 - 3g_4 - 12f_6),$$

$$f_3 = \frac{1}{6}(3g_3 + 6g_4 - g_1 - 2g_2 - 12f_4).$$

We now replace f_3 and f_5 in equations (3.34) and (3.35) using the above expressions and substitute the values of the elastic constants f_1 , f_2 , g_3 and g_4 , and from the coefficients of the k^2 terms we obtain from neutron scattering data, we have two relations for the parameters f_4 , f_6 and d^2 . There is thus a line of points in parameter space, all of which yield exactly the

same fit to the six measured dispersion relations. We have chosen to regard d^2 as the free parameter. Its minimum value is zero and we have determined its maximum value to be $5.06 \text{ kg}^2 \text{ s}^{-4}$ beyond which f_i have unphysical complex values. To determine where on this line and for which d^2 in the desired interval the actual parameter set is likely to lie, we have calculated dispersion curves for the direction ($\theta = 32.0$ and $\phi = 47.16$) that lies near the centre of the symmetry irreducible sector bounded by the [001], [110] and [111] directions. A plausible assumption is that these curves should not lie outside the bounds set by the dispersion curves for the symmetry directions. We have gone further and assumed that these curves are as close as possible to being an average of the symmetry direction dispersion curves. In this way we have narrowed down the value of d^2 to $4.0 \text{ kg}^2 \text{ s}^{-4}$.

In our calculation we have used a density of $5.79 \times 10^3 \text{ kg m}^{-3}$ (Wolfe, 1998) and a lattice parameter of 6.48 \AA for InSb. The non-dispersive and dispersive elastic constants of InSb obtained using these procedures are shown in table 3.3. The anisotropy factor obtained from the non-dispersive elastic constants extracted directly from neutron scattering data is 0.512. This is in very good agreement with the value of 0.502 obtained from the tabulated elastic constants.

InSb (Non-dispersive constants)	InSb (Dispersive constants)
$C_{11} = 0.707 \times 10^{11} \text{ (kg m}^{-1} \text{ s}^{-2}\text{)}$	$f_1 = -4.162 \times 10^{-10} \text{ (kg m s}^{-2}\text{)}$
$C_{12} = 0.449 \times 10^{11} \text{ (kg m}^{-1} \text{ s}^{-2}\text{)}$	$f_2 = -6.181 \times 10^{-10} \text{ (kg m s}^{-2}\text{)}$
$C_{44} = 0.252 \times 10^{11} \text{ (kg m}^{-1} \text{ s}^{-2}\text{)}$	$f_3 = -2.103 \times 10^{-10} \text{ (kg m s}^{-2}\text{)}$
	$f_4 = -2.964 \times 10^{-10} \text{ (kg m s}^{-2}\text{)}$
	$f_5 = -2.258 \times 10^{-10} \text{ (kg m s}^{-2}\text{)}$
	$f_6 = 0.924 \times 10^{-10} \text{ (kg m s}^{-2}\text{)}$
	$d = 2.000 \text{ (kg s}^{-2}\text{)}$

Table 3.3. Non-dispersive and dispersive elastic constants of indium antimonide obtained by fitting neutron scattering data to the continuum model.

3.4.1 Dispersion curves of InSb along symmetry and Brillouin zone centre directions

Figure 3.5 shows a comparison between the measured and calculated dispersion curves of indium antimonide along the [100], [111] and [110] symmetry directions and along the direction passing through the centre of the irreducible sector in figure 3.6. The data points in these plots are experimental neutron scattering data from Price et al (1971). The dispersion curves plotted using elastic constants extracted from neutron scattering data are in very good agreement with experimental data along all the symmetry directions. Experimental data for the slow transverse acoustic mode along the [110] direction could not be found.

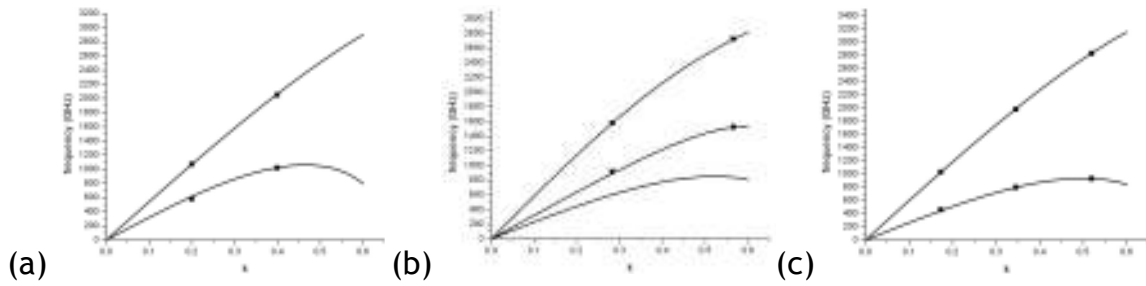


Figure 3.5 Dispersion curves of InSb along the (a) $\langle 100 \rangle$, (b) $\langle 110 \rangle$ and (c) $\langle 111 \rangle$ directions using continuum theory with optimized values of elastic constants. The data points represent neutron scattering data (Price et al, 1971).

For k up to 0.4 the frequencies of the acoustic modes of InSb range up to about 2 THz which is less than that of Ge. We do not therefore expect to have to go as high in frequency for InSb as we do for Ge to observe a similar degree of dispersion.

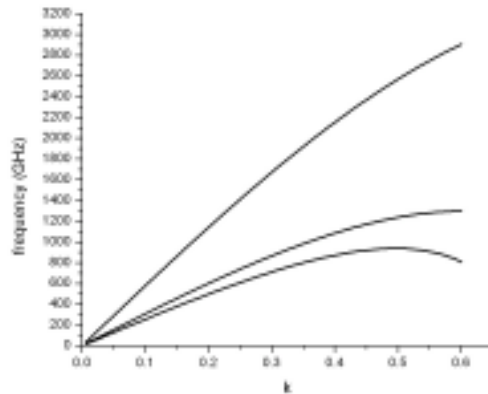


Figure 3.6 Dispersion curves of InSb along the direction through the centre of the irreducible sector.

3.5 Determination of elastic constants and dispersion parameters of GaAs

Determination of the non-dispersive elastic constants and dispersive parameters f_i and d from neutron scattering data for GaAs was carried out in a procedure similar to that of InSb in section 3.4. The non-dispersive elastic constants were determined by fitting to the initial slopes of experimental dispersion relations. We started with tabulated values (Every and McCurdy, 1992) in the Landolt-Börnstein series, $C_{11} = 1.180 \times 10^{11}$, $C_{12} = 0.535 \times 10^{11}$ and $C_{44} = 0.594 \times 10^{11}$, all in units of $\text{kg m}^{-1} \text{s}^{-2}$. The same optimisation technique used for Ge, Si and InSb was used and the elastic constants obtained are tabulated in Table 3.3.

To determine the dispersive elastic constants of GaAs, we used neutron scattering data of Dolling and Waugh, (1965). We made use of data for reduced wave vector values up to 0.4 along the $\langle 100 \rangle$ directions and used (3.14) and (3.15) to obtain values of f_1 and f_2 . Data for the $\langle 111 \rangle$ and $\langle 110 \rangle$ directions was used to determine the values of the combinations of the dispersive elastic constants g_3 , g_4 and g_7 . These values are considered as precisely determined and we now have expressions (3.36) and (3.37) for the [111] direction and for the ST mode along the [110] direction we have,

$$f_1 + f_2 + 6f_4 - 8f_5 = 4g_7. \quad (3.38)$$

Using these expressions we can express f_3 , f_4 and f_6 in terms of f_5 and the known quantities g_1 , g_2 , g_3 , g_4 and g_7 in following way,

$$f_3 = \frac{1}{18}(3g_1 + g_3 + 2g_4 - 6g_7 - 48f_5), \quad (3.39)$$

$$f_4 = \frac{1}{6}(g_7 - g_1 - g_2 + 8f_5), \quad (3.40)$$

$$f_6 = \frac{1}{36}(g_3 - g_4 - 24f_5). \quad (3.41)$$

We then substitute for f_3 , f_4 and f_6 in equations (3.34) and (3.35) using the above expressions and obtain,

$$\frac{\rho\omega_L^2 + \rho\omega_{T1}^2}{k^2} = \frac{1}{k^2}(Q + T + S) = \frac{1}{2}(C_{11} + C_{12} + 4C_{44}) + (g_1 + 2g_2 + 3g_3 + 6g_4 - 4g_7) \frac{k^2}{4}, \quad (3.42)$$

and

$$\begin{aligned} \left(\frac{\rho\omega_L^2 - \rho\omega_{T1}^2}{k^2} \right)^2 &= \frac{1}{k^4} \{ (Q + T - S)^2 + 8U'^2 \} \\ &= \frac{1}{4}(C_{11} + C_{12})^2 + \left[\frac{1}{4}(C_{11} + C_{12})(12g_7 - g_1 - 2g_2 - 3g_3 - 6g_4 + 32f_5) + 9d^2 \right] k^2. \end{aligned} \quad (3.43)$$

Equation (3.42) does not contain any of the two undetermined parameters, f_5 or d^2 , and so we have a singular valued problem. This is solved by varying the values of the two undetermined parameters f_5 and d^2 searching for the best fit to experimental dispersion relation data. At each point, we calculated dispersion curves for the direction that lies near the centre of the symmetry irreducible sector as done for InSb to verify that they were within acceptable bounds. The best fit to neutron scattering data was found for the values $f_5 = -2.80 \times 10^{-10} \text{ kg m s}^{-2}$ and $d^2 = 6.25 \text{ kg s}^{-2}$.

In our calculations, a density of $5.34 \times 10^3 \text{ kg m}^{-3}$ (Wolfe, 1998) and a lattice parameter of 5.65 \AA (Ashcroft, 1976) has been used. The non-dispersive and dispersive elastic constants of GaAs obtained using these procedures are shown in table 3.4. The anisotropy factor of 0.538 obtained from the non-dispersive elastic constants extracted directly from neutron scattering data is in good

agreement with the value of 0.543 obtained from the tabulated elastic constants.

For GaAs, we also used the non-dispersive and dispersive elastic constants published by DiVincenzo in 1986. He obtained these through the intermediary of the shell lattice dynamics using the same procedure as already outlined for Ge by Maranganti et al (2007). DiVincenzo's non-dispersive and dispersive elastic constants are also tabulated in table 3.4.

GaAs (<i>neutron scattering</i>)	GaAs (<i>shell model</i>)
$C_{11} = 1.200 \times 10^{11} \text{ (kg m}^{-1} \text{ s}^{-2}\text{)}$	$C_{11} = 1.200 \times 10^{11} \text{ (kg m}^{-1} \text{ s}^{-2}\text{)}$
$C_{12} = 0.576 \times 10^{11} \text{ (kg m}^{-1} \text{ s}^{-2}\text{)}$	$C_{12} = 0.540 \times 10^{11} \text{ (kg m}^{-1} \text{ s}^{-2}\text{)}$
$C_{44} = 0.580 \times 10^{11} \text{ (kg m}^{-1} \text{ s}^{-2}\text{)}$	$C_{44} = 0.600 \times 10^{11} \text{ (kg m}^{-1} \text{ s}^{-2}\text{)}$
$f_1 = -4.000 \times 10^{-10} \text{ (kg m s}^{-2}\text{)}$	$f_1 = -2.600 \times 10^{-10} \text{ (kg m s}^{-2}\text{)}$
$f_2 = -9.000 \times 10^{-10} \text{ (kg m s}^{-2}\text{)}$	$f_2 = -20.40 \times 10^{-10} \text{ (kg m s}^{-2}\text{)}$
$f_3 = 0.933 \times 10^{-10} \text{ (kg m s}^{-2}\text{)}$	$f_3 = -4.800 \times 10^{-10} \text{ (kg m s}^{-2}\text{)}$
$f_4 = -3.567 \times 10^{-10} \text{ (kg m s}^{-2}\text{)}$	$f_4 = -2.400 \times 10^{-10} \text{ (kg m s}^{-2}\text{)}$
$f_5 = -2.800 \times 10^{-10} \text{ (kg m s}^{-2}\text{)}$	$f_5 = -1.600 \times 10^{-10} \text{ (kg m s}^{-2}\text{)}$
$f_6 = 1.997 \times 10^{-10} \text{ (kg m s}^{-2}\text{)}$	$f_6 = 1.900 \times 10^{-10} \text{ (kg m s}^{-2}\text{)}$
$d = 2.500 \text{ (kg s}^{-2}\text{)}$	$d = -1.8 \text{ (kg s}^{-2}\text{)}$

Table 3.4. Non-dispersive and dispersive elastic constants of Gallium Arsenide obtained by fitting neutron scattering data the continuum model versus the shell model.

3.5.1 Dispersion curves of GaAs along symmetry and Brillouin zone centre directions

A comparison between the measured and calculated dispersion curves of gallium arsenide along the $[100]$, $[111]$ and $[110]$ symmetry directions and along the direction passing through the centre of the irreducible sector are shown in figure 3.7 and 3.8. The data points in these plots are experimental neutron scattering data from Dolling et al (1963). The dispersion curves plotted using elastic constants derived directly from neutron scattering data are in very good agreement with experimental data along all the symmetry directions. The frequencies of the acoustic modes of GaAs extend up to about 3.7 THz which is a bit beyond the 3.5 THz for Ge. We therefore expect a similar degree of dispersion between GaAs and Ge.

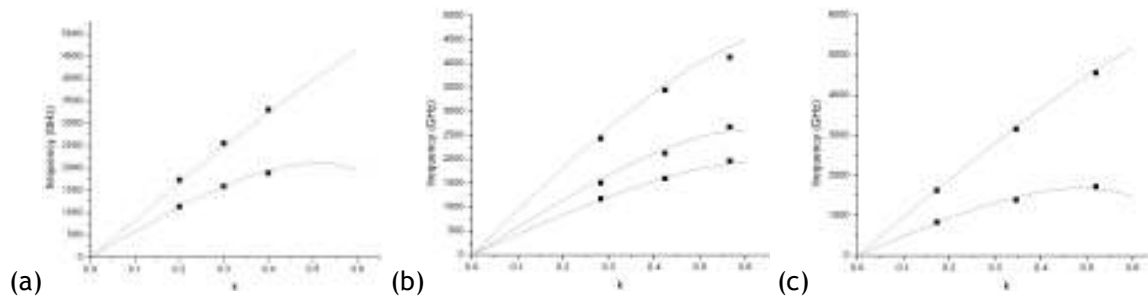


Figure 3.7 Dispersion curves of GaAs along the (a) $\langle 100 \rangle$, (b) $\langle 110 \rangle$ and (c) $\langle 111 \rangle$ directions using continuum theory with optimised values of the elastic constants. The data points represent neutron scattering data (Dolling et al, 1963).

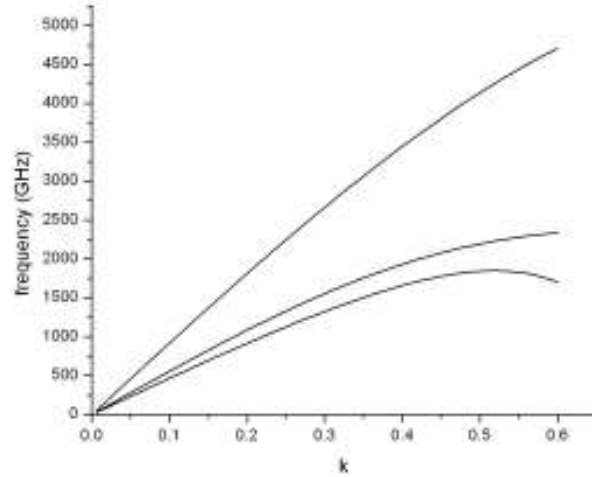


Figure 3.8 Dispersion curves of GaAs along the direction through the centre of the irreducible sector.

We have used DiVincenzo’s shell model elastic constants to plot dispersion curves in figure 3.9 and compare them to neutron scattering data. The experimental data points in figure 3.9 have been obtained from Dolling and Waugh (1963). There is good agreement for k , up to 0.3 and then the transverse modes gradually drift away from the experimental data.

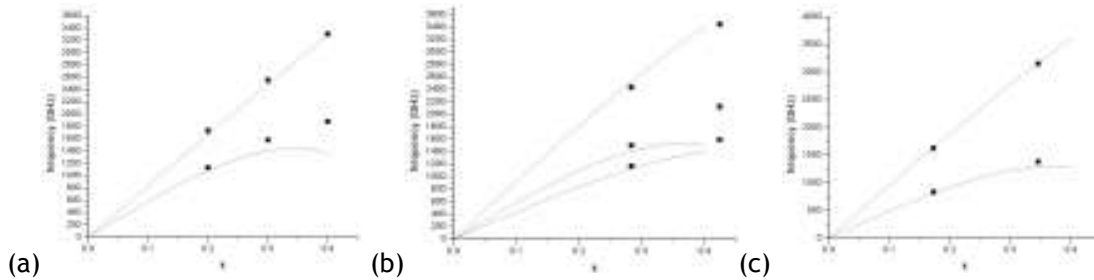


Figure 3.9 Dispersion curves of GaAs along the (a) $\langle 100 \rangle$, (b) $\langle 110 \rangle$ and (c) $\langle 111 \rangle$ directions using the parameters of DiVincenzo (1986). The data points represent neutron scattering data (Dolling et al, 1963).

The dispersion curves of GaAs obtained using elastic constants extracted directly from neutron scattering data in figure 3.7 are in good agreement with

neutron scattering data up to frequencies corresponding to about $k = 0.5$. The dispersion curves obtained using the DiVincenzo elastic constants in figure 3.9 agree with experimental data for wave vector values up to $k = 0.3$. The differences in agreement with experimental data between the two sets of elastic constants may be explained by reasons pointed out earlier in a similar discussion for Ge.

3.6 Dispersive phonon imaging calculations

We calculate the dispersive phonon images of cubic crystals using a program written in the FORTRAN programming language. In this program, we first generate a random distribution of wave vectors in three dimensional \mathbf{k} - space out to a radial distance of $k = 0.3$ in reduced wave vector units.

For each wave vector generated in the program, we find the roots of equation (3.12) using a subroutine zroots which in turn uses the subroutine Laguer to polish the roots. A detailed review of these subroutines can be found in the book Numerical Recipes in FORTRAN by William Press et al, (1986). At this point in our program we can plot dispersion curves of the crystal along any direction in the crystal. As a check for the consistency of our calculations, plots of the dispersion curves in the symmetry directions were compared to the previously calculated ones. These curves were found to be exactly the same as the ones in section 3.5 plotted using the symmetry direction dispersion relations and are therefore also consistent with experiment.

We then calculate the corresponding group velocity vectors by finding the derivative of equation (3.12) with respect to wave vector thus,

$$\mathbf{V}_g = \nabla_{\mathbf{k}} \omega(\mathbf{k}) = \frac{\frac{\partial e(\mathbf{k})}{\partial \mathbf{k}} + \lambda \frac{\partial d(\mathbf{k})}{\partial \mathbf{k}} + \lambda^2 \frac{\partial c(\mathbf{k})}{\partial \mathbf{k}}}{3\lambda^2 - 2c(\mathbf{k})\lambda - d(\mathbf{k})} \times \frac{1}{2\rho\omega} \quad (3.44)$$

For each group velocity vector, we find its point of intersection with the (100), (110) or (111) imaging planes. The imaging planes are divided into 500 by 500 bins and the number of group velocity vectors falling into each bin is stored as a matrix. This matrix is then plotted on a grey scale image with high phonon intensity represented by bright areas whilst dark regions represent low phonon intensity. Using our program, we can simulate the phonon images for a chosen range of frequencies, wave vectors or we can simulate velocity-gated images. As an example, the differences between the phonon images calculated for the 0.0-0.3 and 0.5-0.6 THz frequency ranges in the (110) observation plane for germanium can be seen in figure 3.10. The diamond structure around the $\langle 100 \rangle$ directions for the higher frequency range has become rounded and the inner box has become smaller. The FT caustics connecting the $\langle 100 \rangle$ directions have become more widely separated at the higher frequencies. Changes in the regions surrounding the $\langle 111 \rangle$ directions are less pronounced, and so, in this thesis we do not place much emphasis on the dispersive images projected in the (111) observation plane.

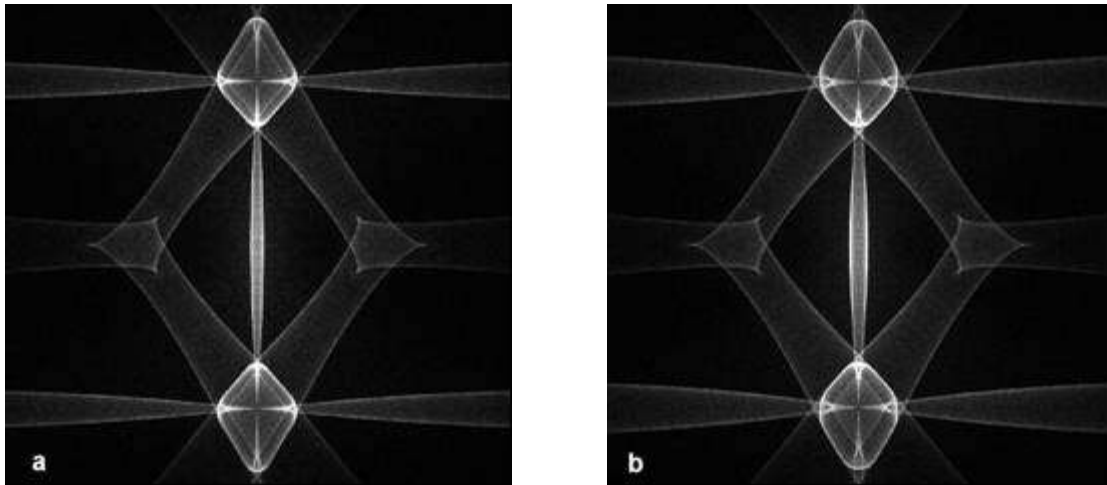


Figure 3.10. Calculated dispersive phonon images of Ge in the (110) observation plane: (a) 0.0-0.3THz (b) 0.5-0.6THz.

Chapter 4

Phonon Focusing Patterns of Ge and Si

There have been a number of theoretical and experimental studies on the phonon focusing patterns of germanium and silicon. Notable are the investigations carried out by Northrop et al (1980), Northrop (1982), Metzger et al (1988), Tamura et al (1991) and Tamura (1982).

Germanium and silicon which are of O_h symmetry have a centre of inversion and the acoustic gyrotropic tensor is zero in such crystals (Every, 1987). These crystals do not therefore, exhibit first order spatial dispersion in their dynamical behavior (Portugal and Burstein, 1968) and no acoustical activity. There is however, second order dispersion, and it is characterized by the f tensor which has six independent components for O_h symmetry.

In the first section of this chapter, the calculated phonon images of Ge are compared with corresponding experimental images. This is then followed by a section on the frequency dependence of the dispersive phonon images of germanium for higher frequency phonons. Then the measured focusing patterns of silicon are compared with continuum elasticity theory simulations. The frequency dependence of dispersive phonon images of silicon is then discussed in the last section of this chapter.

4.1 Comparison of calculated images with those measured in Ge

Low frequency phonon imaging is fully accounted for by classical continuum elasticity theory. Figure 4.1a shows a phonon image of germanium in the (110) observation plane that was measured with a bolometric detector. A

corresponding image, figure 4.1b, was calculated selecting phonons with frequencies ranging from 0.0THz to 0.3THz for which there is negligible dispersion. Phonon focusing structures labeled ST and FT are due to slow transverse and fast transverse phonons respectively. The variation in intensity in these phonon images is mainly due to phonon focusing and the sharp lines are caustics where the focusing is infinite. As pointed out earlier, these are associated with lines on the slowness surface where the Gaussian curvature is zero.

The longitudinal sheet of the slowness surface is separated from the ST and FT slowness sheets and is entirely convex without any parabolic lines. The corresponding wave surface of the L mode does not have any folds and is also entirely convex which means that it does not produce any caustics in the phonon image (Every, 1981). We do not therefore include the longitudinal mode in our calculated phonon images in chapters 4 and 5.

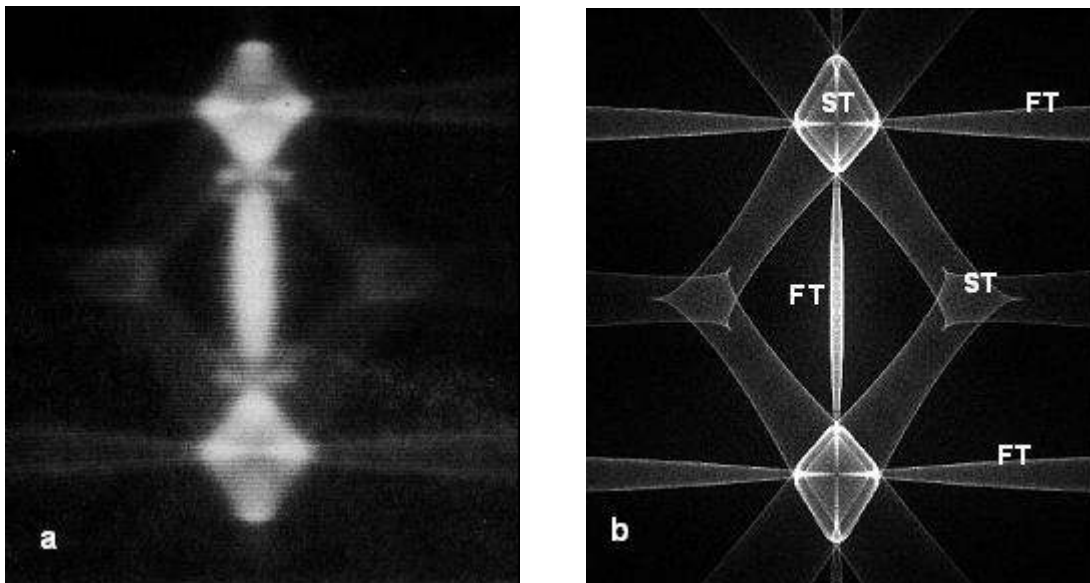


Figure 4.1. Phonon images of Ge in the (110) observation plane: (a) measured image using a bolometric detector by Dietsche et al, (1981), (b) calculated phonon image for essentially non-dispersive phonons in the 0.0 THz to 0.3THz frequency range.

Figure 4.2a shows an experimental image of Ge for the same geometry obtained with a tunnel junction detector sensitive to frequencies above 0.7THz. There are changes in the focusing pattern due to phonon dispersion. The diamond shaped structures centered around the $\langle 100 \rangle$ directions near top and bottom centre have become rounded. The curved horizontal and vertical caustics due to fast transverse caustics have become more widely separated. The three-fold symmetric ST structure around the $\langle 111 \rangle$ directions is absent from the measured image at this frequency.

A calculated phonon image of Ge for the 0.7 to 1.0 THz frequency range in the (110) plane is shown in figure 4.2b. The distance between the FT caustics in the calculated image has increased in conformity with the experimental image. Compared with the non-dispersive phonon image in figure 4.1b, the outer diamond has become rounded and the inner structure has become much smaller at the higher frequencies. The three fold symmetric ST structure around the $\langle 111 \rangle$ directions is conspicuously present in this image.

Another image was calculated for frequencies around 0.85THz and selecting phonons with wave vector k up to 0.15 rather than 0.3, figure 4.2c. This wave vector selection results in the exclusion of phonons with smaller wavelengths which are more susceptible to scattering, and this has the greatest effect on phonons near the slow $\langle 111 \rangle$ directions where the three fold structures are now totally absent. This may explain the absence of the ST phonon focusing structures around the $\langle 111 \rangle$ directions in the measured image of Dietsche et al (1981).

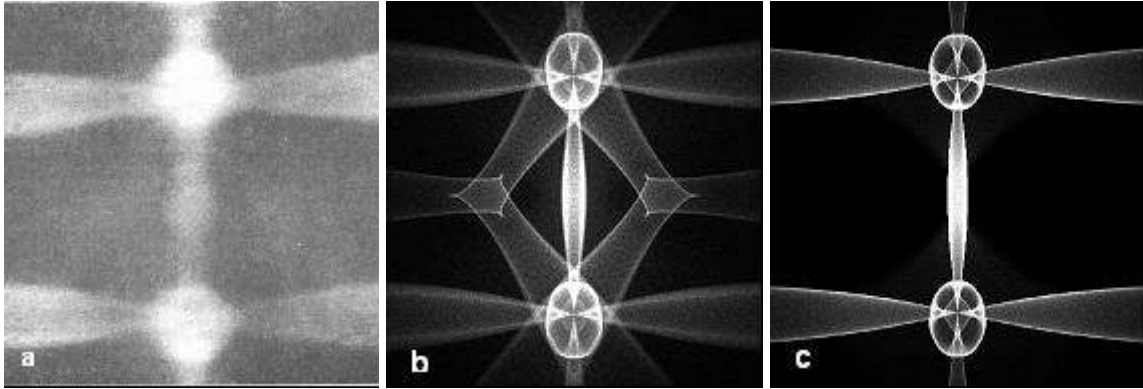


Figure 4.2. Phonon images of Ge in the (110) observation plane, (a) measured using a detector with 0.7THz onset frequency by Dietsche et al, (1981). Calculated images: (b) selecting wave vector k up to 0.3 for phonons with frequencies between 0.7THz and 1.0 THz, (c) selecting wave vector k up to 0.15 for phonons with frequencies near 0.85THz.

The experimental (100) observation plane phonon image of Ge in figure 4.3a was measured by Metzger and Huebener (1988) using a bolometric detector. The points A to F are a means of quantifying the geometric pattern of the focusing image of the ST phonons for comparison with calculated images. Metzger et al (1988) compared this image with classical continuum model simulations and suggested discrepancies between calculated and measured images were due to the fact that the phonons contributing to the image were in the frequency range 0.3-0.4THz, and therefore slightly dispersive. Investigations by Tamura (1982, 1983, and 1985) based on lattice dynamics models have shown that dispersive effects are already quite significant in the focusing patterns of Ge at 0.3THz. We have calculated the focusing pattern of germanium in the (100) observation plane for phonons in the same frequency range 0.3-0.4THz, and the results are shown in figure 4.3b. There is qualitatively excellent agreement between the measured image and calculations using elastic constants derived from neutron scattering data.

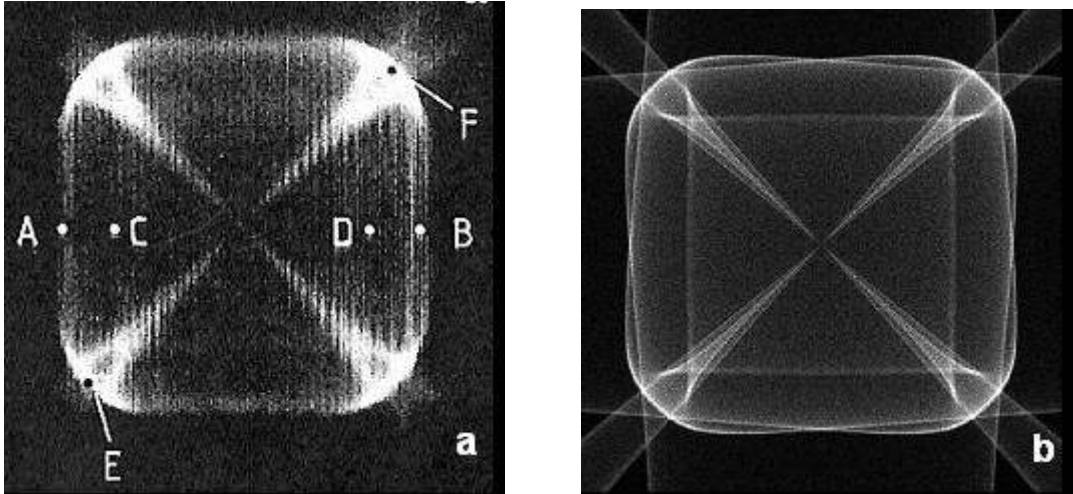


Figure 4.3. Phonon images of Ge in the (100) observation plane for the frequency range: $0.3 \leq f \leq 0.4$ THz. (a) measured image by Metzger and Huebener (1988). (b) Calculated image.

Metzger and Huebener (1988) have used the points marked in the experimental image to define the distance ratios $u = CD/AB$ and $v = EF/AB$. The experimental image gives $u = 0.67$ and we obtain $u = 0.69$ for our continuum model calculation shown in figure 4.3b. The ratio v in the experimental image is 1.22 and 1.19 for our calculated image. Metzger et al attempted to account for their images using “effective” elastic constant ratios, $a = C_{11}/C_{44}$ and $b = C_{12}/C_{44}$. The best agreement between measurement and simulation was found for $a = 2.11$ and $b = 0.91$. These may be compared with our values $a = 1.99$ and $b = 0.80$ used in conjunction with the dispersive elastic constants tabulated in chapter 3.

4.1.1 Comparison of phonon images calculated using shell model derived elastic constants with measured images in Ge

We now compare the phonon images obtained using elastic constants derived from the shell model by Maranganti and Sharma, (2007) with observed phonon

images. Figure 4.4 and 4.5 shows images in the (110) and (100) observation planes.

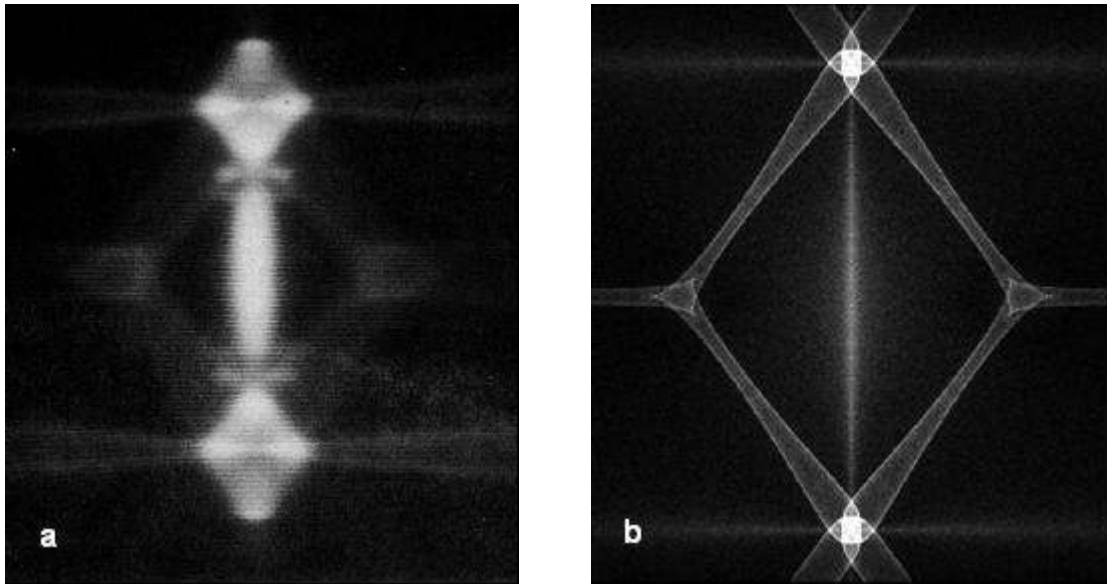


Figure 4.4. Phonon images of Ge in the (110) observation plane: (a) measured image using a bolometric detector by Dietsche et al, (1981), (b) calculated phonon image for essentially non-dispersive phonons in the 0.0 THz to 0.3THz frequency range using shell model elastic constants (Maranganti et al, 2007).

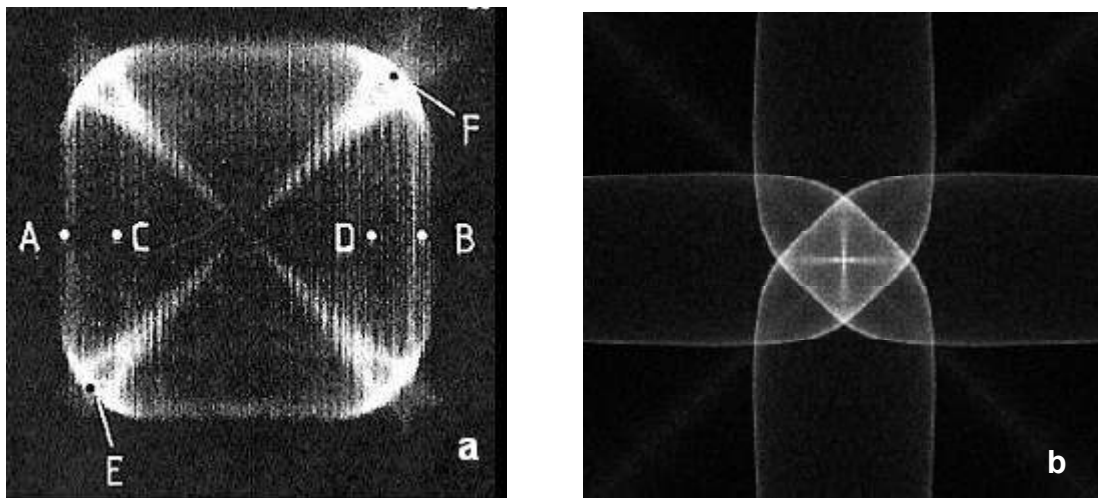


Figure 4.5. Phonon images of Ge in the (100) observation plane for the frequency range: $0.3 \leq f \leq 0.4$ THz. (a) measured image by Metzger and Huebener (1988). (b) Calculated phonon image using shell model elastic constants (Maranganti et al, 2007).

For the non-dispersive experimental image in the (110) plane has a diamond shaped structure around the $\langle 100 \rangle$ directions whilst we obtain a rounded structure in the corresponding calculated image. This is also observed in figure 4.5 for the (100) observation plane. The separation of the FT caustics is larger in the observed image than in the calculated image. Thus, phonon images of Ge obtained using elastic constants extracted directly from neutron scattering data gives much better agreement with measurement as compared with ones derived from the shell model elastic constants. This is expected since better agreement with neutron scattering dispersion relation data is obtained with elastic constants extracted directly from the neutron scattering data.

4.2 Further frequency dependent Ge dispersive phonon images

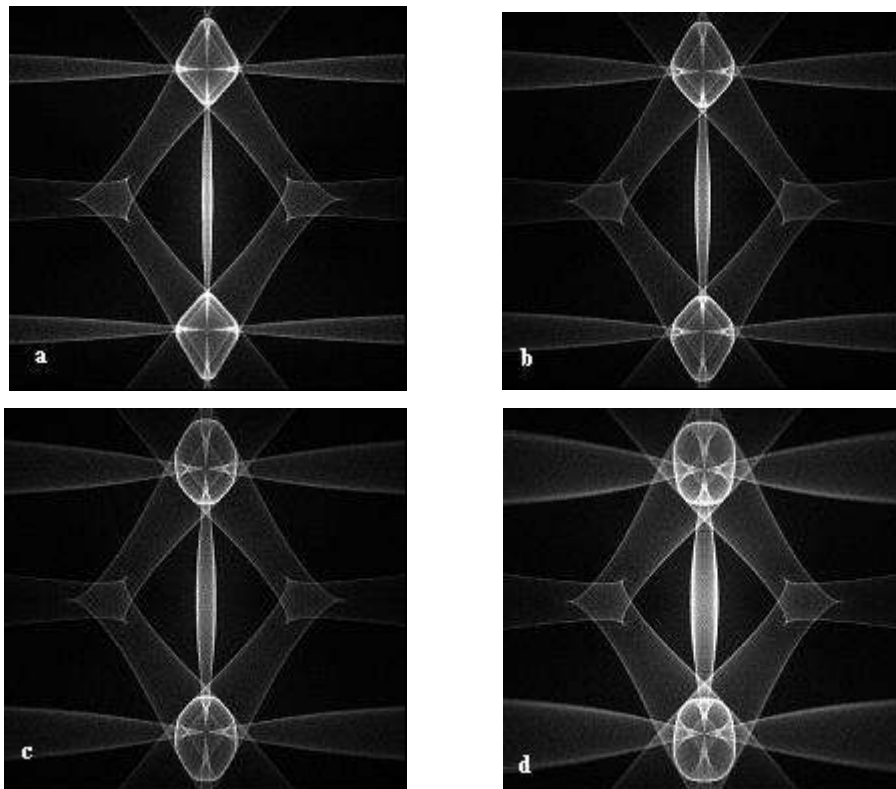


Figure 4.6. Calculated dispersive phonon images of germanium in the (110) imaging plane for the frequency ranges: (a) 0.0 - 0.3 THz (b) 0.5 - 0.6 THz (c) 0.7 - 0.8 THz (d) 0.9 - 1.0 THz.

The calculated phonon images in figure 4.6 display the changes in the phonon focusing pattern of Ge as the frequency increases. They were calculated using non-dispersive and dispersive elastic constants extracted directly from neutron scattering data. The diamond shaped box structures due to ST phonons around the $\langle 100 \rangle$ directions become more rounded and the separation of the FT caustics increases.

The angle subtended by the FT ridge, θ_{FT} , at the centre of the image has been measured and is shown as a function of frequency in figure 4.7. The data points are the opening angles of the FT caustics for each frequency in the calculated images and they have been fitted to a polynomial represented by the solid line. This angle increases from 4.7° at 0.3THz to 11.7° at 1.0THz which is an increase by a factor of 2.49.

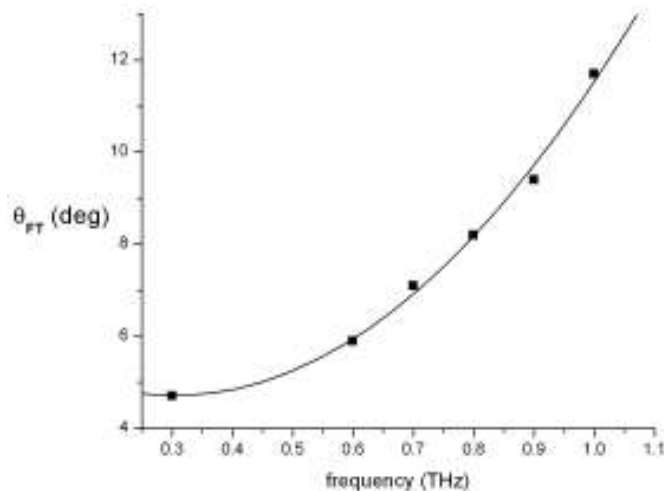


Figure 4.7. The angle between FT caustics, θ_{FT} , as a function of phonon frequency for Ge.

Simulations of the dispersive phonon images in the (100) observation plane of germanium are shown in figure 4.8. They were also calculated using elastic constants extracted directly from neutron scattering data. These images are

rotated by 45° with respect to the images in figure 4.3. For the ST box structure around the $\langle 100 \rangle$ direction, the outer box becomes more rounded whilst the inner box becomes smaller as frequency is increased. The FT caustics become broader at higher frequencies for a given frequency spread and their opening angle becomes much larger. Thus, for the frequency range we have investigated, we do not observe new structures in the focusing pattern of Ge but the existing structures do become gradually modified.

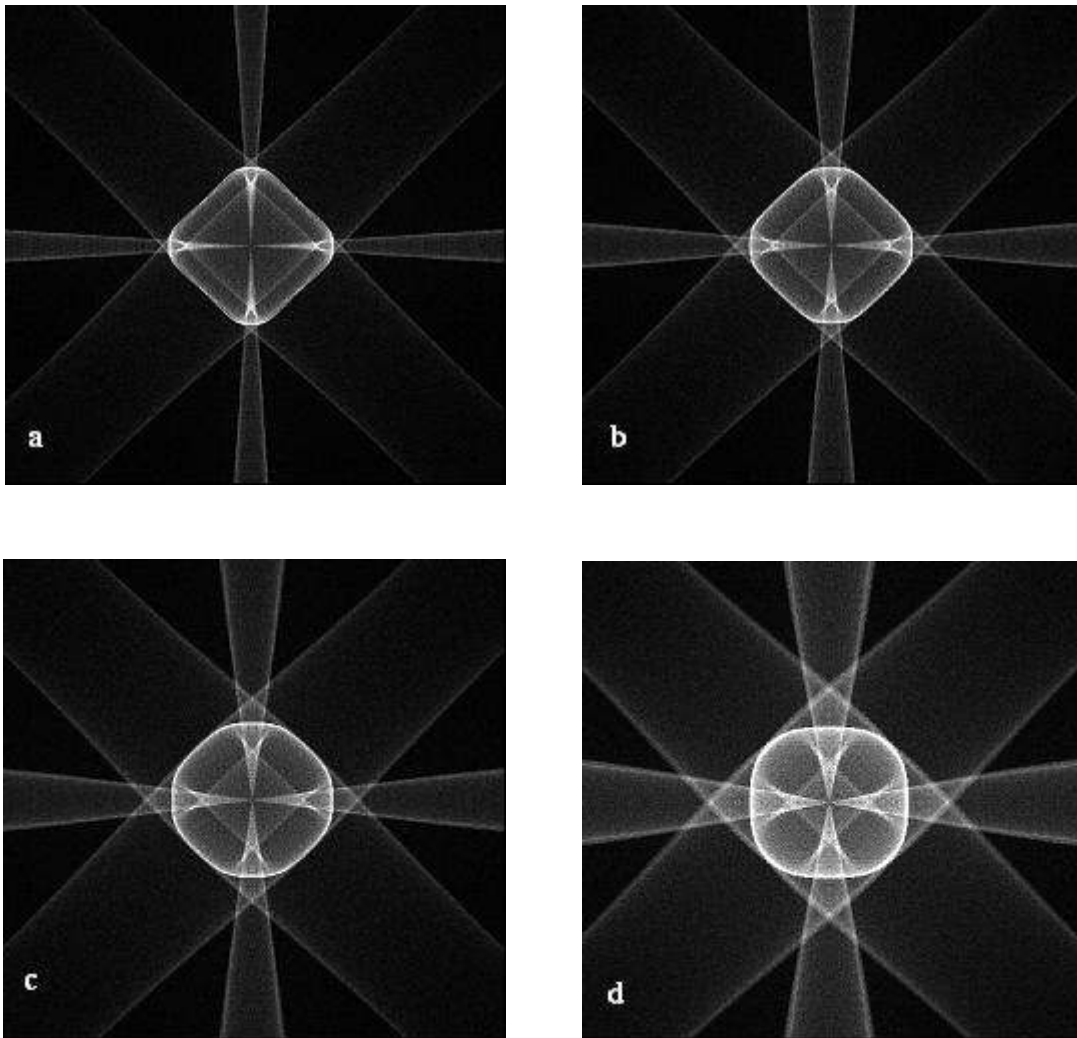


Figure 4.8. Calculated dispersive phonon images of germanium in the (100) imaging plane: (a) 0.0 - 0.3 THz (b) 0.5 - 0.6 THz (c) 0.7 - 0.8 THz (d) 0.9 - 1.0 THz.

The ratio u defined in section 4.1 was measured as a function of frequency for the calculated images in the (100) observation plane. The results are shown in figure 4.9 as the data points which have been fitted to a polynomial represented by the solid line. There is a marked decrease in the ratio u which is 0.68 at 0.3THz and decreases by almost a half to 0.33 at 1.0THz.

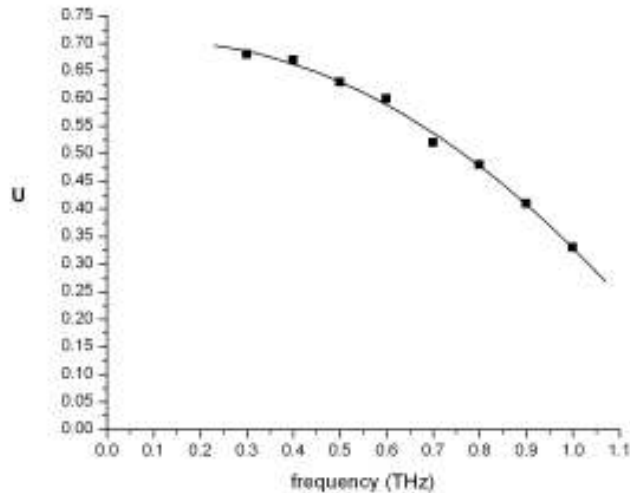


Figure 4.9. The ratio u as a function of phonon frequency.

4.3 Comparison of calculated images with measurements for Si

A comparison between an experimental image obtained with a silicon crystal and a calculation using elastic constants derived directly from neutron scattering data is shown in figure 4.10. These images are in the (100) observation plane of the crystal with the [100] direction at the centre of the image. The measured phonon image, figure 4.10a, was obtained with the use of a tunnel junction detector with an onset frequency of 0.44THz (Tamura et al, 1991). A frequency range of 0.44 to 0.54THz was used in the calculation of the phonon image in figure 4.10b. The non-dispersive and dispersive elastic constants obtained directly from neutron scattering data were used to calculate this image. The experimental image has been well reproduced by the calculated image. The inner box structure in the calculated image is just about the same size as the one in the experimental image.

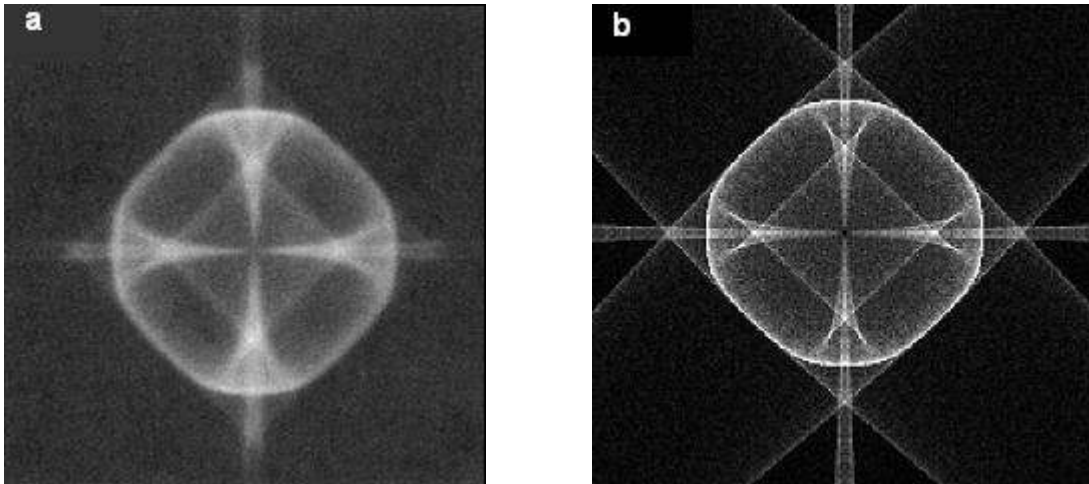


Figure 4.10. Phonon images of Si in the (100) observation plane (a) measured image by Tamura, Shields and Wolfe (1991) using a PbTI tunnel junction detector with an onset frequency of 0.44THz. (b) Calculated image for the frequency range: $0.44 \leq f \leq 0.54$ THz.

Figure 4.11 shows phonon images for Si for the same geometry as in figure 4.10, but for higher frequencies. Figure 4.11a is an image measured by Tamura et al, (1991) using a tunnel junction detector with an onset frequency of 0.7THz. The effects of dispersion at these frequencies are less than for Ge, because the Si vibrational spectrum is scaled up by about a factor of 2 compared to that of Ge. Nevertheless there are noticeable changes to the image above 0.7THz. The outer box structure is slightly more rounded and the inner box slightly smaller. These effects are reproduced in figure 4.11b, which is a calculated image for the frequency range $0.7 \leq f \leq 0.9$ THz.

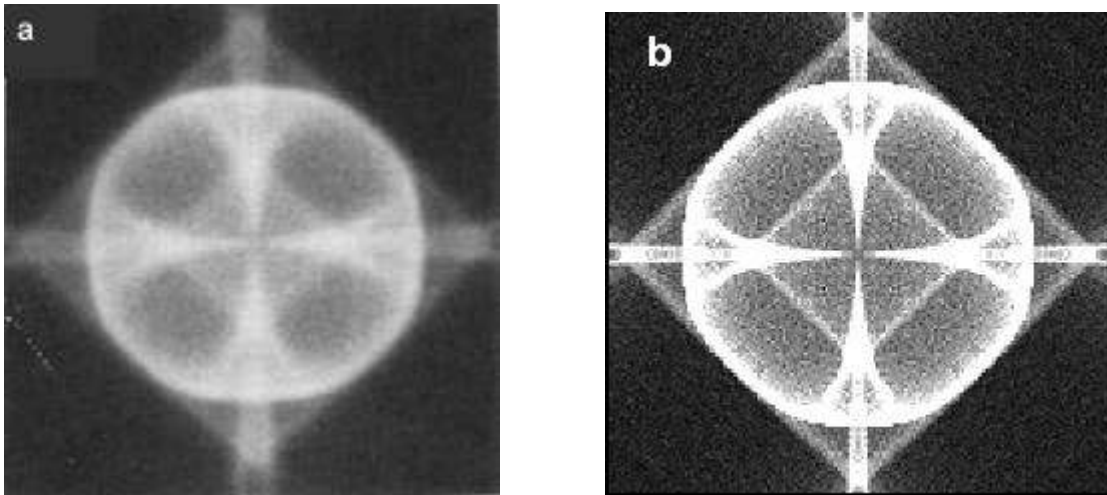


Figure 4.11. Phonon images of Si in the (100) observation plane: (a) measured using a detector with onset frequency 0.7THz by Tamura, Shields and Wolfe (1991), (b) Calculated image for the frequency range: $0.7 \leq f \leq 0.9$ THz.

A phonon image measured in the (110) observation plane using a tunnel junction detector with an onset frequency of 0.82 THz (Shields et al, 1991) is shown in figure 4.12a. A corresponding calculation using non-dispersive and dispersive elastic constants derived directly from neutron scattering data whilst selecting phonons with frequencies between 0.8THz and 0.9THz is shown in figure 4.12b. There is qualitatively good agreement between the experimental image and the calculated image. The ST box structures centered on the $\langle 100 \rangle$ directions are rounded. The separation between the FT caustics connecting the $\langle 100 \rangle$ directions is however somewhat larger in the experimental image than in the calculated image.

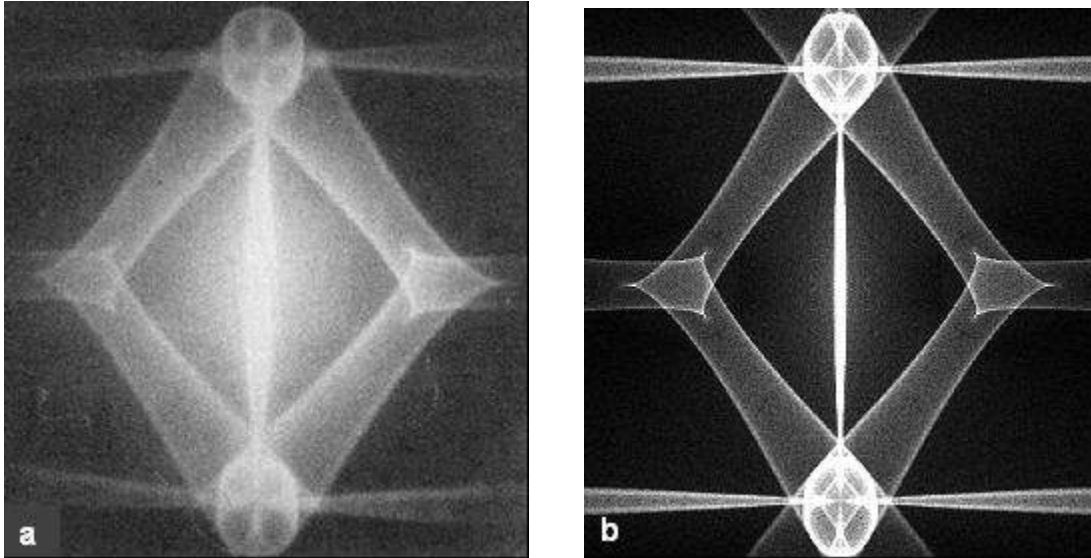


Figure 4.12. Phonon images of Si in the (110) observation plane: (a) measured using a detector with onset frequency 0.82THz by Shields et al (1991), (b) Calculated image for the frequency range: $0.82 \leq f \leq 1.02$ THz.

4.3.1 Comparison of images calculated using MD derived elastic constants with measurements for Si

Phonon images calculated using MD derived elastic constants in the (100) observation plane are compared with experimental phonon images in figures 4.13 and 4.14. The box structure in the image obtained using a detector with an onset frequency of 0.44THz is rounded whilst the corresponding calculation has the box structure. The same observation is made in figure 4.14 which corresponds to images at higher phonon frequencies. The separation of the FT caustics is also much wider in the calculated images than in the experimental images.

The observed phonon images of Si are not well reproduced by calculations using MD elastic constants. We obtain much better agreement with experiment using elastic constants extracted directly from neutron scattering data. This may be

explained by the fact that a better fit to neutron scattering data was obtained using these elastic constants. The non-dispersive elastic constants obtained from MD elastic constants give an anisotropy factor of 0.436 whilst with the elastic constants extracted directly from neutron scattering data we obtain 0.638. This accounts for the big difference in the phonon focusing patterns obtained using the different sets of elastic constants.

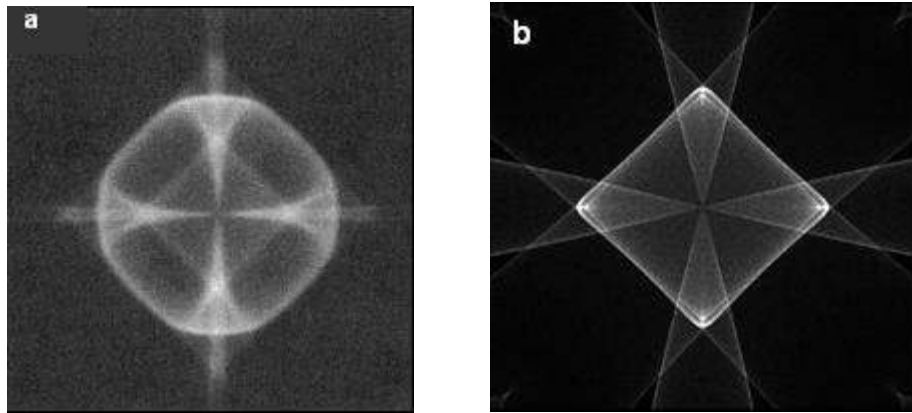


Figure 4.13. Phonon images of Si in the (100) observation plane (a) measured image by Tamura, Shields and Wolfe (1991) using a PbTI tunnel junction detector with an onset frequency of 0.44THz. (b) Calculated image for the frequency range: $0.44 \leq f \leq 0.54$ THz using MD derived elastic constants extracted by Maranganti et al (2007).

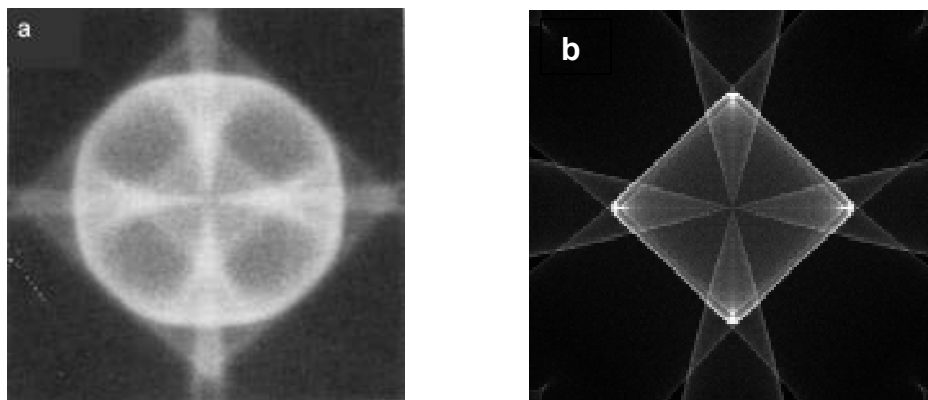


Figure 4.14. Phonon images of Si in the (100) observation plane: (a) measured using a detector with onset frequency 0.7THz by Tamura, Shields and Wolfe (1991), (b) Calculated phonon image for the frequency range: $0.7 \leq f \leq 0.9$ THz using MD derived elastic constants extracted by Maranganti et al (2007).

4.4 Further frequency dependent dispersive phonon images of Si

Silicon does not display a lot of dispersion in its phonon images for frequencies in the range of 0.0-1.0THz, see figure 4.11. This is expected because the vibrational frequencies of Si are about a factor of 1.8 higher than those of Ge at comparable points in the Brillouin zone. We have therefore calculated the phonon images of silicon for frequencies of up to 2.0THz using elastic constants extracted directly from neutron scattering data. The simulated dispersive phonon images of silicon in the (110) observation plane for different frequencies are shown in figure 4.11.

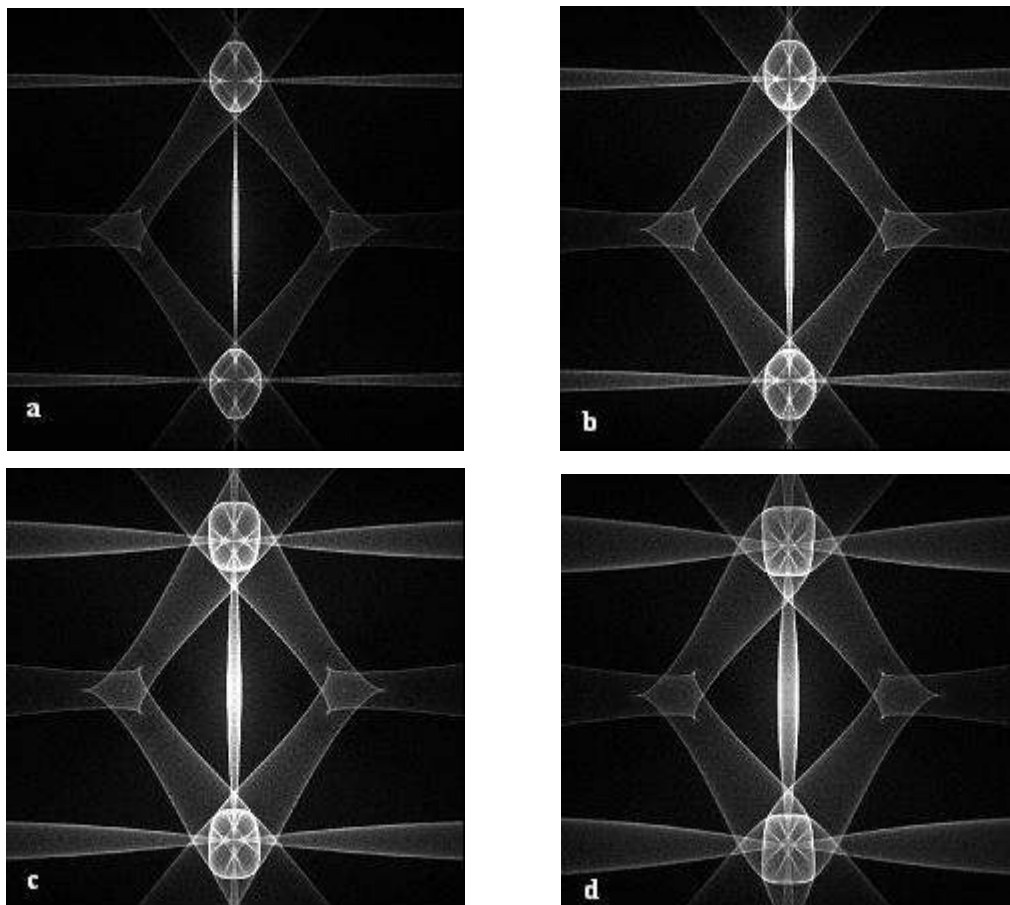


Figure 4.11. Calculated dispersive phonon images of silicon in the (110) imaging plane: (a) 0.0 - 0.3 THz (b) 0.9 - 1.0 THz (c) 1.5 - 1.6 THz (d) 1.9 - 2.0 THz.

The evolution of the focusing patterns of silicon in the (100) observation plane are shown in figure 4.12. It is again noted that for the frequency range we have examined we have not observed any new phonon focusing structures of Si at the higher frequencies; the existing focusing patterns simply become modified. The box structure due to ST phonons around the $\langle 100 \rangle$ directions becomes more rounded and the inner box becomes smaller, and the FT caustics become more widely separated.

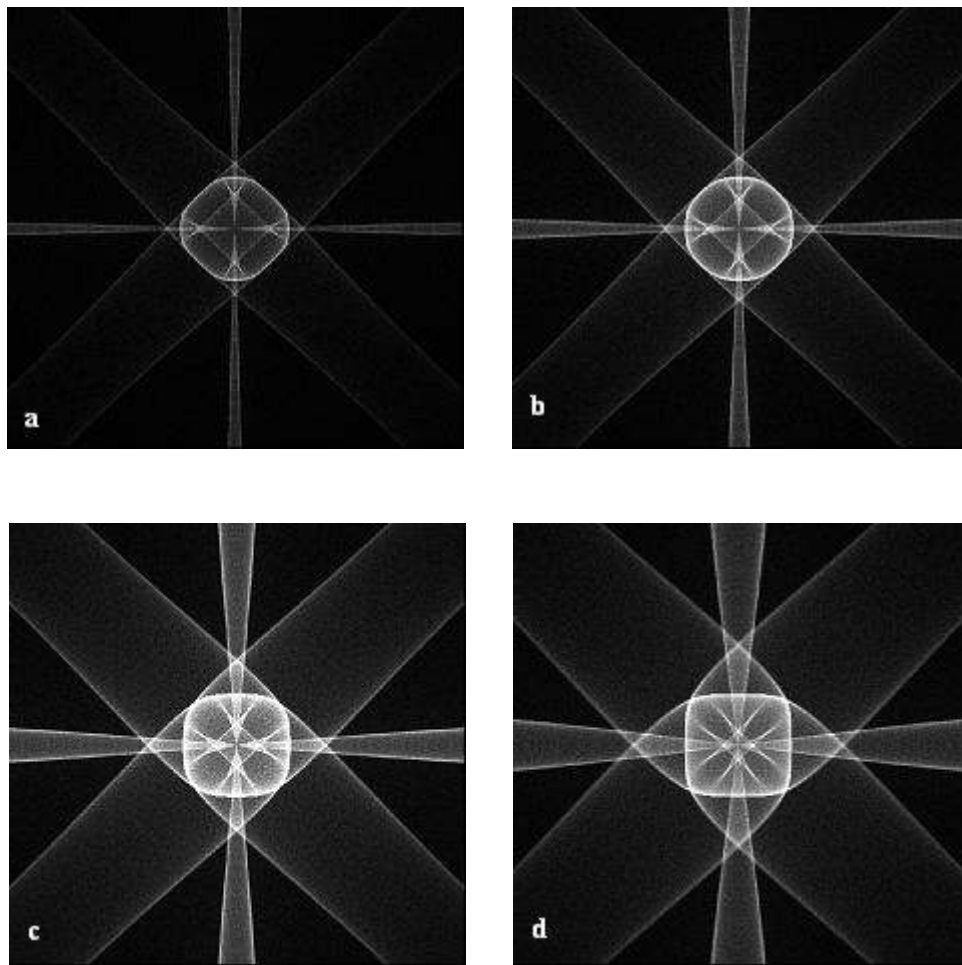


Figure 4.12. Calculated dispersive phonon images of silicon in the (100) imaging plane: (a) 0.0 - 0.3 THz (b) 0.9 - 1.0 THz (c) 1.5 - 1.6 THz (d) 1.9 - 2.0 THz.

Chapter 5

Phonon focusing patterns of InSb and GaAs

Crystals lacking a centre of inversion like InSb and GaAs, which are of T_d symmetry and for which the acoustic gyrotropic tensor is not zero, exhibit the phenomenon of acoustical activity (Portigal and Burstein, 1968 and Every, 1987). This is a fifth rank tensor for which the numbers of independent components for all point groups have been reduced by group theoretical methods by Kumaraswamy and Krishnamurthy in 1980. There is only one independent component of the acoustic gyrotropic tensor in crystals like InSb and GaAs of point group T_d (DiVincenzo, 1986). There is in addition second order dispersion, which is characterized by the f tensor which has the same 6 independent components as for O_h symmetry.

The dispersive phonon focusing patterns of InSb and GaAs are investigated in this chapter. Calculations of the phonon images of InSb have been performed using non-dispersive and dispersive elastic constants obtained using modified continuum elasticity theory as discussed in chapter 3.

5.1 Frequency dependence of dispersive phonon images of InSb in the (110) observation plane

We now discuss the evolution of phonon images of InSb calculated using elastic constants extracted directly from neutron scattering data and compare them with measurements. There is no independent set of parameters derived from lattice dynamics models to compare with. Figure 5.1a shows a non-dispersive phonon image of indium antimonide measured with a bolometric detector. The

corresponding calculated image for the non-dispersive frequencies 0.0 - 0.2THz is shown in figures 5.1b. These images are for the (110) observation plane of the crystal with the [110] direction at the centre. The FT caustics in the calculated image are not quite as widely separated as the ones in the experimental image. However, all other calculated phonon focusing structures conform reasonably well to the measurements. The box structures around the $\langle 100 \rangle$ directions for which the corners are rounded are in qualitatively good agreement.

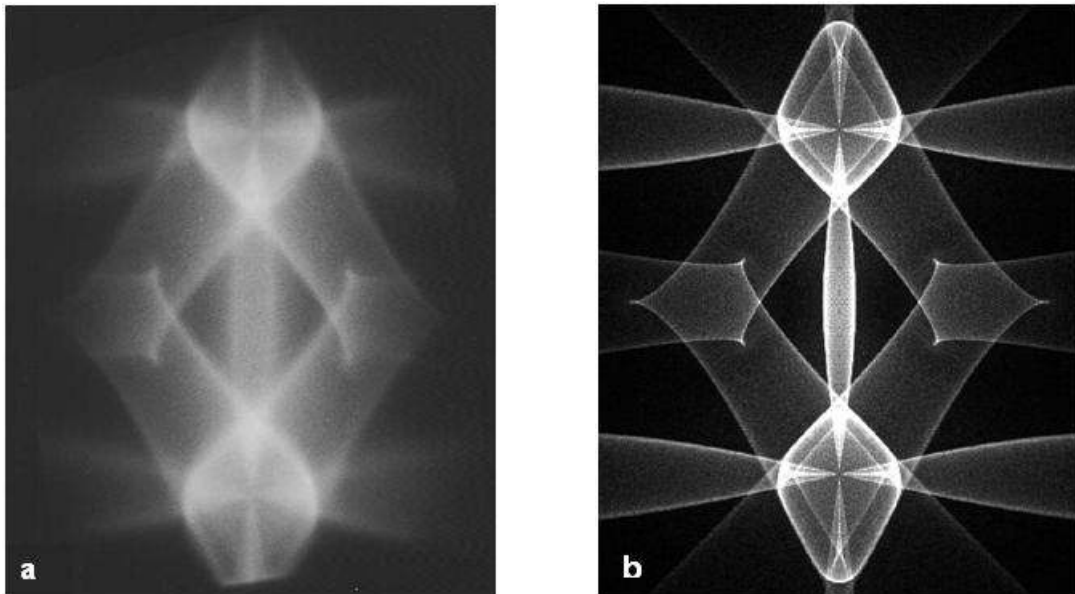


Figure 5.1. Non-dispersive phonon images of InSb in the (110) observation plane. (a) Measured image by Hebboul and Wolfe (1989). (b) Calculated image selecting phonons with frequencies between 0.0 - 0.2 THz.

An image measured using a tunnel junction detector with an onset frequency of 0.43THz is shown in figure 5.2a. In this image, the box structure around the $\langle 100 \rangle$ directions has now become completely rounded. The FT caustics have become even more widely separated and the fast transverse ridge at the center shows relatively very high phonon intensity. A corresponding dispersive

continuum model calculation for the 0.43-0.50 THz frequency range is shown in figure 5.2b. The fast transverse caustics have also become more widely separated in this simulated image and the box structure is now rounded. The inner box is much smaller.

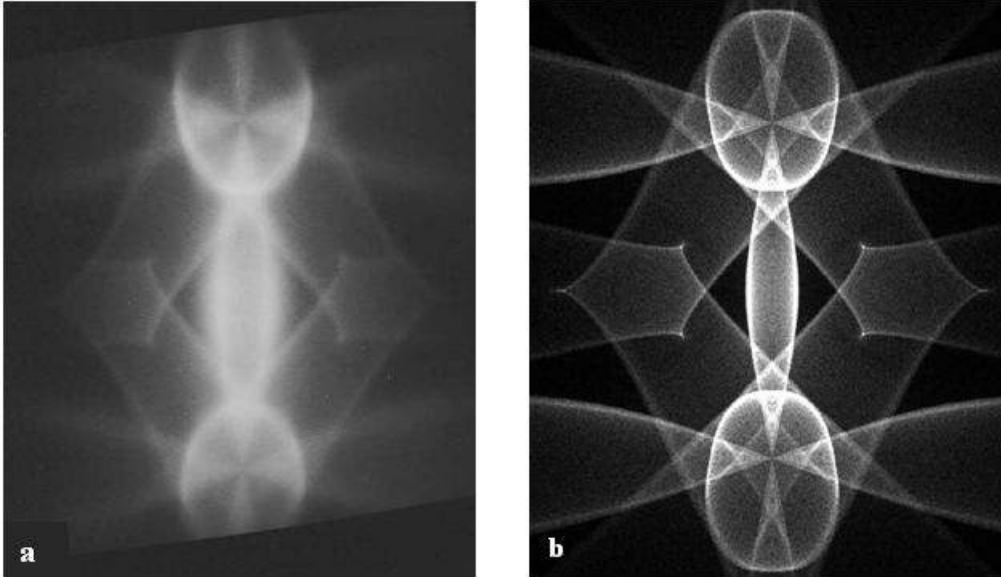


Figure 5.2 Phonon images of InSb in the (110) observation (a) measured image using a tunnel junction detector with an onset frequency of 0.43 THz by Hebboul and Wolfe (1989) (b) Calculated image in the 0.43 - 0.50 THz frequency range.

The image in figure 5.3a was measured with a tunnel junction detector with an onset frequency of 0.593 THz. Striking changes can be seen in the phonon focusing pattern. There is a very high concentration of phonons on the FT ridge connecting the $\langle 100 \rangle$ directions. There is an increase in the distance between the FT caustics. The box structures around the $\langle 100 \rangle$ directions have changed from the rounded shape to a squared shape. A corresponding simulation in the 0.575-0.625THz frequency range is shown in figure 5.3b. In the calculated image, the box structure around the $\langle 100 \rangle$ directions has also become squared.

The inner box in the calculated image has become much smaller. The separation of the FT caustics has increased although by a magnitude that is not quite the same as in the experimental image. The faint focusing structures around the $\langle 111 \rangle$ directions have become larger to the extent that they are almost touching the FT structures near the $\langle 110 \rangle$ directions.

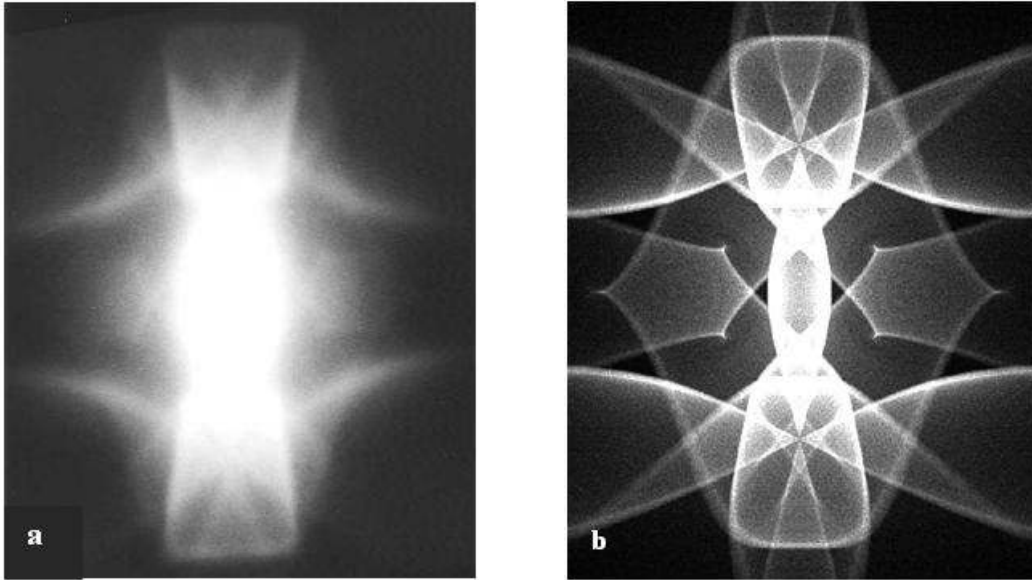


Figure 5.3 Phonon images of InSb in the (110) observation plane (a) Experimental image using a tunnel junction detector with an onset frequency of 0.593THz by Hebboul and Wolfe (1989). (b) Calculated image in the 0.593-0.650 THz frequency range.

A comparison of an experimental phonon image obtained with a detector with onset frequency of 0.688 THz with a simulation in the 0.688 to 0.750 THz frequency range is shown in figures 5.4a and 5.4b. The focusing structure around the $\langle 111 \rangle$ directions is no longer visible in the experimental image whilst it is now touching the FT ridge close to the $\langle 110 \rangle$ directions in the calculated image. The opening angle of the FT caustics has increased in the calculated image as has the one in the experimental image though the

magnitudes are slightly different. The box structures around the $\langle 100 \rangle$ directions are still squared in both images but the edges are slightly concave in the experimental image. The inner box structure has vanished in both the measured image and the calculated image. According to Hebboul and Wolfe (1989), a low frequency focusing pattern is superposed on the high frequency pattern in the measured image. This has been attributed to the tunnel junction detector simultaneously acting as a low and high frequency detector.

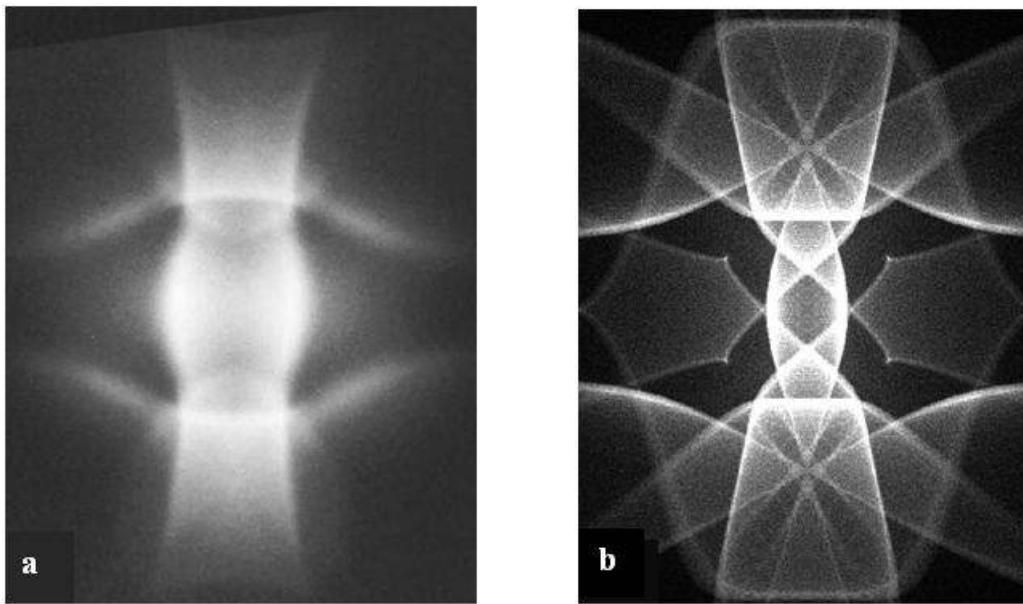


Figure 5.4 Phonon images of InSb in the (110) observation plane (a) measured image using a tunnel junction detector with an onset frequency of 0.688 THz by Hebboul and Wolfe (1989) (b) Calculated image in the 0.688 - 0.750 THz frequency range.

5.2 Evolution of dispersive phonon images of InSb in the (100) observation plane

A discussion of the frequency dependence of the calculated phonon focusing patterns using elastic constants derived directly from neutron scattering data

in the (100) observation plane is carried out in this section. The image of figure 5.5a was calculated for ballistic phonons within the 0.40 to 0.45 THz frequency ranges. The box structure due to ST phonons is completely rounded.

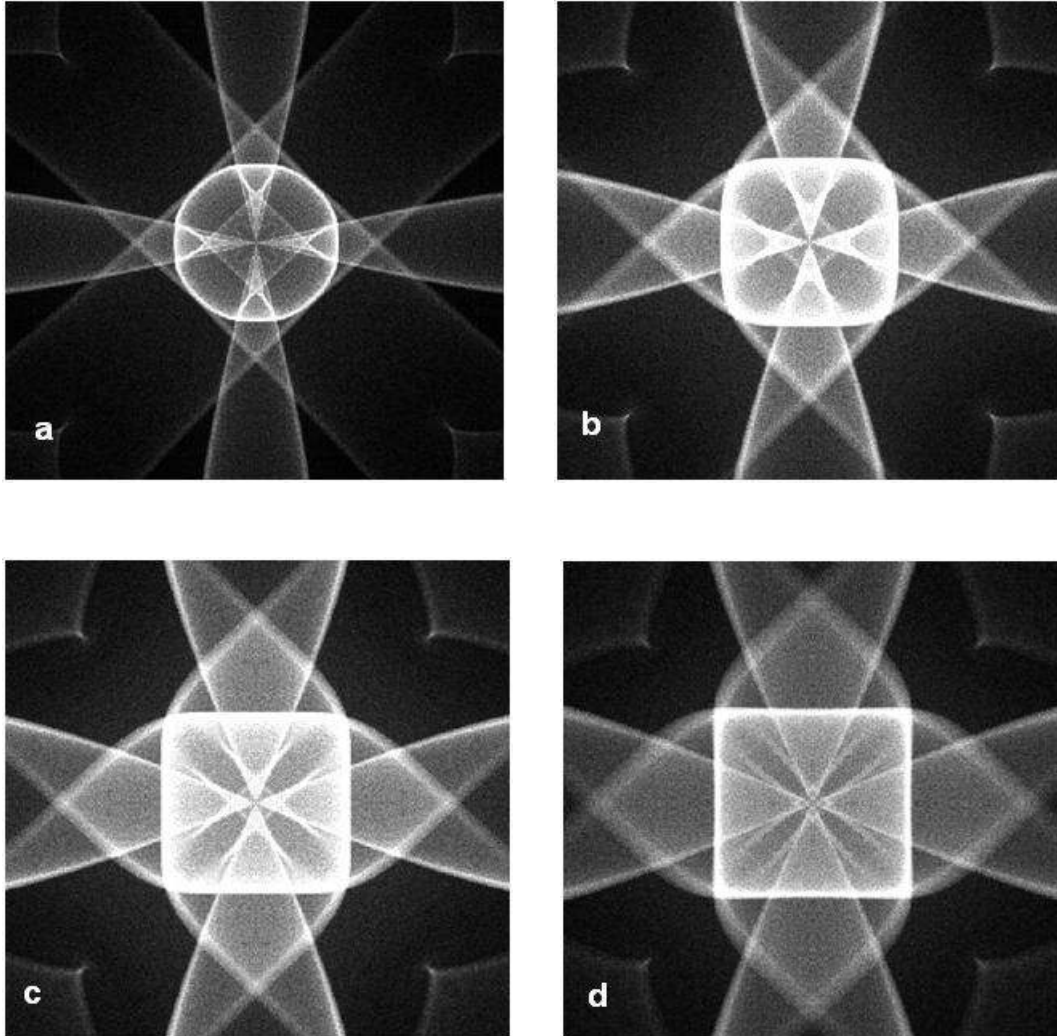


Figure 5.5. Calculated phonon images of InSb in the (100) observation for the: (a) 0.40-0.45THz (b) 0.57-0.62THz (c) 0.66-0.70THz (d) 0.70-0.75THz, frequency ranges.

This shape changes to a squared shape in the 0.57 to 0.62 THz frequency range in figure 5.5b. The inner box around the $\langle 100 \rangle$ directions has become much

smaller and the separation of the horizontal and vertical FT caustics has increased. In figure 5.5c corresponding to calculations selecting phonons with 0.66 to 0.70 THz frequencies, the inner box has become even smaller. It is completely absent in the 0.70 to 0.75 THz phonon image. The FT caustics which are very sharp at 0.4-0.45THz become much broader at 0.7-0.75THz and their opening angle increases to the extent that the distance between them is about doubled. The box structure around the $\langle 100 \rangle$ directions has become almost completely squared.

One may compare the calculated images in figure 5.5 with experimental images of InSb in figure 5.6. The projection plane of the experimental images is (110) which differs from the (100) plane of figure 5.5, but the angular range is similar, capturing the ST box structure (Hebboul and Wolfe, 1988). Figure 5.6a was measured with a frequency tunnel junction detector with an onset frequency of 430 GHz. The box structure around the [100] direction is rounded. This becomes squared in figure 5.6b obtained with a detector with an onset frequency of 593 GHz. The edges of this structure become slightly curved inwards in figures 5.6c and 5.6d obtained with detector onset frequencies of 688GHz and 727GHz respectively.

The inner box in these experimental images is discernible in the image measured using a detector with an onset frequency of 430 GHz. This structure is however, not observed at higher frequencies. The tunnel junction detectors used in these experiments are also sensitive to low frequency phonons and as result a low frequency caustic pattern is superimposed on the focusing pattern in figures 5.6b.

Bearing in mind that the images in figure 5.6 are expanded views about the $\langle 100 \rangle$ directions of images measured in the (110) observation which distorts the comparison with the images calculated in the (100) plane in figure 5.5, the

experimental images in figure 5.6 are reasonably well reproduced by the corresponding calculations in figure 5.5.

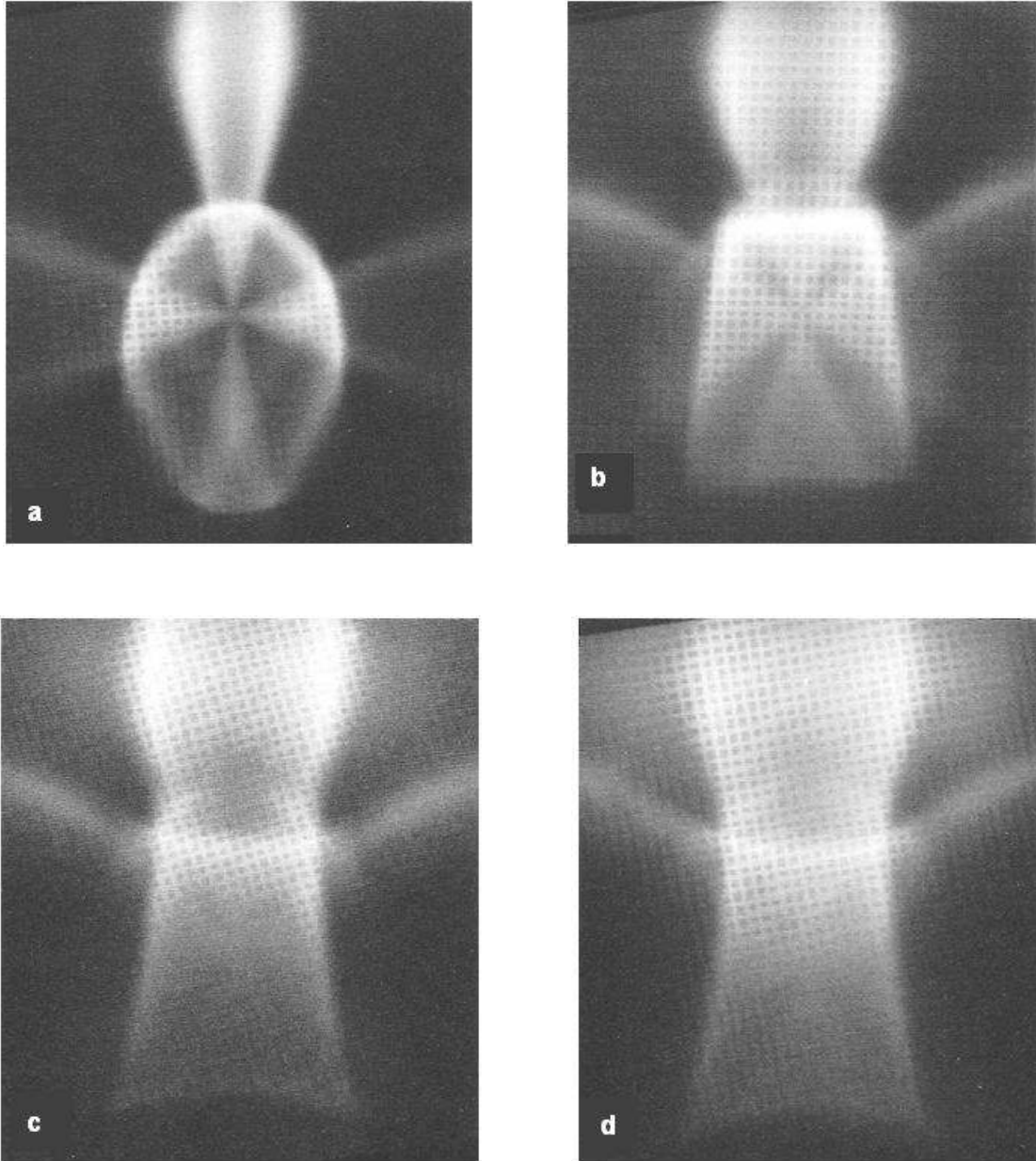


Figure 5.6. Phonon images of InSb measured in the (110) plane with a smaller angular scan to record a magnified view of the focusing structures around the [100] direction. They have been obtained with tunnel junction detectors with onset frequencies of: (a) 430 GHz (b) 593 GHz (c) 688 GHz (d) 727 GHz.

5.3 Comparison of GaAs experimental images with calculated images

Crystals of GaAs also lack a centre of inversion but the method used to extract its dispersive elastic constants from neutron scattering data was slightly different from the one used for InSb. As explained in more detail in chapter 3, this was because neutron scattering data is available for all branches of the dispersion relations of GaAs.

A phonon image measured in the (110) observation plane of GaAs using a bolometric detector is shown in figure 5.7a (Northrop et al, 1985). Phonon focusing structures due to slow transverse and fast transverse modes of propagation have been labeled ST and FT respectively. A corresponding calculated image using elastic constants derived directly from neutron scattering data whilst selecting phonons with frequencies less than 0.3 THz is shown in figure 5.7d. There is very good agreement between the measured and the calculated image. The fast transverse ridge is slightly broader in the experimental image than it is in the calculated image.

In figure 5.7b, a time gate selecting phonons with velocities between 2.9 and 3.1 $\mu\text{m}/\text{ns}$ was used in the image measured with a tunnel junction detector with an onset frequency of 0.7 THz. At these higher frequencies, the diamond shaped structure around the $\langle 100 \rangle$ directions has become rounded and the separation between the FT caustics has increased. The time gate selection results in the absence of the ST phonon focusing structures near the $\langle 111 \rangle$ directions. The changes in the experimental image are well reproduced by the calculated image in figure 5.7e. This image was calculated using the same time gate selection as in the experimental image whilst selecting phonons with frequencies between 0.7 - 1.0 THz.

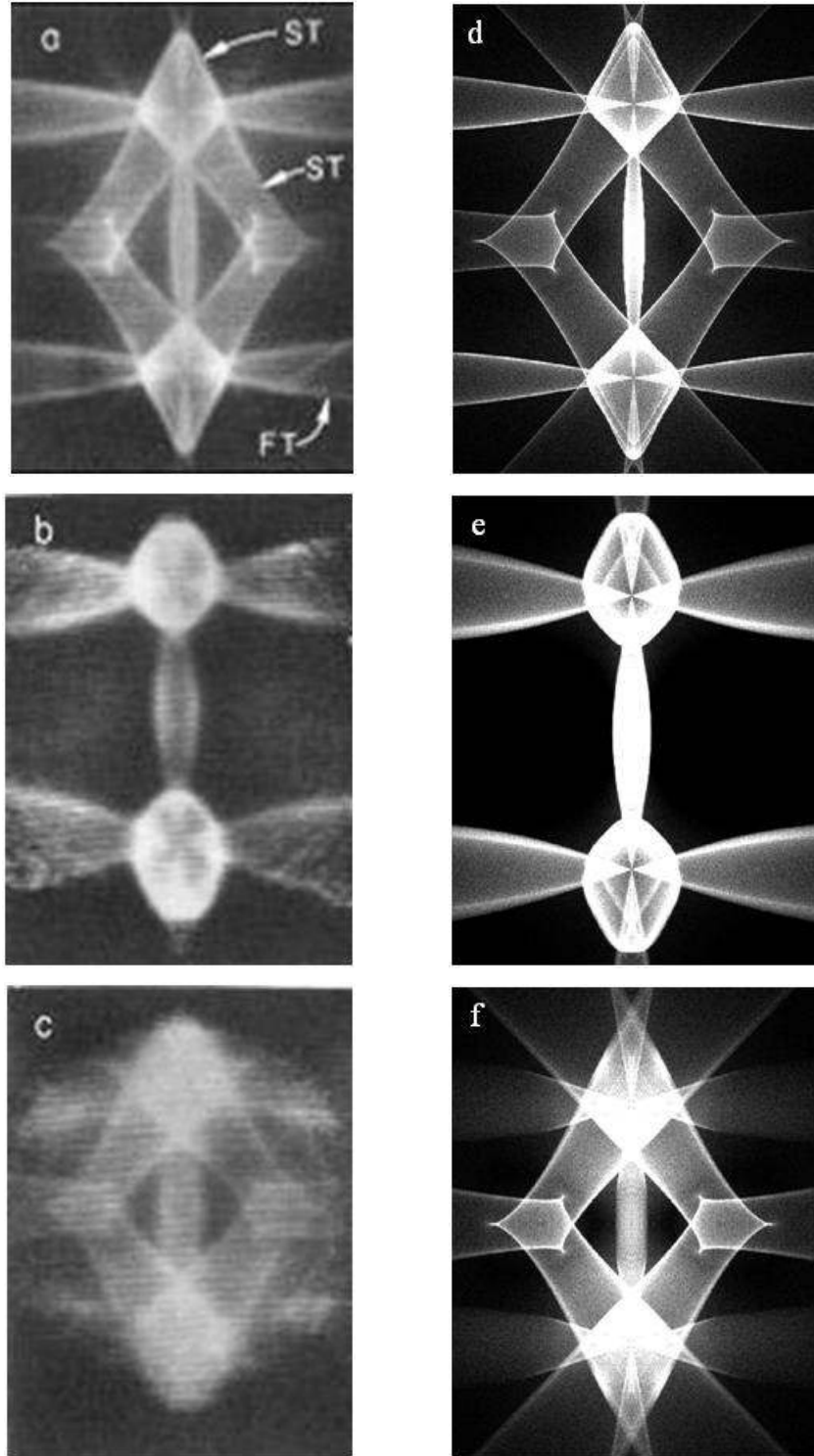


Figure 5.7. Phonon images of GaAs. Measured images by Northrop et al (1985): (a) $f < 0.3$ THz, (b) $f > 0.7$ THz, $2.9 < V < 3.9$ $\mu\text{m}/\text{ns}$, (c) $f > 0.7$ THz, $2.3 < V < 3.1$ $\mu\text{m}/\text{ns}$. Calculated images: (d) $f < 0.3$ THz, (e) $0.7 < f < 1.0$ THz, $2.9 < V < 3.9$ $\mu\text{m}/\text{ns}$, (f) $0.7 < f < 1.0$ THz, $2.3 < V < 3.1$ $\mu\text{m}/\text{ns}$.

Figure 5.7c shows an image measured with a time gate selecting phonons with velocities between 2.3 and 3.1 $\mu\text{m}/\text{ns}$ using a tunnel junction detector with an onset frequency of 0.7 THz. A corresponding image was calculated, figure 5.7f, selecting phonons with frequencies between 0.7 and 1.0 THz whilst using the same time gate selection. The ST phonon focusing structures near the $\langle 111 \rangle$ directions are no longer absent because of the time gate selection which emphasizes slower phonons. The calculated and measured phonon images are all in good agreement.

5.3.1 Comparison of GaAs experimental images with images calculated using DiVincenzo elastic constants

The elastic constants extracted by DiVincenzo (1986) were also used to simulate the focusing patterns of GaAs. A detailed explanation on how the elastic constants are extracted is given in the already named reference.

The experimental phonon images shown in Figure 5.8a, b, and c are the same images shown in figure 5.7a, b and c. They are shown again for comparison with phonon images calculated using non-dispersive and dispersive elastic constants extracted by DiVincenzo (1986). The calculated non-dispersive phonon image in figure 5.8d is in good agreement with the observed non-dispersive phonon image in figure 5.8a.

An image calculated in the 0.7 to 1.0 THz frequency range with time gate selection of phonons with velocities between 2.9 to 3.9 $\mu\text{m}/\text{ns}$ is shown in figure 5.8e. The distance between the fast transverse caustics has increased in the both the simulated image and the experimental image although this is by different magnitudes. The corners of the box structure around the $\langle 100 \rangle$ directions have become rounded. It has a diamond shape in the calculated image whilst it is more circular in the measured image.

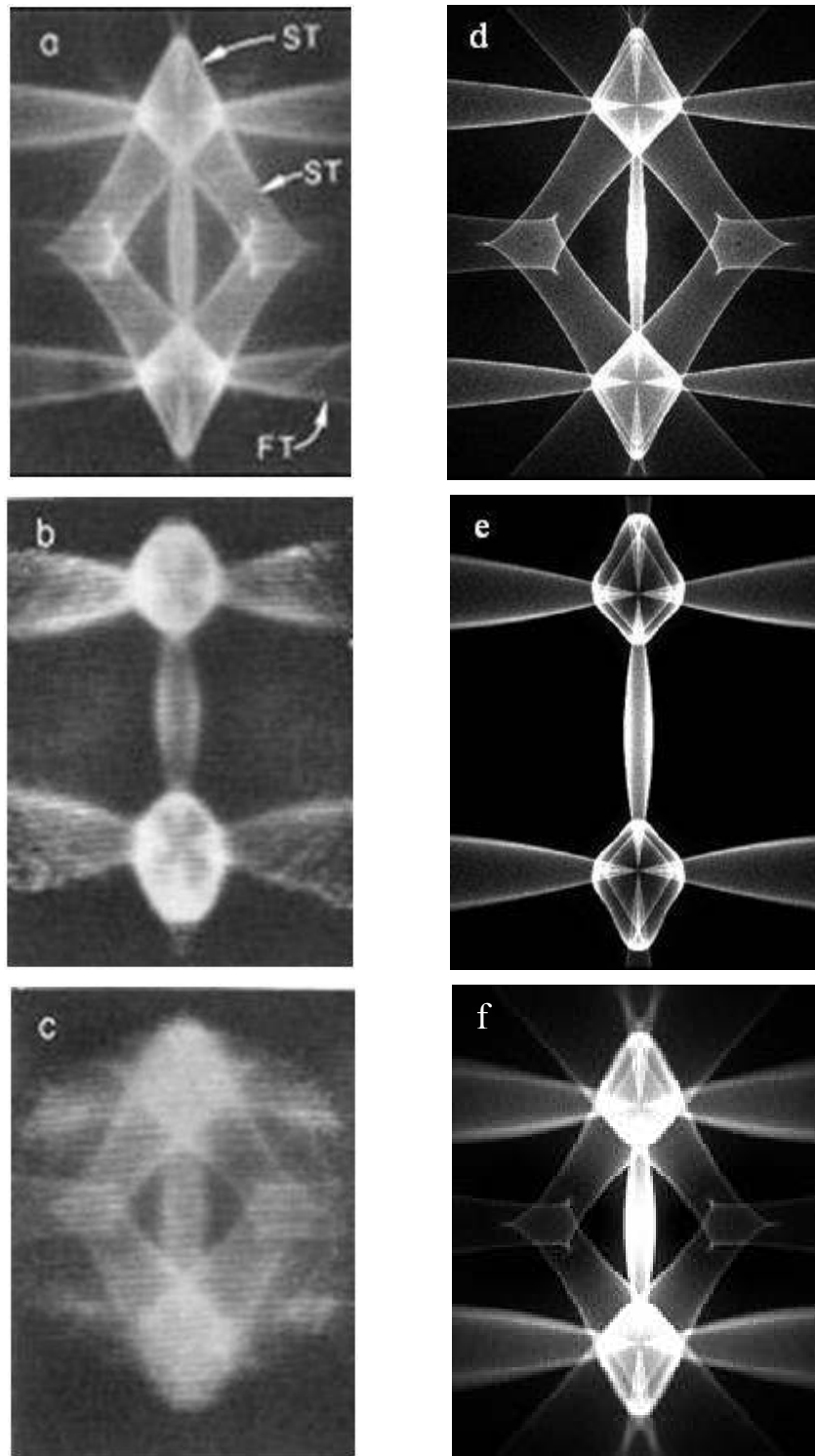


Figure 5.8. Phonon images of GaAs. Measured images by Northrop et al (1985): (a) $f < 0.3$ THz, (b) $f > 0.7$ THz, $2.9 < V < 3.9$ $\mu\text{m}/\text{ns}$, (c) $f > 0.7$ THz, $2.3 < V < 3.1$ $\mu\text{m}/\text{ns}$. Calculated images: (d) $f < 0.3$ THz, (e) $0.7 < f < 1.0$ THz, $2.9 < V < 3.9$ $\mu\text{m}/\text{ns}$, (f) $0.7 < f < 1.0$ THz, $2.3 < V < 3.1$ $\mu\text{m}/\text{ns}$.

The inner box in the simulated image is now smaller than in the non-dispersive case. Time gate selection has also resulted in the absence of the focusing structures around the $\langle 111 \rangle$ directions.

An image corresponding to figure 5.8c was calculated for the 0.7 to 1.0 THz frequency range, see figure 5.8f. A time gate selection of phonons with velocities between 2.3 and 3.1 $\mu\text{m}/\text{ns}$ was used in this simulation. The focusing structures around the $\langle 111 \rangle$ directions are slightly faded in the calculated image and there is very high phonon intensity on the FT ridge connecting the $\langle 100 \rangle$ directions. The experimental images have been qualitatively well reproduced by the calculations.

For the long-wavelength limit images, the elastic constants derived from the shell model and the ones extracted directly from neutron scattering data give a phonon image that is in good agreement with measurements. At higher frequencies however, the measured image is better reproduced by the latter. This is expected since a better fit to experimental data at higher phonon frequencies in the dispersion curves was obtained with elastic constants derived from neutron scattering data.

5.4 Frequency dependence of GaAs dispersive phonon images in the (100) plane

The dispersive phonon images in the (100) observation plane of GaAs were calculated using non-dispersive and dispersive elastic constants which we obtained using the procedure explained in chapter 3. The horizontal and vertical FT caustics become more widely separated in figure 5.9b calculated for the 0.5-0.6THz frequency range when compared to the low frequency image calculated whilst selecting phonons with frequencies less than 0.3THz. The

corners of the box structure become slightly rounded and the inner box structure becomes smaller.

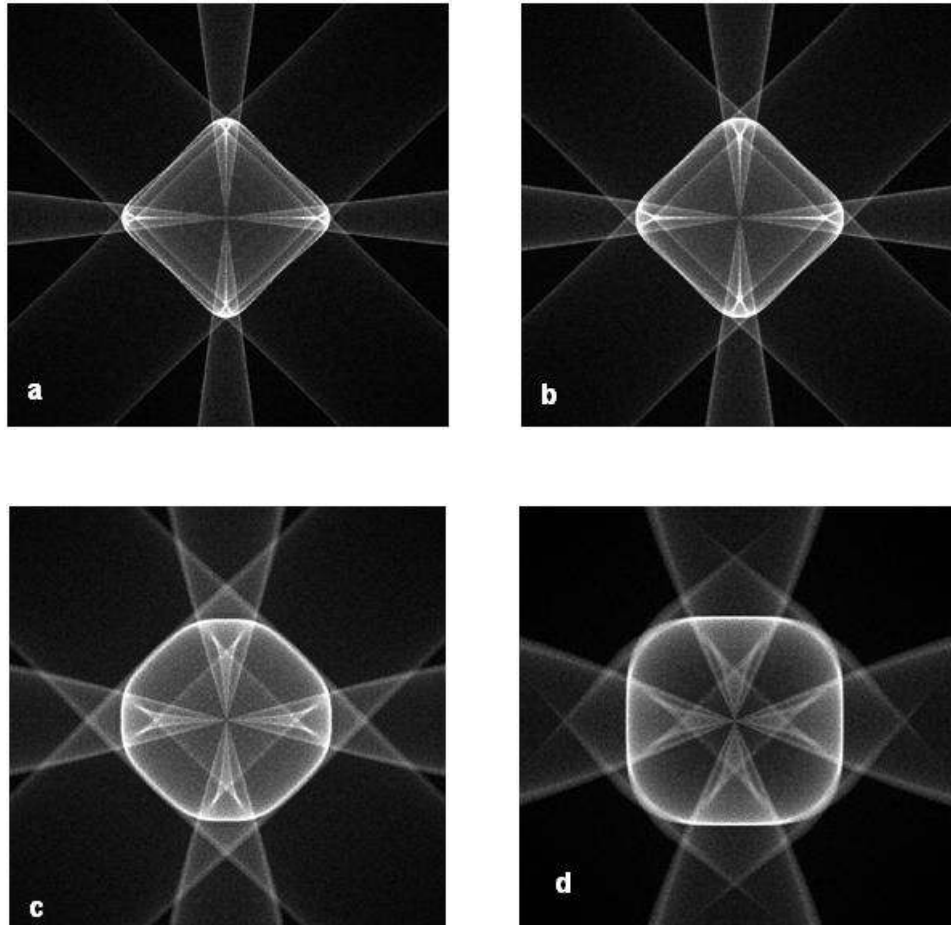


Figure 5.9. Calculated phonon images of GaAs in the (100) plane: (a) $f < 0.3$ THz, (b) $0.5 < f < 0.6$ THz, (c) $1.0 < f < 1.1$ THz, (d) $1.3 < f < 1.4$ THz.

In the 1.0-1.1THz frequency range, see figure 5.9c, the box structure around the $\langle 100 \rangle$ directions acquires a rounded shape and the inner box has become smaller. The separation of the FT caustics has also increased and becomes even larger in figure 5.9d calculated for the 1.3-1.4 THz frequency range. The box structure around the [100] also changes to a squared shape whilst the inner box becomes even smaller.

Chapter 6

Conclusions

Dispersive phonon images of Ge, Si, InSb and GaAs have been calculated using modified continuum elasticity theory. The main aim was to determine if an extension to continuum elasticity theory to include third and fourth order spatial derivatives in the wave equation can be used to explain observed dispersive phonon images of these materials. Experimental neutron scattering data was used to determine the non-dispersive and dispersive elastic constants of all of these crystals that were needed for the imaging calculations.

One of the dispersive elastic constants, the component d of the gyrotropic tensor, is zero in crystals with a centre of inversion such as germanium and silicon. For these two materials neutron scattering data was available for the dispersion curves for the longitudinal and transverse acoustic branches in the $\langle 100 \rangle$, $\langle 110 \rangle$ and $\langle 111 \rangle$ symmetry directions. From these data non dispersive and dispersive elastic constants were obtained by means of optimized fitting to the experimental neutron scattering data along the symmetry directions.

The single independent component of the fifth order elastic tensor is not zero in the two crystals without a centre of inversion, indium antimonide and gallium arsenide. One cannot therefore derive polynomial expressions of the same form as other dispersion relations along the $\langle 110 \rangle$ direction because a surd is involved which has to be solved exactly without approximations. Visual optimization and fitting to dispersion curves along symmetry directions was used to obtain the dispersive elastic constants.

The elastic constants were used in dispersive phonon imaging calculations with a program written in the FORTRAN programming language. In this program, a large number of phonon wave vectors with a random distribution of directions and magnitudes are generated. Then their corresponding group velocity vectors are calculated and projected onto the (100), (111) and (110) observation planes to generate density plots representing phonon images. Our calculation does not include the effects of scattering which may account for some of the disagreements with measurements.

A comparison of the calculated phonon images of germanium with measurements was carried out. The phonon focusing structures in the experimental image are qualitatively well reproduced by the calculation. The box structures around the $\langle 100 \rangle$ direction become rounded at higher frequencies. The separation of the fast transverse caustics also increases in the calculated images as in the experimental images in the (110) observation plane but by different magnitudes. The angle subtended by the FT ridge in the calculated image was measured for each frequency range. Phonon focusing patterns of Ge obtained using elastic constants extracted directly from neutron scattering data were compared to the ones obtained using the shell model by Maranganti and Sharma (2007). It was found that phonon images calculated using elastic constants derived directly from neutron scattering data of Ge give better agreement with experiment when compared to shell model phonon focusing patterns. This may be explained by the fact that the fitting of the shell model parameters to experimental data is carried out simultaneously for all the acoustic and optical modes over the full Brillouin zone. As a result, it is not surprising that it does not give an optimum fit to the acoustic modes near the zone centre. Among the lattice dynamics models, bond charge model calculations of phonon images give the best agreement with observed phonon images for group IV elements (Tamura et al, 1991). However, non-dispersive and dispersive elastic constants of covalently bonded crystals like Ge and Si derived through the medium of the bond charge model could not be found.

Calculated non-dispersive images in the (100) observation plane of silicon were in good agreement with measurements. The changes in the focusing patterns as a result of dispersion were well reproduced by calculations using elastic constants extracted directly from neutron scattering data. The inner box structure around the $\langle 100 \rangle$ directions is smaller in the experimental image than in the calculated image in the 0.7 to 0.8 THz frequency range. The distance between the fast transverse caustics becomes larger. A comparison between phonon images of silicon calculated using elastic constants extracted from molecular dynamics (MD) simulations by Maranganti and Sharma (2007) and measurements was carried out. The MD phonon images did not agree as well with experimental observations as images calculated using elastic constants derived directly from neutron scattering data. A possible explanation is that the fitting of MD elastic constants is carried out for wave vector values near $\mathbf{k} = 0$ (Maranganti, 2007) and as a result one obtains a good fit to experimental data for small wave vector values. At large wave vector values however, a small deviation resulting from the approximations may not give a good fit to the experimental data.

Experimental images of indium antimonide in the (110) plane were compared to calculations using elastic constants extracted directly from neutron scattering data. The effects of dispersion are very significant in the focusing patterns of indium antimonide. The box structure around the $\langle 100 \rangle$ directions changes from a square shape to a rounded one. It then becomes squared again with the edges slightly curved. The inner box becomes smaller as frequency is increased until it vanishes. The fast transverse caustics become much more separated at higher frequencies.

Phonon focusing patterns of gallium arsenide were calculated using dispersive and non-dispersive elastic constants extracted directly from neutron scattering data and then the shell model by DiVincenzo (1986). They were compared to phonon images measured by Northrop et al (1985). The changes in the phonon images as result of

dispersion were well reproduced by the calculations. The images calculated using elastic constants extracted directly from neutron scattering data however, give slightly better agreement with the dispersive experimental phonon images.

On the whole, the position of phonon focusing singularities predicted by continuum elasticity theory modified to incorporate dispersion and using parameters inferred from neutron scattering dispersion relations agrees well with experimental observations. The few discrepancies may be attributable to phonon scattering which was not taken into account in the calculations.

Further investigations on this topic may include the effects of phonon scattering in the calculation of phonon images. An examination of several two and three parameter dispersion relations pertaining to one dimensional continuum elasticity models has just been reported by Mittal and Every (2007). They found out that there is a reasonable fit to the dispersion relations over the entire Brillouin zone by the inclusion of up to the sixth order term of the spatial derivatives in the wave equation.

References

Ashcroft N. W, *Solid state physics*, Saunders College, Philadelphia, (1976).

Dietsche W, Northrop G. A and Wolfe J. P, *Phonon focusing of large-K acoustic phonons in germanium*, Phys. Rev. Lett. **47**, 660 (1981).

DiVincenzo D.P, *Dispersive corrections to continuum elastic theory in cubic crystals*, Phys. Rev. B, **34**, 5450 (1986).

Dolling G, *Lattice vibrations in crystals with the diamond structure, in Inelastic scattering of neutrons in solids and liquids Volume II*, IAEA, Vienna, (1963).

Dolling G and Waugh J L T, *Normal vibrations in gallium arsenide, in Lattice Dynamics, Proceedings of the international conference held at Copenhagen, Denmark*, edited by R. F. Wallis, Pergamon, London, (1963).

Eisenmenger W, *Phonon detection by the fountain pressure in superfluid helium films, in Phonon scattering in condensed matter*, (ed) Maris H. J, Plenum Press, New York, (1980).

Every A G, *Effects of first-order spatial dispersion on phonon focusing: Application to quartz*, Phys. Rev. B **36**, 1448 (1987).

Every A G, *Weak spatial dispersion and the unfolding of wave arrival singularities in the elastodynamic Green's functions of solids*, Phys. Rev. B **72**, 104302 (2005).

Every A G, *Ballistic phonons and the shape of the ray surface in cubic crystals*, Phys. Rev. B **24**, 3456 (1981).

Every A G, *Formation of phonon-focusing caustics in crystals*, Phys. Rev. B. **34**, 2852 (1986).

Every A. G. and McCurdy A.K, *Landolt-Börnstein series, Low frequency properties of dielectric crystals: Second and higher order elastic constants*, (ed) Nelson D.F, (1992).

Every A.G and Stoddart A.J, *Phonon focusing in cubic crystals in which transverse phase velocities exceed the longitudinal phase velocity in some direction*, Phys. Rev. B **32**, 1319 (1985).

Every A.G. *Handbook of elastic properties of solids, liquids and gases volume 1: Dynamic methods for measuring the elastic properties of solids Chapter 1*. (ed) Moises Levy, Academic Press, (2001).

Goldstein H, *Classical Mechanics*. Addison-Wesley, Cambridge, MA, (1950).

Hebboul S.E and Wolfe J.P, *Imaging of large-K phonons in InSb*, Phys. Rev. B **34**, 3948 (1986).

Hebboul S.E and Wolfe J.P, *Lattice dynamics of InSb from phonon imaging*, Z.Phys B - Condensed Matter **73**, 437 (1989).

Huet D, Maneval J.P and Zylbersztejn A, *Measurement of Acoustic-Wave Dispersion in Solids*, Phys. Rev. Lett. **29**, 1092 (1972).

Hurley D.C and Wolfe J.P, *Phonon focusing in cubic crystals*, Phys. Rev. B. **32**, 2568 (1985).

Kittel C, *Introduction to solid state physics*, John Wiley and Sons, USA, (1956).
Krumhansl J A, *Mechanics of generalized continua*, edited by E. Kroner, Springer, Berlin, (1968).

Kumaraswamy K and Krishnamurthy N, *The acoustic gyrotropic tensor in crystals*, Acta. Cryst, A **36**, 760 (1980).

Kunc K, Balkanski M and Nusimovici M A, *Lattice Dynamics of Several AN-B8-N Compounds Having the Zincblende Structure. Pt.1. Deformable-Bond Approximation*, Phys. Status. Solidi (b) **71**, 341 (1975).

Lax. M. *Symmetry Principles in Solid State and Molecular Physics*, John Wiley and Sons, New York, (1974).

Maranganti R and Sharma P, *A novel atomistic approach to determine strain-gradient elasticity constants: Tabulation and comparison for various metals, semiconductors, silica, polymers and the (Ir) relevance for nanotechnologies*, J. Mech. Phys. Solids **55**, 1823 (2007).

Maris H.J, *Enhancement of heat pulses in crystals due to elastic anisotropy*, J. Acoust. Soc. Am. **50**, 812 (1971).

McCurdy A. K, *Phonon focusing and phonon conduction in hexagonal crystals in the boundary-scattering regime*, Phys. Rev. B. **9**, 466 (1974).

Metzger W and Huebener R.P, *Phonon focusing in [001] germanium*, Z. Phys. B **73**, 33 (1988).

Mittal R and Every A G, *Modification of the elastic wave equation of a solid for the effects of spatial dispersion* (in press).

Nilsson G and Nelin G, *Phonon Dispersion Relations in Ge at 80 °K*, Phys. Rev. B **3**, 364 (1971).

Nilsson G and Nelin G, *Study of the Homology between Silicon and Germanium by Thermal-Neutron Spectrometry*, Phys. Rev. B **6**, 3777 (1972).

Northrop G.A and Wolfe J.P, *Ballistic phonon imaging in germanium*, Phys. Rev. B **22**, 6196 (1980).

Northrop G.A and Wolfe J.P, *Ballistic Phonon Imaging in Solids—A New Look at Phonon Focusing*, Phys. Rev. Lett. **43**, 1424 (1979).

Northrop G.A, Hebboul S.E and Wolfe J.P, *Lattice dynamics from phonon imaging*, Phys. Rev. Lett. **55**, 95 (1985).

Northrop G.A, *Phonon focusing of dispersive phonons in Ge*, Phys. Rev. B **26**, 903 (1982).

Nye J.F, *Physical properties of crystals: Their representation by tensors and matrices*, Clarendon Press, Oxford, (1957).

Portigal D.L and Burstein E, *Acoustical Activity and Other First-Order Spatial Dispersion Effects in Crystals*, Phys. Rev. **170**, 673 (1968).

Press W. H, Teukolsky S.A, Vetterling W.T, Flannery P.B. *Numerical Recipes in FORTRAN: The Art of Scientific Computing*, CUP, New York, (1992).

Price D L, Rowe J M and Nicklow R M, *Lattice Dynamics of Grey Tin and Indium Antimonide*, Phys. Rev. B **3**, 1268 (1971).

Ramsbey R.T, Wolfe J.P and Tamura S, *Phonon focusing of elastically scattered phonons in GaAs*, Z. Phys B - Condensed Matter **73**, 167(1988).

Rustagi K C and Weber W, *Adiabatic bond charge model for the phonons in A^3B^5 semiconductors*, Solid State Commun. **18**, 673, (1976).

Shields J.A and Wolfe J.P, *Measurement of a phonon hot spot in photoexcited Si*, Z. Phys B - Condensed Matter **75**, 11(1989).

Tamura S, Shields J.A and Wolfe J.P, *Lattice dynamics and elastic phonon scattering in silicon*, Phys. Rev. B **44**, 3001(1991).

Tamura S and Harada T, *Focusing of large-wave-vector phonons in GaAs*, Phys. Rev. B. **32**, 5245 (1985).

Tamura S and Nakane Y, *Applicability and limitations of the phonon-focusing theory based on geometrical acoustics*, Phys. Rev. B **24**, 4317(1981).

Tamura S, *Focusing of high-frequency dispersive phonons*, Phys. Rev. B. **25**, 1415 (1982).

Tamura S, *Large-wave-vector phonons in highly dispersive crystals: Phonon-focusing effects*, Phys. Rev. B. **28**, 897(1983).

Shields J.A, Tamura S and Wolfe J.P, *Elastic scattering of acoustic phonons in Si*, Phys. Rev. B **43**, 4966(1991).

von Gutfeld R. J and Nethercot A.H, *Heat pulses in quartz and sapphire at low temperatures*, Phys. Rev. Lett. **12**, 641(1964).

Wolfe JP, *Imaging of phonons*, CUP, Cambridge, (1998).

Publications

1. Every A. G and Jakata K, *Spatial dispersion in acoustic wave propagation, Proceedings of the 3rd International Conference of the African Materials Research Society*, Journal of Physics, Conference Series, to be published (2007).
2. Jakata K and Every A. G, *Frequency dependence of dispersive phonon images*, South African Journal of Science, submitted for publication (2007).
3. Jakata K and Every A. G, *Determination of the dispersive elastic constants of the cubic crystals Ge, Si, GaAs and InSb*, Physical Review B, submitted for publication (2008).

Conferences and presentations

1. Jakata K and Every A. G, *Spatial dispersion in phonon imaging*, International Symposium on Mechanical Waves in Solids, in Hangzhou, China (2006).
2. Jakata K and Every A. G, *Spatial dispersion in phonon imaging*, Nanjing University, Nanjing, China (2006).
3. Jakata K and Every A. G, *Spatial dispersion in phonon imaging*, Tongji University, Shanghai, China (2006).
4. Jakata K and Every A. G, *Spatial dispersion effects in phonon imaging*, South African Institute of Physics, 51st Annual Conference, in Cape Town, South Africa (2006).
5. Jakata K and Every A. G, *Frequency dependence of dispersive phonon images*, South African Institute of Physics, 52nd Annual Conference, in Johannesburg, South Africa (2007).

6. Jakata K and Every A. G, *Frequency dependence of dispersive phonon images*, School of Physics, University of the Witwatersrand, Johannesburg, South Africa (2007).

Appendix

Dispersive phonon imaging program

The FORTRAN program to calculate the dispersive phonon images is given below. Comments are written in italics preceded by a bold **C**. Units used are such that most quantities in phonon imaging are of the order unity. Lengths are in microns, μm , and time in nanoseconds, frequencies in gigahertz and mass in pico-gramms.

```
PROGRAM image
```

C *This program calculates the dispersive phonon images of Ge .We start by defining the variables and the output files, disp100.dat, disp110.dat and disp111.dat for the images in the (100), (110) and (111) observation planes respectively.*

```
Implicit Real*8 (a-h,o-z)
```

```
Real*8 w(3),Velx0(3),Vely0(3),Velz0(3)
```

```
Complex*16 roots(3), a(4),xi
```

```
Integer*2 Ins100(500,500),Irow0(500),Ins110(500,500),Irow1(500)
```

```
Integer*2 Ins111(500,500),Irow2(500)
```

```
OPEN (UNIT=60,FILE='D:\fortran\kuda\disp100d.dat',STATUS='NEW')
```

```
OPEN (UNIT=61,FILE='D:\fortran\kuda\disp110d.dat',STATUS='NEW')
```

```
OPEN (UNIT=62,FILE='D:\fortran\kuda\disp111d.dat',STATUS='NEW')
```

C *Elastic constants of germanium are defined. The non-dispersive elastic constants are c11, c12 and c44 and the dispersive elastic constants f1, f2, f3, f4, f5, f6 and d. P is the density of germanium and wav is the lattice parameter. The non-dispersive elastic constants*

```
c11 = 139.80d00
```

```
c12 = 56.00d00
```

```
c44 = 69.80d00
```

```
f1 = -8.028979900488998d-007
```

f2 = -1.505796005572888d-006

f3 = -7.673999747267629d-009

f4 = -4.891560156042842d-007

f5 = -4.387499927815952d-007

f6 = 3.196740010480426d-007

d = 0.00d00

p = 5.36d00

wav = 5.651d-04

C the constant pi

pi = 3.141592653589793d00

C defining numbers often encountered and square roots in double precision.

t2 = 2.00d0

t3 = 3.00d0

t4 = 4.00d0

t6 = 6.00d0

t12= 12.00d0

t24=24.00d0

sqr2=1.00d00/dsqrt(t2)

sqr3=1.00d00/dsqrt(t3)

sqr6=1.00d00/dsqrt(t6)

C Setting dimensions of imaging plane. The variable dstx is the length along the x axis and dsty is the length along the y axis. This is divided into 500 by 500 bins by dividing the x and y lengths by 500. The variable h is the distance from the phonon source to the centre of the imaging plane.

dstx = 10.00d03

dsty = 10.00d03

dincx = dstx/500.0d00

dincy = dsty/500.0d00

h = 10.00d03

C Defining the wave vector, dK in reduced wave vectors.

dK= t2*pi/wav

C Arrays Ix, Iy and Iz to generate phonon wave vectors in the x, y and z directions.

DO 52 Ix = -120,120

DO 51 Iy = -120,120

DO 50 Iz = -120,120

dKx = (dfloat(Ix)+ rand())*0.300d0/120.0d0

dKy = (dfloat(Iy)+ rand())*0.300d0/120.0d0

dKz = (dfloat(Iz)+ rand())*0.300d0/120.0d0

dmodK = sqrt(dKx*dKx + dKy*dKy + dKz*dKz)

C Selecting wave vector magnitudes less than 0.3

IF(dmodK.gt.0.0d0.AND.dmodK.lt.0.3d0) THEN

x = dK*dKx

y = dK*dKy

z = dK*dKz

*C Having generated wave vectors, we now call a subroutine *FREQ* to calculate the group velocity vectors. We input the wave vectors components x, y, and z, the elastic constants, the density of the material and the lattice parameter. The output of the subroutine are the components of the group velocity vectors in the x, y and z directions and the phonon angular frequencies for the ST, FT and L modes w(j). The subroutine *FREQ* is written at the end of this program.*

```
CALL FREQ(x,y,z,c11,c12,c44,f1,f2,f3,f4,f5,f6,d1,p,  
1 Velx0,Vely0,Velz0,w)
```

C From the angular frequencies we calculate the phonon frequencies in gigahertz and then select the range of frequencies required in the phonon image. In this case, we are selecting phonon frequencies in the 500GHz to 600GHz range. As a method of checking for the consistency of these calculations, dispersion curves can be plotted and compared to neutron scattering data along the symmetry directions of the crystal.

```
DO 38 j=1,2  
  frq= w(j)/(t2*pi)  
  IF(frq.gt.500.00d00.AND.frq.lt.600.00d0) THEN
```

C For the range of frequencies selected above, we now use the symmetry of the crystal for the group velocity vectors.

```
DO 23 mx = -1, 1, 2  
DO 22 my = -1, 1, 2  
DO 21 mz = -1, 1, 2  
DO 20 mi = 1, 6  
  
IF (mi.eq.1) THEN  
  Velx = Velx0(j)*mx  
  Vely = Vely0(j)*my  
  Velz = Velz0(j)*mz  
ELSE IF(mi.eq.2) THEN  
  Velx = Velx0(j)*mx  
  Vely = Velz0(j)*my  
  Velz = Vely0(j)*mz  
ELSE IF(mi.eq.3) THEN
```

```

Velx = Vely0(j)*mx
Vely = Velx0(j)*my
Velz = Velz0(j)*mz
ELSE IF(mi.eq.4) THEN
    Velx = Vely0(j)*mx
    Vely = Velz0(j)*my
    Velz = Velx0(j)*mz
ELSE IF(mi.eq.5) THEN
    Velx = Velz0(j)*mx
    Vely = Velx0(j)*my
    Velz = Vely0(j)*mz
ELSE IF (mi.eq.6) THEN
    Velx = Velz0(j)*mx
    Vely = Vely0(j)*my
    Velz = Velx0(j)*mz
END IF

```

C We now find the number of group velocity vectors falling into each one of the 500 by 500 bins on the imaging planes. For example, in the (100) plane, qx_0 and qy_0 are the x and y distances where the group velocity vectors intersect with the imaging plane. nx and ny are their coordinates on the observation plane.

C For the (100) observation plane

```

IF( Velz.gt.0.0d0) THEN
    qx0 = h*Velx/Velz
    qy0 = h*Vely/Velz

    nx = IDINT(qx0/dincx) + 250
    ny = IDINT(qy0/dincy) + 250

```

```

IF(qx0.lt.0.0d0)nx=nx-1
IF(qy0.lt.0.0d0)ny=ny-1
IF (nx.lt.501.AND.nx.gt.0) THEN
IF(ny.lt.501.AND.ny.gt.0) THEN
Ins100(nx,ny) = Ins100(nx,ny)+1
END IF
END IF
END IF

```

C For the (110) observation plane

```

Vzp = (Velx-Vely)*sqr2
IF (Vzp.gt.0.0d0) THEN
Vxp = (Velx+Vely)*sqr2
Vyp = Velz
qx1 = h*Vxp/Vzp
qy1 = h*Vyp/Vzp

nx = IDINT(qx1/dincx) + 250
ny = IDINT(qy1/dincy) + 250
IF(qx1.lt.0.0d0)nx=nx-1
IF(qy1.lt.0.0d0)ny=ny-1
IF (nx.lt.501.AND.nx.gt.0) THEN
IF(ny.lt.501.AND.ny.gt.0) THEN
Ins110(nx,ny) = Ins110(nx,ny)+1

END IF
END IF
END IF

```

C For the (111) observation plane

$$V_{zp1} = (V_{elx} + V_{ely} + V_{elz}) * \text{sqr}3$$

IF (Vzp1.gt.0.0d0) THEN

$$V_{xp1} = (V_{ely} - V_{elx}) * \text{sqr}2$$

$$V_{yp1} = (-V_{elx} - V_{ely} + t2 * V_{elz}) * \text{sqr}6$$

$$q_{x2} = h * V_{xp1} / V_{zp1}$$

$$q_{y2} = h * V_{yp1} / V_{zp1}$$

$$n_x = \text{IDINT}(q_{x2} / d_{incx}) + 250$$

$$n_y = \text{IDINT}(q_{y2} / d_{incy}) + 250$$

IF (q_{x2}.lt.0.0d0) n_x=n_x-1

IF (q_{y2}.lt.0.0d0) n_y=n_y-1

IF (n_x.lt.501.AND.n_x.gt.0) THEN

IF (n_y.lt.501.AND.n_y.gt.0) THEN

$$\text{Ins111}(n_x, n_y) = \text{Ins111}(n_x, n_y) + 1$$

END IF

END IF

END IF

20 CONTINUE

21 CONTINUE

22 CONTINUE

23 CONTINUE

END IF

38 CONTINUE

END IF

50 CONTINUE
51 CONTINUE
52 CONTINUE

C Writing to image files

```
DO 65 Iw=1,500
DO 60 Iv=1,500
IF(Ins100(Iw,Iv).gt.99) THEN
Ins100(Iw,Iv)=99
END IF
Ins100(Iw,Iv) = 99 - Ins100(Iw,Iv)
Irow0(Iv) = Ins100(Iw,Iv)

IF(Ins110(Iw,Iv).gt.99) THEN
Ins110(Iw,Iv)=99
END IF
Ins110(Iw,Iv) = 99 - Ins110(Iw,Iv)
Irow1(Iv) = Ins110(Iw,Iv)

IF(Ins111(Iw,Iv).gt.99) THEN
Ins111(Iw,Iv)=99
END IF
Ins111(Iw,Iv) = 99 - Ins111(Iw,Iv)
Irow2(Iv) = Ins111(Iw,Iv)
```

60 CONTINUE

Write(60,120)Irow0

Write(61,120)Irow1

Write(62,120)Irow2

65 CONTINUE

120 Format(1x,500I3)

123 Format(1x,3F12.6)

END

C Subroutine *FREQ*

*C The wave vector components in the x, y and z Cartesian directions, the elastic constants, density of the material and the lattice parameter are input from the main program. This subroutine outputs the group velocity components *Velx0*, *Vely0* and *Velz0* and the phonon angular frequencies for the ST, FT and L modes, *w(j)*.*

SUBROUTINE *FREQ*(x,y,z,c11,c12,c44,f1,f2,f3,f4,f5,f6,d1,p,Velx0,Vely0,Velz0,w)

C Defining variables

Implicit Real*8 (a-h,o-z)

Real*8 w(3),Velx0(3),Vely0(3), Velz0(3)

Complex*16 roots(3),a(4),xi

C Defining numbers used frequently in the program in double precision

t2=2.00d0

t3=3.00d0

t4=4.00d0

t6=6.00d0

t12=12.00d0

t24=24.00d0

C Defining powers of variables used frequently

$$x2 = x**2$$

$$y2 = y**2$$

$$z2 = z**2$$

$$x3 = x**3$$

$$y3 = y**3$$

$$z3 = z**3$$

$$x4 = x**4$$

$$y4 = y**4$$

$$z4 = z**4$$

C Calculating the components of the dynamical matrix for each phonon wave vector, see section 3.1.

$$Q = c11*x2 + c44*(y2+z2) + f1*x4 + f2*(y4 + z4)$$

$$l + t6*f3*y2*z2 + t6*f4*x2*(y2 + z2)$$

$$R = c11*y2 + c44*(x2+z2) + f1*y4 + f2*(x4 + z4)$$

$$l + t6*f3*x2*z2 + t6*f4*y2*(x2 + z2)$$

$$S = c11*z2 + c44*(x2+y2) + f1*z4 + f2*(x4 + y4)$$

$$l + t6*f3*x2*y2 + t6*f4*z2*(x2 + y2)$$

$$T = (c12+c44)*x*y + t4*f5*(x*y3 + x3*y) + t12*f6*x*y*z2$$

$$U = (c12+c44)*x*z + t4*f5*(x*z3 + x3*z) + t12*f6*x*z*y2$$

$$V = (c12+c44)*y*z + t4*f5*(y*z3 + y3*z) + t12*f6*y*z*x2$$

$$Tp=t3*d1*z*(x2 - y2)$$

$$Up=t3*d1*y*(z2 - x2)$$

$$V_p = t_3 * d_1 * x * (y^2 - z^2)$$

C Calculating the four coefficients of the cubic equation in $\lambda = \rho\omega^2$, see chapter 3, equation (3.12).

$$b = -1.0d_0$$

$$c = Q + R + S$$

$$d = T * T + T_p * T_p + U * U + U_p * U_p + V * V + V_p * V_p - Q * R - R * S - S * Q$$

$$e = Q * R * S - T * T * S - T_p * T_p * S - U * U * R - U_p * U_p * R - V * V * Q - V_p * V_p * Q$$

$$1 + t_2 * T * U * V - t_2 * T * U_p * V_p - t_2 * T_p * U * V_p - t_2 * T_p * U_p * V$$

C The four coefficients of the cubic equation are put into an array $a(4)$

$$a(1) = e$$

$$a(2) = d$$

$$a(3) = c$$

$$a(4) = b$$

C The coefficients of the cubic equation are input into a subroutine ZROOTS together with the number of required roots, 3. A detailed explanation of this root finding subroutine is found in the book *Numerical Recipes in FORTRAN* (Press et al, 1992). The output of this routine is the roots of the polynomial which in this case are the angular frequencies of each one of the ST, FT and L modes, $w(1)$, $w(2)$ and $w(3)$. The output frequencies are complex numbers so we take the real part only.

CALL ZROOTS(a,3,roots,TRUE)

$$w(1) = \text{dsqrt}(\text{dreal}(\text{roots}(1))/p)$$

$$w(2) = \text{dsqrt}(\text{dreal}(\text{roots}(2))/p)$$

$$w(3) = \text{dsqrt}(\text{dreal}(\text{roots}(3))/p)$$

C In order to calculate the group velocity vectors, the gradient of the cubic equation (3.12) was calculated in the way shown in equation (3.44). In this part of the program, we have the partial derivatives of the components of the dynamical matrix (3.11). For example, Q_x refers to the partial derivative of Q with respect to wave vector component in the x direction.

DO 38 j=1,3

$$Q_x = t2*c11*x + t4*f1*x3 + t12*f4*x*(y2 + z2)$$

$$Q_y = t2*c44*y + t4*f2*y3 + t12*f3*y*z2 + t12*f4*x2*y$$

$$Q_z = t2*c44*z + t4*f2*z3 + t12*f3*y2*z + t12*f4*x2*z$$

$$R_x = t2*c44*x + t4*f2*x3 + t12*f3*x*z2 + t12*f4*y2*x$$

$$R_y = t2*c11*y + t4*f1*y3 + t12*f4*y*(x2 + z2)$$

$$R_z = t2*c44*z + t4*f2*z3 + t12*f3*x2*z + t12*f4*y2*z$$

$$S_x = t2*c44*x + t4*f2*x3 + t12*f3*x*y2 + t12*f4*z2*x$$

$$S_y = t2*c44*y + t4*f2*y3 + t12*f3*x2*y + t12*f4*z2*y$$

$$S_z = t2*c11*z + t4*f1*z3 + t12*f4*z*(x2 + y2)$$

$$T_x = (c12 + c44)*y + t4*f5*(y3 + t3*x2*y) + t12*f6*y*z2$$

$$T_y = (c12 + c44)*x + t4*f5*(t3*x*y2 + x3) + t12*f6*x*z2$$

$$T_z = t24*f6*x*y*z$$

$$T_{px} = t6*d1*z*x$$

$$T_{py} = -t6*d1*z*y$$

$$T_{pz} = t3*d1*(x2 - y2)$$

$$U_x = (c_{12} + c_{44}) * z + t_4 * f_5 * (z^3 + t_3 * x^2 * z) + t_{12} * f_6 * z * y^2$$

$$U_y = t_{24} * f_6 * x * z * y$$

$$U_z = (c_{12} + c_{44}) * x + t_4 * f_5 * (t_3 * x * z^2 + x^3) + t_{12} * f_6 * x * y^2$$

$$U_{px} = -t_6 * d_1 * y * x$$

$$U_{py} = t_3 * d_1 * (z^2 - x^2)$$

$$U_{pz} = t_6 * d_1 * y * z$$

$$V_x = t_{24} * f_6 * y * z * x$$

$$V_y = (c_{12} + c_{44}) * z + t_4 * f_5 * (z^3 + t_3 * y^2 * z) + t_{12} * f_6 * z * x^2$$

$$V_z = (c_{12} + c_{44}) * y + t_4 * f_5 * (t_3 * y * z^2 + y^3) + t_{12} * f_6 * y * x^2$$

$$V_{px} = t_3 * d_1 * (y^2 - z^2)$$

$$V_{py} = t_6 * d_1 * x * y$$

$$V_{pz} = -t_6 * d_1 * x * z$$

$$C_x = Q_x + R_x + S_x$$

$$C_y = Q_y + R_y + S_y$$

$$C_z = Q_z + R_z + S_z$$

C The partial derivatives of the coefficients of the cubic equation are now calculated. Again dx stands for the derivative of d with respect to the component of the wave vector in the x direction.

$$dx = t_2 * T * T_x + t_2 * T_p * T_{px} + t_2 * U * U_x + t_2 * U_p * U_{px} + t_2 * V * V_x + t_2 * V_p * V_{px}$$

$$1 - Q * R_x - Q_x * R - R * S_x - R_x * S - S * Q_x - S_x * Q$$

$$dy = t_2 * T * T_y + t_2 * T_p * T_{py} + t_2 * U * U_y + t_2 * U_p * U_{py} + t_2 * V * V_y + t_2 * V_p * V_{py}$$

$$1 - Q * R_y - Q_y * R - R * S_y - R_y * S - S * Q_y - S_y * Q$$

$$dz = t^2 * T * T_z + t^2 * T_p * T_{pz} + t^2 * U * U_z + t^2 * U_p * U_{pz} + t^2 * V * V_z + t^2 * V_p * V_{pz}$$

$$1 \quad -Q * R_z - Q_z * R - R * S_z - R_z * S - S * Q_z - S_z * Q$$

$$ex = Q * R * S_x + Q * R_x * S + Q_x * R * S - t^2 * T * T_x * S - T * T * S_x - t^2 * T_p * T_{px} * S$$

$$1 \quad -T_p * T_p * S_x - t^2 * U * U_x * R - U * U * R_x - t^2 * U_p * U_{px} * R - U_p * U_p * R_x$$

$$2 \quad -t^2 * V * V_x * Q - V * V * Q_x - t^2 * V_p * V_{px} * Q - V_p * V_p * Q_x + t^2 * T * U * V_x$$

$$3 \quad + t^2 * T * U_x * V + t^2 * T_x * U * V - t^2 * T * U_p * V_{px} - t^2 * T * U_{px} * V_p - t^2 * T_x * U_p * V_p$$

$$4 \quad - t^2 * T_p * U * V_{px} - t^2 * T_p * U_x * V_p - t^2 * T_{px} * U * V_p - t^2 * T_p * U_p * V_x - t^2 * T_p * U_{px} * V$$

$$5 \quad - t^2 * T_{px} * U_p * V$$

$$ey = Q * R * S_y + Q * R_y * S + Q_y * R * S - t^2 * T * T_y * S - T * T * S_y - t^2 * T_p * T_{py} * S$$

$$1 \quad -T_p * T_p * S_y - t^2 * U * U_y * R - U * U * R_y - t^2 * U_p * U_{py} * R - U_p * U_p * R_y$$

$$2 \quad -t^2 * V * V_y * Q - V * V * Q_y - t^2 * V_p * V_{py} * Q - V_p * V_p * Q_y + t^2 * T * U * V_y$$

$$3 \quad + t^2 * T * U_y * V + t^2 * T_y * U * V - t^2 * T * U_p * V_{py} - t^2 * T * U_{py} * V_p - t^2 * T_y * U_p * V_p$$

$$4 \quad - t^2 * T_p * U * V_{py} - t^2 * T_p * U_y * V_p - t^2 * T_{py} * U * V_p - t^2 * T_p * U_p * V_y - t^2 * T_p * U_{py} * V$$

$$5 \quad - t^2 * T_{py} * U_p * V$$

$$ez = Q * R * S_z + Q * R_z * S + Q_z * R * S - t^2 * T * T_z * S - T * T * S_z - t^2 * T_p * T_{pz} * S$$

$$1 \quad -T_p * T_p * S_z - t^2 * U * U_z * R - U * U * R_z - t^2 * U_p * U_{pz} * R - U_p * U_p * R_z$$

$$2 \quad -t^2 * V * V_z * Q - V * V * Q_z - t^2 * V_p * V_{pz} * Q - V_p * V_p * Q_z + t^2 * T * U * V_z$$

$$3 \quad + t^2 * T * U_z * V + t^2 * T_z * U * V - t^2 * T * U_p * V_{pz} - t^2 * T * U_{pz} * V_p - t^2 * T_z * U_p * V_p$$

$$4 \quad - t^2 * T_p * U * V_{pz} - t^2 * T_p * U_z * V_p - t^2 * T_{pz} * U * V_p - t^2 * T_p * U_p * V_z - t^2 * T_p * U_{pz} * V$$

$$5 \quad - t^2 * T_{pz} * U_p * V$$

C The angular frequencies and group velocity vectors are now calculated.

$$fr = p*w(j)*w(j)$$

$$wk = t2*p*w(j) * (t3*fr*fr-(t2*c*fr)-d)$$

$$Velx0(j) = (ex+fr*dx+fr*fr*Cx)/ wk$$

$$Vely0(j) = (ey+fr*dy+fr*fr*Cy)/ wk$$

$$Velz0(j) = (ez+fr*dz+fr*fr*Cz)/ wk$$

38 CONTINUE

RETURN

END